8/22/95

SANDIA REPORT

SAND94–1941 • UC–814
Unlimited Release
Printed August 1995

Yucca Mountain Site Characterization Project

Effect of Roughness and Material Strength on the Mechanical Properties of Fracture Replicas

J. Wibowo, B. Amadei, R. H. Price, S. R. Brown, S. Sture

Prepared by
Sandia National Laboratories
Albuquerque, New Mexico 87185 and Livermore, California 94550
for the United States Department of Energy
under Contract DE-AC04-94AL85000

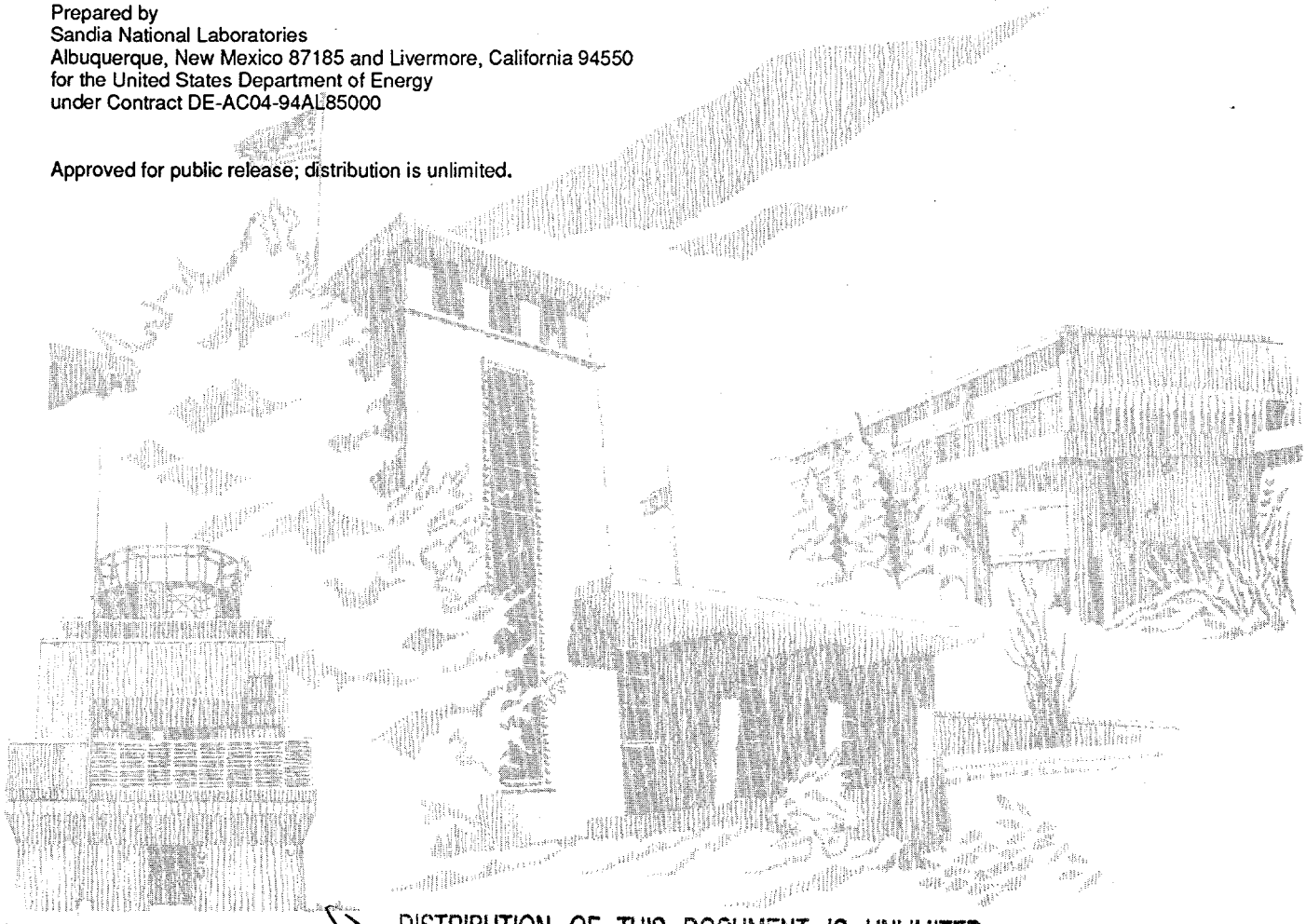

"Prepared by Yucca Mountain Site Characterization Project (YMSCP) participants as part of the Civilian Radioactive Waste Management Program (CRWM). The YMSCP is managed by the Yucca Mountain Project Office of the U.S. Department of Energy, DOE Field Office, Nevada (DOE/NV). YMSCP work is sponsored by the Office of Geologic Repositories (OGR) of the DOE Office of Civilian Radioactive Waste Management (OCRWM)."

Issued by Sandia National Laboratories, operated for the United States Department of Energy by Sandia Corporation.

Available to DOE and DOE contractors from
Office of Scientific and Technical Information
PO Box 62
Oak Ridge, TN 37831

Prices available from (615) 576-8401, FTS 626-8401

Available to the public from
National Technical Information Service
US Department of Commerce
5285 Port Royal Rd
Springfield, VA 22161

NTIS price codes
Printed copy: A06
Microfiche copy: A01

DISCLAIMER

Portions of this document may be illegible in electronic image products. Images are produced from the best available original document.

Distribution
Category UC-814

SAND 94-1941
Unlimited Release
Printed August 1995

Effect of Roughness and Material Strength on the Mechanical Properties of Fracture Replicas

J. Wibowo[†], B. Amadei[†], R. H. Price[*], S. R. Brown[*], S. Sture[†]

[†]Department of Civil, Environmental, and Architectural Engineering
University of Colorado at Boulder
Boulder, Colorado 80309-0428

[*]Sandia National Laboratories
Albuquerque, New Mexico 87185-1325

ABSTRACT

This report presents the results of 11 rotary shear tests conducted on replicas of three hollow cylinders of natural fractures with JRC values of 7.7, 9.4 and 12.0. The JRC values were determined from the results of laser profilometer measurements. The replicas were created from gypsum cement. By varying the water-to-gypsum cement ratio from 30 to 45%, fracture replicas with different values of compressive strength (JCS) were created. The rotary shear experiments were performed under constant normal (nominal) stresses ranging between 0.2 and 1.6 MPa. In this report, the shear test results are compared with predictions using Barton's empirical peak shear strength equation. Observations during the experiments indicate that only certain parts of the fracture profiles influence fracture shear strength and dilatancy. Under relatively low applied normal stresses, the JCS does not seem to have a significant effect on shear behavior. As an alternative, a new procedure for predicting the shear behavior of fractures was developed. The approach is based on basic fracture properties such as fracture surface profile data and the compressive strength, modulus of elasticity, and Poisson's ratio of the fracture walls. Comparison between predictions and actual shear test results shows that the alternative procedure is a reliable method.

This report was prepared under the Yucca Mountain Project WBS number 1.2.4.2.1.2. The data in this report was developed subject to the planning in work agreements WA-0129, Rev.0 and QA controls in QAGR for S124212 (QAGR-008, Rev.0); the data is not qualified and not to be used for licensing.

CONTENTS

LIST OF FIGURES

LIST OF TABLES

1. INTRODUCTION

In 1976 Barton proposed a failure criterion to estimate the peak shear strength of rock joints in terms of the applied normal stress, the strength of the joint surface material, and the joint surface roughness. The criterion is expressed as follows

$$\tau_p = \sigma_n \tan\left[\phi + JRC \log_{10}\left(\frac{JCS}{\sigma_n}\right)\right], \qquad (1)$$

where τ_p is the peak shear strength, σ_n is the applied normal stress, ϕ is the basic friction angle, JRC is the joint roughness coefficient, and JCS is the joint wall compressive strength.

The above formulation was studied extensively by Barton and Choubey (1977). Ten different scales of surface roughness were introduced with JRC ranging between 0 and 20. The International Society for Rock Mechanics (ISRM, 1981) suggested that these ten scales of roughness be used as a standard to determine the JRC of natural fracture surfaces.

Two remarks can be made regarding JRC. First, the ten roughness scales were established based on the results of more than 100 direct shear experiments conducted on rock joints. In their paper, Barton and Choubey concluded that the actual value of JRC for a given joint could range between 0.5 and 2 times the values estimated using the scales of roughness. Second, different techniques recommended by Barton and co-workers to determine JRC have been found to give different values of JRC for a same joint. This was illustrated in an earlier report by Wibowo et al. (1994) in the analysis of direct shear tests conducted on replicas of fractures of welded tuff.

Because of its simplicity and despite its limitations, Barton's joint shear strength model has gained considerable acceptance in the rock mechanics and practicing engineering communities. The

design and construction of the proposed repository at Yucca Mountain depend, in part, on the accurate description and subsequent modeling of the shear strength of rock joints. Barton's empirical model for rock joint strength has been considered for use in this process. Due to the widespread acceptance of Barton's model and potential applications to the Yucca Mountain Project, Sandia National Laboratories (SNL) proposed that the relationship among JRC, JCS, and the geometrical and physical characteristics, which the terms imply, be given careful scrutiny.

This report presents the results of 11 rotary shear tests conducted on replicas of three hollow cylinders containing natural fractures with JRC values of 7.7, 9.4 and 12.0. The JRC values were determined from the results of laser profilometer measurements. The replicas were made from gypsum. By varying the water-to-gypsum cement ratio from 30 to 45%, fracture replicas with different values of JCS could be created. The rotary shear experiments were performed under constant normal (nominal) stresses ranging between 0.2 and 1.6 MPa. In this report, the shear test results are compared with predictions using Barton's empirical peak shear strength equation [equation (1)]. Observations during the experiments indicate that only certain parts of the fracture profiles influence fracture shear strength and dilatancy. Under relatively low applied normal stresses, the compressive strength (JCS) does not seem to have a significant effect.

As an alternative, a new procedure for predicting the shear behavior of the fractures was developed. The analysis of two rough surfaces in contact was replaced by the analysis of the composite topography of the two surfaces against a flat and stiff surface (Brown and Scholz, 1986). The asperities were assumed to have the form of wedges that fail in a brittle manner (Byerlee, 1967). The elastic displacement of the two surfaces was assessed by using Hertzian contact theory. Two possible types of failures were considered, i.e., sliding friction and shear, which are both accounted for in Patton's bilinear shear strength failure envelope (Patton, 1966). As shear displacement progresses, the type of

failure can be determined, and the values of shear stress and dilatancy can be predicted. The input data for this prediction procedure include all basic material properties, i.e., fracture surface roughness profile data, and the compressive strength, modulus of elasticity, and Poisson's ratio of the fracture walls. Comparisons between the predictions and the actual rotary shear test results indicate that the proposed alternative approach is a reliable method for predicting the shear behavior of the tested hollow cylinder fractures.

2. EXPERIMENTAL WORK

2.1 Experimental Matrix

Rotary shear tests were conducted on replicas of hollow cylinders of natural fractures as shown schematically in Figure 1. The hollow cylinders had inner and outer diameters of 51 mm and 76 mm, respectively. Five natural fractures were selected with surfaces having JRC values ranging between 0 and 20. The JRCs were determined using a laser profilometer. The fracture replicas were created from gypsum cement (Ultracal 30, produced by United States Gypsum, Chicago, Illinois). Due to time limitation, however, only replicas of three fractures were fabricated with JRC values of 9.4, 7.7, and 12.0. Throughout this report, these fractures are referred to as fractures #1, 2, and 4, respectively. For each fracture, several replicas were made with water-to-gypsum cement ratios (by weight) of 30, 35, 38, or 45% in order to model fractures with different wall strengths and hardnesses.

Each gypsum fracture replica was identified using a four digit number: the first digit refers to the fracture number, the second and third digits refer to the water-to-gypsum cement ratio, and the fourth digit refers to the replica number. As an example, a sample with identification #1302 indicates that the sample represents fracture #1, with a 30% water-to-gypsum cement ratio, and is the second replica. A total of 11 rotary shear tests was conducted.

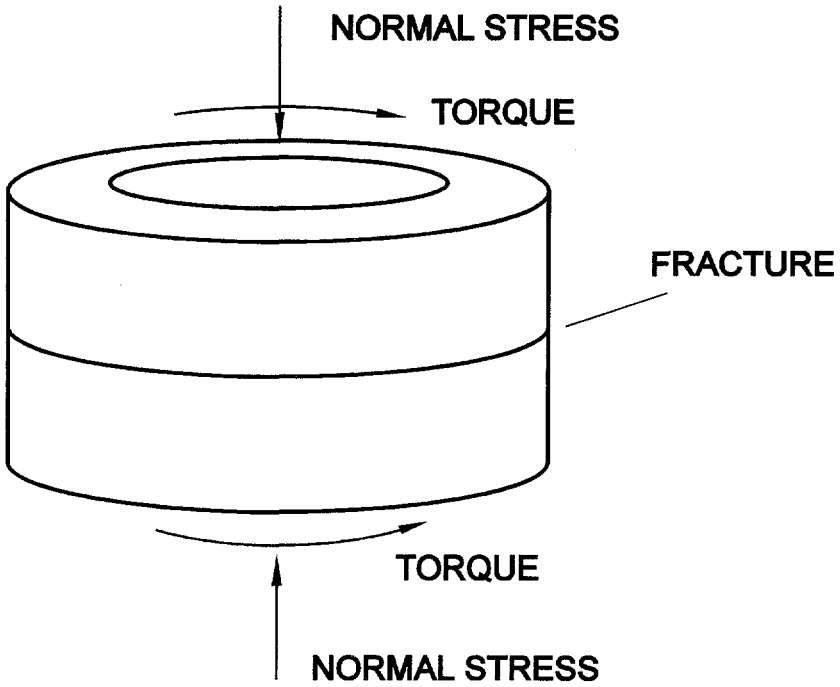

Figure 1. Rotary direct shear on hollow cylinder fracture replica.

For the fracture replicas with a JRC of 9.4 and a water-to-gypsum cement ratio of 30%, rotary shear tests were conducted under constant normal stresses of 0.2, 0.4, 0.8, and 1.6 MPa (samples #1301, 1302, 1303, and 1304). For the fracture replicas with JRC values of 7.7 and 12.0, and a water-to-gypsum cement ratio of 30%, rotary shear tests were performed under a constant normal stress of 0.4 MPa (samples #2301 and 4301). For fracture replicas with a JRC value of 9.4 and water-to-gypsum cement ratios of 35, 38, and 45%, rotary shear tests were conducted under a constant normal stress of 0.4 MPa (samples #1351, 1381, and 1451). In order to check the consistency of the experimental procedure, two additional fracture replicas with a JRC of 9.4 and a water-to-gypsum cement ratio of 30% were sheared under constant normal stresses of 0.4 and 0.8 MPa (samples #1305 and 1306). The overall experimental matrix is shown in Table 1.

Table 1.
Experimental matrix.

Sample #	Fracture #	JRC	Water vs. Gypsum Ratio (%)	Normal Stress (MPa)
1301	1	9.4	30	0.4
1302	1	9.4	30	0.8
1303	1	9.4	30	0.2
1304	1	9.4	30	1.6
1305	1	9.4	30	0.4
1306	1	9.4	30	0.8
1351	1	9.4	35	0.4
1381	1	9.4	38	0.4
1451	1	9.4	45	0.4
2301	2	7.7	30	0.4
4301	4	12.0	30	0.4

Prior to each rotary shear test, one cycle of normal loading and unloading was performed. Also, the fracture surface hardness and strength were assessed by indentation and Schmidt Rebound Hammer tests.

2.2 Experimental Procedure

2.2.1 Laser Profilometer Scanning

The topography of the top and bottom surfaces of each natural fracture was mapped using a non-contact laser profilometer available in the SNL Geomechanics Division. This equipment consists of a precision three-axis positioning system that moves a laser distance measurement probe over a surface, then records the variation in the surface height. The sensor used in this instrument is a non-contact laser head manufactured by Cyber-Optics, Inc. in Minneapolis. A laser beam from a low-power He-Ne laser source is directed normally onto the plane of the fracture surface. The interception of the normally incident laser beam at the measured fracture surface is focused onto a photo diode array via a 35 mm

SLR camera. The optical axis of the lens is inclined by a small angle to the laser beam from the He-Ne laser source. The elevation of the measured point is given by simple geometric relations through the position of the image on the photo diode array. A more detailed discussion of this laser profile scanner can be found in Huang et al. (1988). Each measurement consisted of three annular (circular) profiles with radii of 29.25, 31.75, and 34.25 mm and each profile consisted of 7,860 points with an interval of about 0.0254 mm.

2.2.2 Unconfined Compression Tests

Unconfined compression tests were performed on gypsum cement cylinders according to ASTM D 2938-86 specifications, with a variety of water-to-gypsum cement ratios of 25, 30, 35, 38, and 45%, using a 980 kN MTS frame system available in the SNL Geomechanics Division. The gypsum cylinders were 5.1 cm in diameter and 10.2 cm in length. The bottom and top surfaces of the gypsum cylinders were polished and parallel. Vertical displacements were measured using Linear Variable Differential Transformers (LVDTs) which are attached to the samples. The normal load was measured using a load transducer.

2.2.3 Joint Wall Compressive Strength

Before conducting the rotary shear tests, the hardness of the surfaces of each fracture replica was determined using indentation and Schmidt Rebound Hammer tests.

Indentation Tests

Two indentation tests were performed by penetrating a sharp carbide cone (indenter) into the smooth surface of each gypsum fracture replica. The angle of the cone tip was 34.6°. The tests were carried out using a 98 kN MTS frame. The rate of penetration of the indenter was determined by the rate of loading of 0.1 kN/min. The amount of penetration was measured using two LVDTs.

Schmidt Rebound Hammer Tests

Three Schmidt Rebound Hammer tests were performed on the smooth surface of each gypsum fracture replica. The rebound numbers, ranging between 10 and 60, were recorded for each test. The final value of the rebound number was the average of the three readings.

2.2.4 Normal Compression Tests

Before conducting the rotary shear tests, each fracture replica was subject to one cycle of normal loading and unloading to a maximum load of 4.5 kN. The rate of loading (and unloading) was set at 1 kN/min. The tests were carried out using a 900 kN MTS system. The vertical displacements were measured using two LVDTs attached to the sample replica holders.

2.2.5 Rotary Shear Tests

The rotary shear apparatus consists of a load frame containing a hydraulic rotary actuator in series with a hydraulic linear actuator. The maximum torque capability is 7.0 kN-m, and the maximum axial force is 900 kN. These actuators are independently servo-controlled by 410 function generators and 442 controllers from MTS Systems, Inc. After being subjected to one cycle of normal loading and unloading, each fracture replica was compressed to its preassigned normal stress for the rotary shear tests. The amplitude of the rotation was 30° and the rotation rate was 0.5 °/min (one cycle per hour). The top part of each fracture replica was fixed, while the bottom part rotated. In each shear cycle, the bottom part of the fracture replica was first rotated 30° in the counterclockwise direction. Then, rotation was reversed 60° in the clockwise direction. Finally, rotation in the counterclockwise direction was applied to bring back the fracture replica to its original position. The vertical displacements were measured with two LVDTs. A more detailed discussion of the rotary shear procedure can be found in Olsson (1987). The results were recorded using a

personal computer with a data acquisition system developed by Holcomb and Jones (1983).

3. EXPERIMENTAL RESULTS

3.1 Profilometer Measurement Results

3.1.1 Profile Data

Three annular (circular) roughness profiles were recorded on the top and bottom surfaces of each natural fracture. Figure 2 shows an example for the bottom part of fracture #1. In this figure, the annular axis is related to the angle of rotation (in degrees), and the radial axis is related to the asperity height (in mm). In order to present the three profiles in one figure more clearly, the inner, middle and outer profiles are depicted with offsets of 15.0, 17.5 and 20.0 mm, respectively. Figure 2 indicates that the three profiles are essentially similar. Other fracture profiles can be found in Appendix A.

3.1.2 JRC Calculations

Because the JRC values could not be determined by tilt tests, they were determined, instead, using the methods proposed by Tse and Cruden (1979) and modified by Yu and Vayssade (1991). These authors digitized Barton and Choubey's standard profiles into several hundred points and proposed an empirical regression equation between the JRC and the Root Mean Square (RMS) of the first derivative of the profile, Z_2. Yu and Vayssade (1991) recommended the following relation,

$$JRC = 60.32 * Z_2 - 4.51, \qquad (2)$$

for profiles with sampling intervals of 0.25 mm. In order to use equation (2), all measured profiles were resampled to obtain

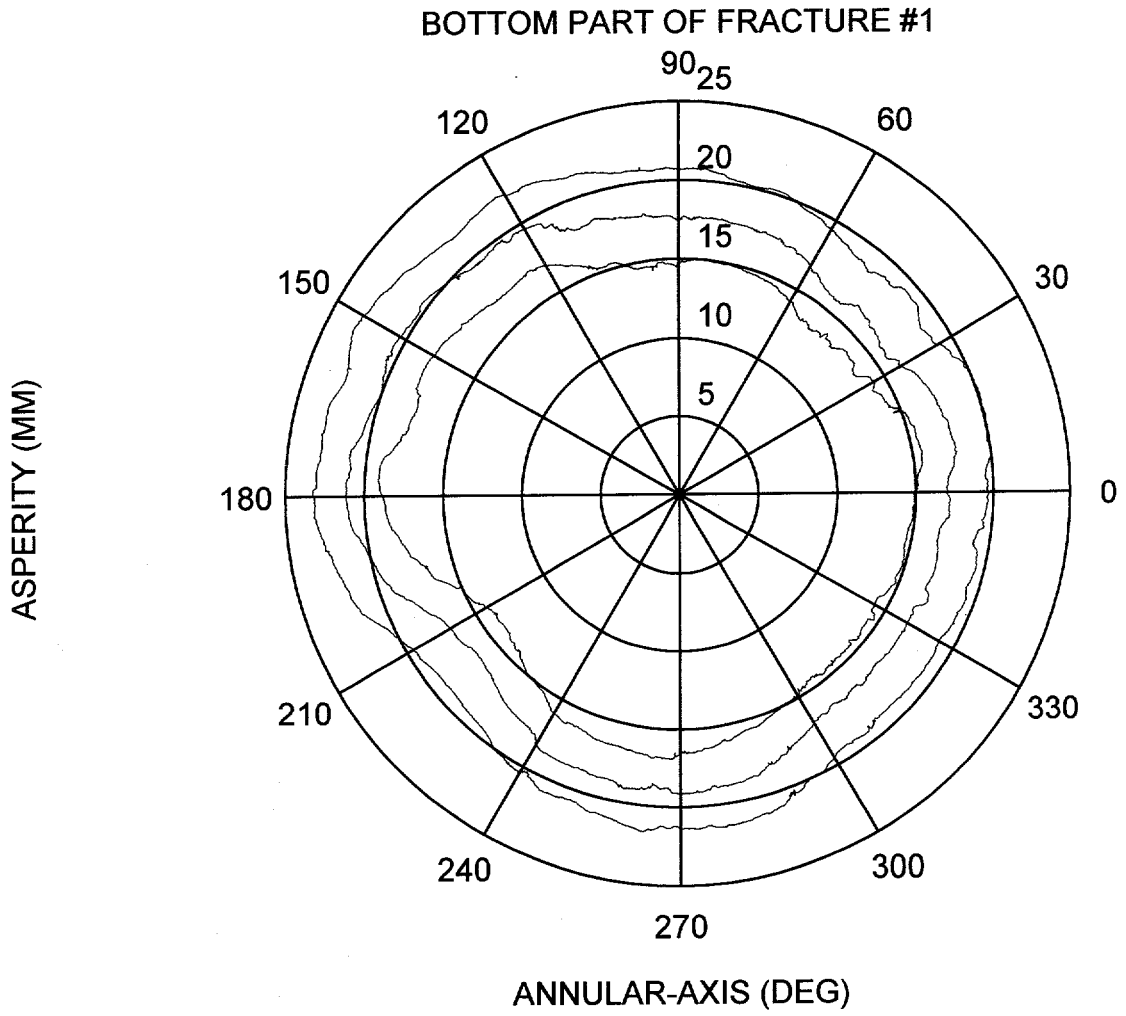

Figure 2. Annular topography of bottom part of fracture #1.

similar profiles with 0.25 mm sampling intervals. The value of Z_2 is defined as follows,

$$Z_2 = \sqrt{\frac{1}{M(D_x)^2}\sum (y_{i+1} - y_i)^2}, \qquad (3)$$

where M is the number of sampling intervals, D_x is the interval size, and y_i is the asperity height along the profile. The value of JRC is then corrected for scale effect as suggested by Barton and Bandis (1990), using the following empirical equation,

$$JRC_n = JRC_0 \left[\frac{L_n}{L_0}\right]^{-0.02JRC_0}, \qquad (4)$$

where JRC_0 is the JRC value before correction corresponding to a joint sample length L_0 of 100 mm and JRC_n is the value of JRC after correction for the actual length L_n of the joint profiles. Table 2 gives a summary of the values of JRC for fractures 1 through 5. In this table, JRC_t is the average of the three JRC values calculated for the top part of each fracture, and JRC_b is the average of the three JRC values calculated for the bottom part of each fracture. Also, JRC_{ave} is equal to 0.5 (JRC_t + JRC_b).

3.2 Unconfined Compression Test Results

The uniaxial compressive strength of five different mixtures of water and gypsum cement was determined. For each test, Young's modulus and Poisson's ratio were calculated from the average slope of the stress-strain curves between 10 and 50% of the peak stress. The results of the unconfined compression tests are reported in Table 3.

Table 2

Joint roughness coefficient calculation.

Fracture #	JRC_t (top)	JRC_b (bottom)	JRC_{ave}
1	9.7	9.1	9.4
2	8.2	7.2	7.7
3	13.0	13.0	13.0
4	11.6	12.3	12.0
5	7.3	7.1	7.2

Table 3.

Unconfined compression test results.

Water/Gypsum Ratio (%)	Maximum Stress (MPa)	Young's Modulus 10^3(MPa)	Poisson's Ratio
25	47.2	16.6	0.27
30	63.4	16.3	0.27
35	49.2	16.0	0.25
38	29.7	15.3	0.24
45	23.2	12.4	0.24

3.3 Joint Wall Compressive Strength (JCS) Test Results

3.3.1 Schmidt Rebound Hammer Test Results

A correlation between the Schmidt Rebound Hammer number and the unconfined compressive strength of the surface of the material was given by Miller (1965, after Barton and Choubey, 1977),

$$\log_{10}(\sigma_c) = 0.00088\gamma R + 1.01, \quad (5)$$

where σ_c is the unconfined compressive strength (MPa), γ is the dry density of rock (kN/m^3), and R is the rebound number. In Table 4, the values of JCS = σ_c determined using equation (5) are compared with the values of the unconfined compressive strength reported in Table 3.

Table 4 shows that JCS for the samples with water-to-gypsum cement ratio of 30% is about 42% of the unconfined compressive strength. For the samples with water-to-gypsum cement ratios of 35, 38, and 45%, the values of JCS are respectively 51, 75, and 80% of the unconfined compressive strength. It can be concluded that the empirical equation (5) developed for rocks is not suitable to predict the unconfined compressive strength of gypsum-cement.

Table 4
Joint wall compressive strength using Schmidt Rebound Hammer.

Sample #	Dry Density, γ (kN/m^3)	Rebound Number, R (average)	Joint Wall Compressive Strength, JCS (MPa)	Uniaxial Compressive Strength (MPa)
1301	18.0	25	25.5	63.4
1302	18.0	24	24.6	63.4
1303	18.0	26	26.4	63.4
1304	18.0	26	26.4	63.4
1305	18.0	24	24.6	63.4
1306	18.0	27	27.4	63.4
1351	17.1	26	25.2	49.2
1381	16.7	23	22.3	29.7
1451	15.4	19	18.5	23.2
2301	18.0	29	29.5	63.4
4301	18.0	28	28.4	63.4

3.3.2 Indentation Test Results

The indentation tests were performed in order to evaluate the hardness of the fracture replica surfaces. Hankins (1925, after

Tabor, 1951) considered that there is an intrinsic yield pressure (or hardness), H, which is independent of the shape of the indentor. Figure 3 shows a cone of hard material indenting a softer surface. According to Hankins, the value of the hardness, H, can be expressed as follows,

$$H = \frac{4W}{\pi d^2}\left(\frac{1}{1 + \mu\tan\alpha}\right), \qquad (6)$$

where W is the applied normal load in kilograms (about 45.4 kg), d is the diameter of the impression in mm ($d = 2p\tan\alpha$), p is the depth of penetration in mm, μ is the coefficient of friction between the two materials (assumed here to be tan 30°), and 2α is the angle of the cone tip.

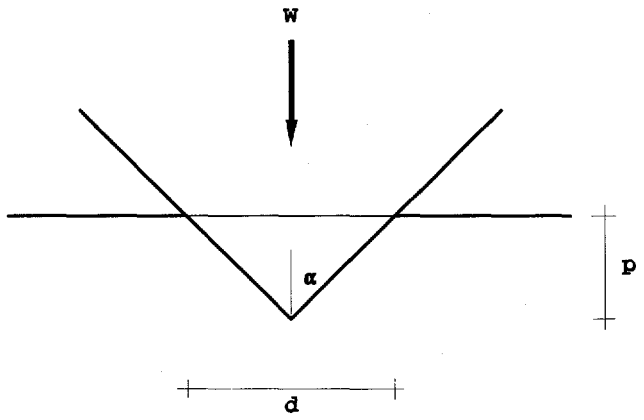

Figure 3. Schematic diagram of a conical indenter.

Table 5 gives the value of H for all the fracture replicas. The value of surface hardness decreases as the water-to-gypsum cement ratio increases. For water-to-gypsum cement ratios ranging between 30 and 45%, the hardness varies between 922.8 and 389.3 MPa.

Table 5
Indentation test results.

Sample #	Water/Gypsum Ratio (%)	Average Indentation p (mm)	Hardness, H (MPa)	Unconfined Compressive Strength (MPa)
1301	30	1.24	829.6	63.4
1302	30	1.44	603.1	63.4
1303	30	1.31	736.5	63.4
1304	30	1.46	592.3	63.4
1305	30	1.44	620.8	63.4
1306	30	1.32	724.7	63.4
1351	35	1.43	617.8	49.2
1381	38	1.51	554.1	29.7
1451	45	1.80	389.3	23.2
2301	30	1.41	635.5	63.4
4301	30	1.17	922.8	63.4

3.4 Normal Compression Test Results

As an example, Figure 4 shows the response of sample #1302 to one cycle of loading and unloading. Other normal load versus normal displacement response curves can be found in Appendix B. Table 6 gives the values of the maximum normal displacement when the normal load is equal to 4.5 kN for all the tested fracture replicas. As expected, the weaker the material, the larger the maximum displacement. The variations in Table 6 indicate the possibility that during preparation, the bottom and top surfaces of some of the fracture specimens may not have been exactly mated.

3.5 Rotary Shear Test Results

The relationship between the tangential shear stress and the applied torque in each fracture plane is considered after full establishment of slip, that is, when the torque is nominally independent of the rotation (Olsson, 1987). The torque-shear stress

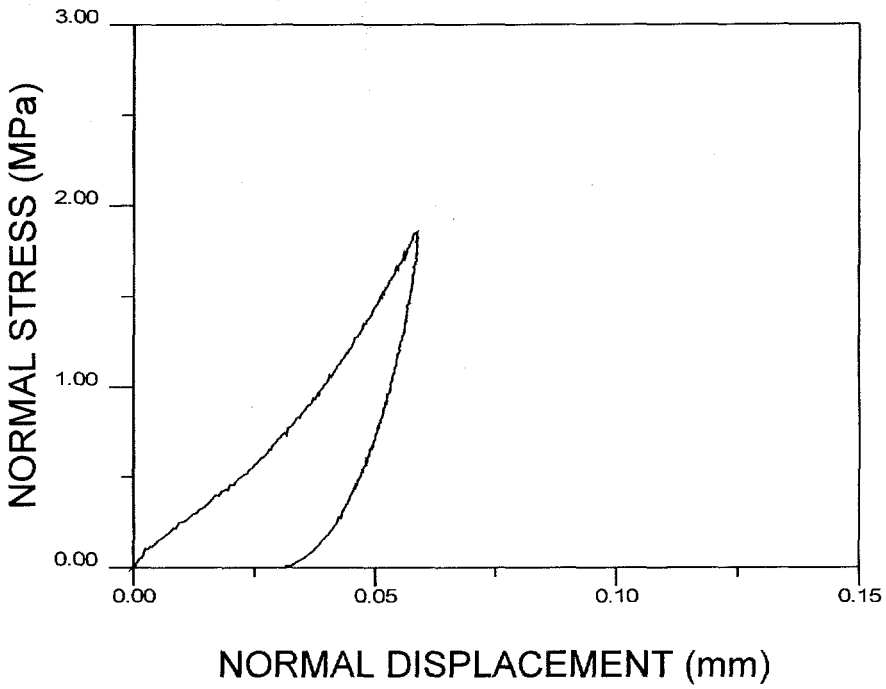

Figure 4. Normal compression test result for sample #1302.

Table 6.

Maximum displacements during normal compression tests.

Sample #	Maximum Displacement at 4.5 kN Normal Load (mm)
1301	0.06
1302	0.06
1303	0.08
1304	0.08
1305	0.11
1306	0.08
1351	0.05
1381	0.10
1451	0.09
2301	0.07
4301	0.13

relation has the same form as that of a fully-yielded plastic tube. The tangential shear stress, τ_f, is calculated from

$$\tau_f = \frac{3T_{fs}}{2\pi(R_o^3 - R_i^3)}, \qquad (7)$$

where T_{fs} is the applied torque during full sliding and R_o and R_i are the outer and inner radii of the gypsum hollow cylinder, respectively.

Typical shear stress versus slip (mean shear displacement) and dilatancy versus slip (mean shear displacement) response curves for sample #1301 are shown in Figures 5a and 5b, respectively. This sample has a water-to-gypsum cement ratio equal to 30% and was tested under a constant normal load of 1 kN (or normal stress = 0.4 MPa). Figure 5a indicates that for forward (counterclockwise) shear motion, a peak shear stress of 0.61 MPa occurs after a slip of 0.79 mm (or a rotation of 1.4°). On the other hand, for reverse (clockwise) shear motion, a peak shear stress of 0.48 MPa occurs after a slip of -1.57 mm (or a rotation of 2.8°). The other rotary shear test results can be found in Appendix C. A summary of the peak shear strengths and peak slips for all fracture replicas can be found in Table 7.

Comparison of the results of the rotary shear tests on samples #1301 and #1305 (tests on two similar samples under similar conditions) indicates that the values of peak shear strength are similar, but that the peak slips are slightly different. This could be due to a small offset between the top and bottom surfaces of the joint specimens which may have taken place during specimen preparation. Comparison of the test results for samples #1302 and 1306 indicates that both peak shear strength and peak slip values are quite similar.

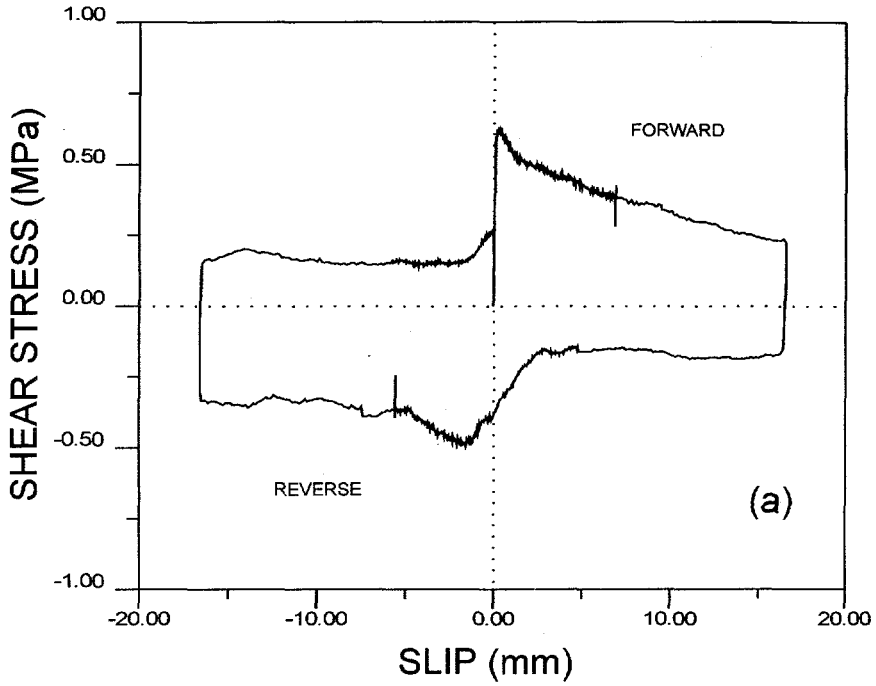

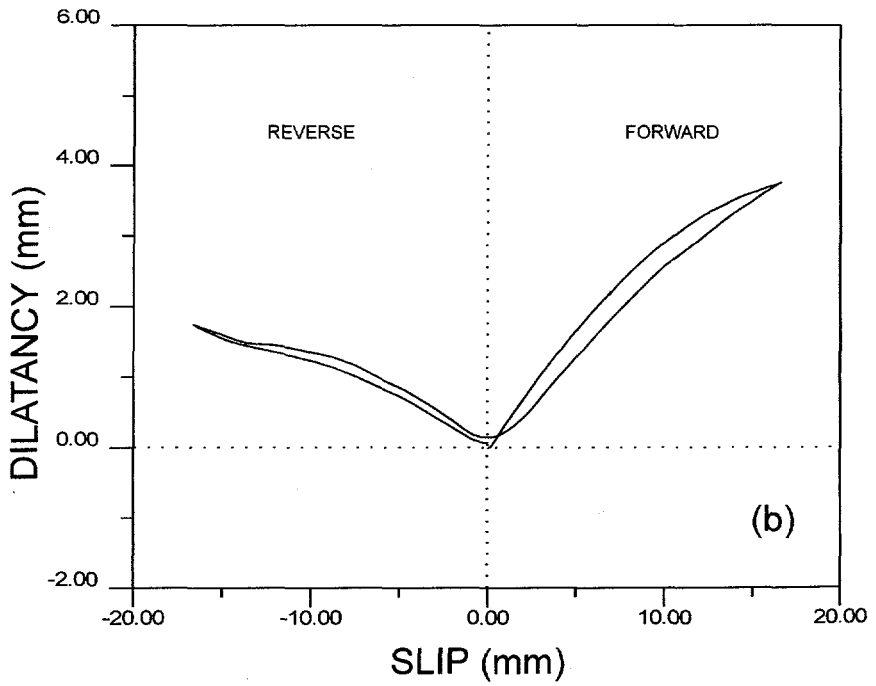

Figure 5. (a) Shear stress vs. slip, and (b) Dilatancy vs. slip response curves for sample #1301 tested under a constant normal stress of 0.4 MPa.

Table 7

Values of peak shear strength and peak slip.

Sample #	σ_n (MPa)	Forward Motion		Reverse Motion	
		τ_p (MPa)	u_p (mm)	τ_p (MPa)	u_p (mm)
1301	0.4	0.61	0.79	0.48	1.57
1302	0.8	1.14	0.38	0.90	1.47
1303	0.2	0.38	0.74	0.29	0.51
1304	1.6	2.28	1.85	1.59	0.70
1305	0.4	0.59	0.38	0.47	0.54
1306	0.8	1.10	0.46	0.94	1.79
1351	0.4	0.62	0.57	0.50	0.52
1381	0.4	0.59	0.87	0.54	1.42
1451	0.4	0.61	1.44	0.50	2.10
2301	0.4	0.42	0.73	0.36	0.67
4301	0.4	0.68	0.55	0.58	0.52

Figures 6a and 6b show, respectively, the shear stress versus slip and dilatancy versus slip response curves for forward motion for four replicas of fracture #1 (samples #1301, 1302, 1303 and 1304) tested under constant normal (nominal) stress ranging between 0.2 and 1.6 MPa. All four samples have the same 30% water-to-gypsum cement ratio. As expected, the shear strength increases and the dilatancy decreases as the normal stress increases.

Figures 7a and 7b show, respectively, the shear stress versus slip and dilatancy versus slip response curves for forward motion for four replicas of fracture #1 with different water-to-gypsum cement ratios of 30% (sample #1301), 35% (sample #1351), 38% (sample #1381) and 45% (sample #1451). All samples were tested under a constant normal (nominal) stress of 0.4 MPa. It appears that although the four samples have strengths that are different and vary between 23.2 and 63.4 MPa, their shear behavior is essentially the same. A slight decrease in dilatancy with an increase in the water-to-gypsum cement ratio can be observed in Figure 7b.

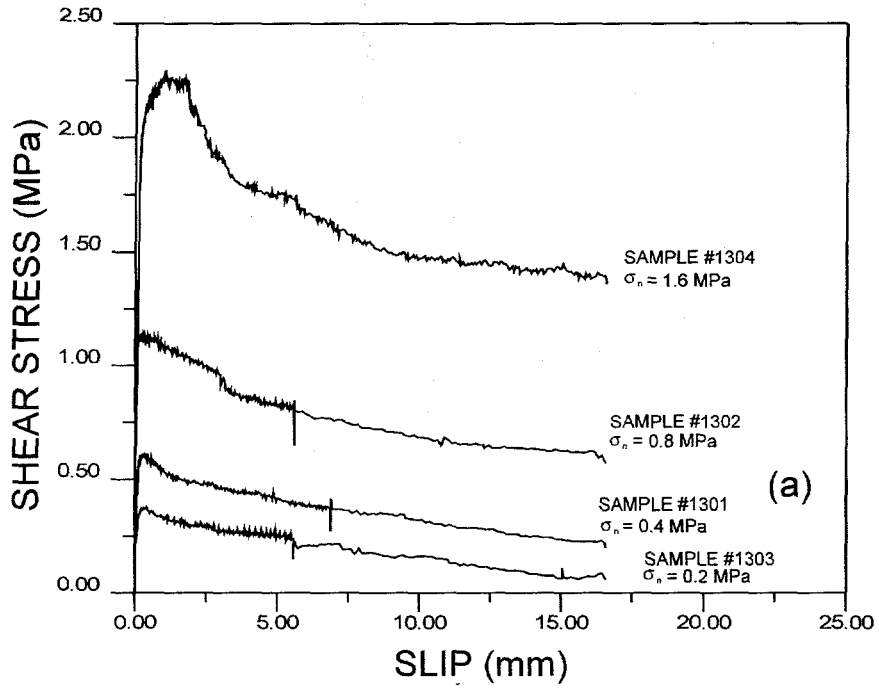

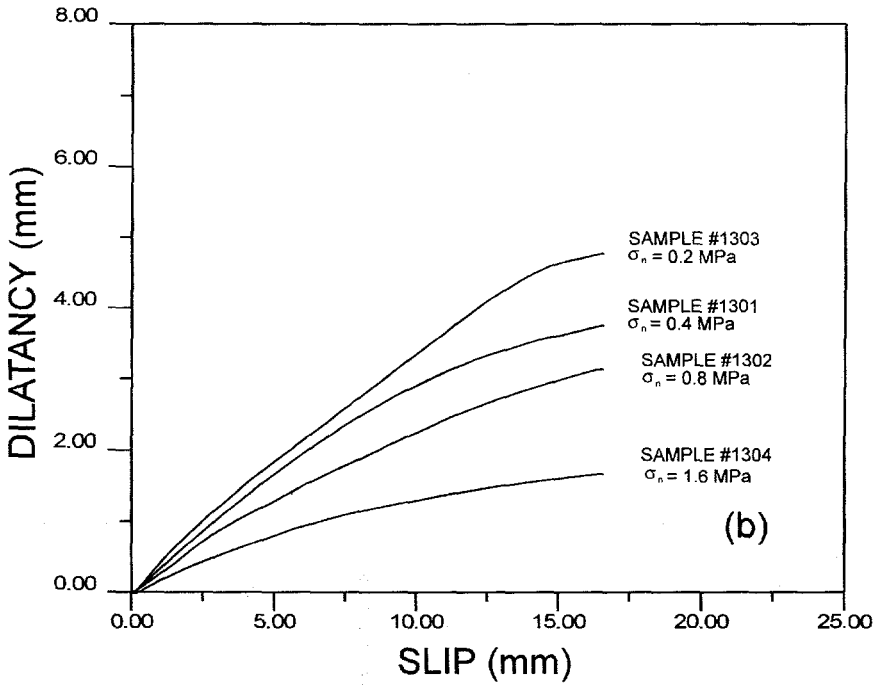

Figure 6. (a) Shear stress vs. slip, and (b) Dilatancy vs. slip response curves for four replicas of fracture #1 with same 30% water-to-gypsum cement ratio and tested under different levels of applied normal stress. Forward shear motion. Samples #1301, 1302, 1303, and 1304.

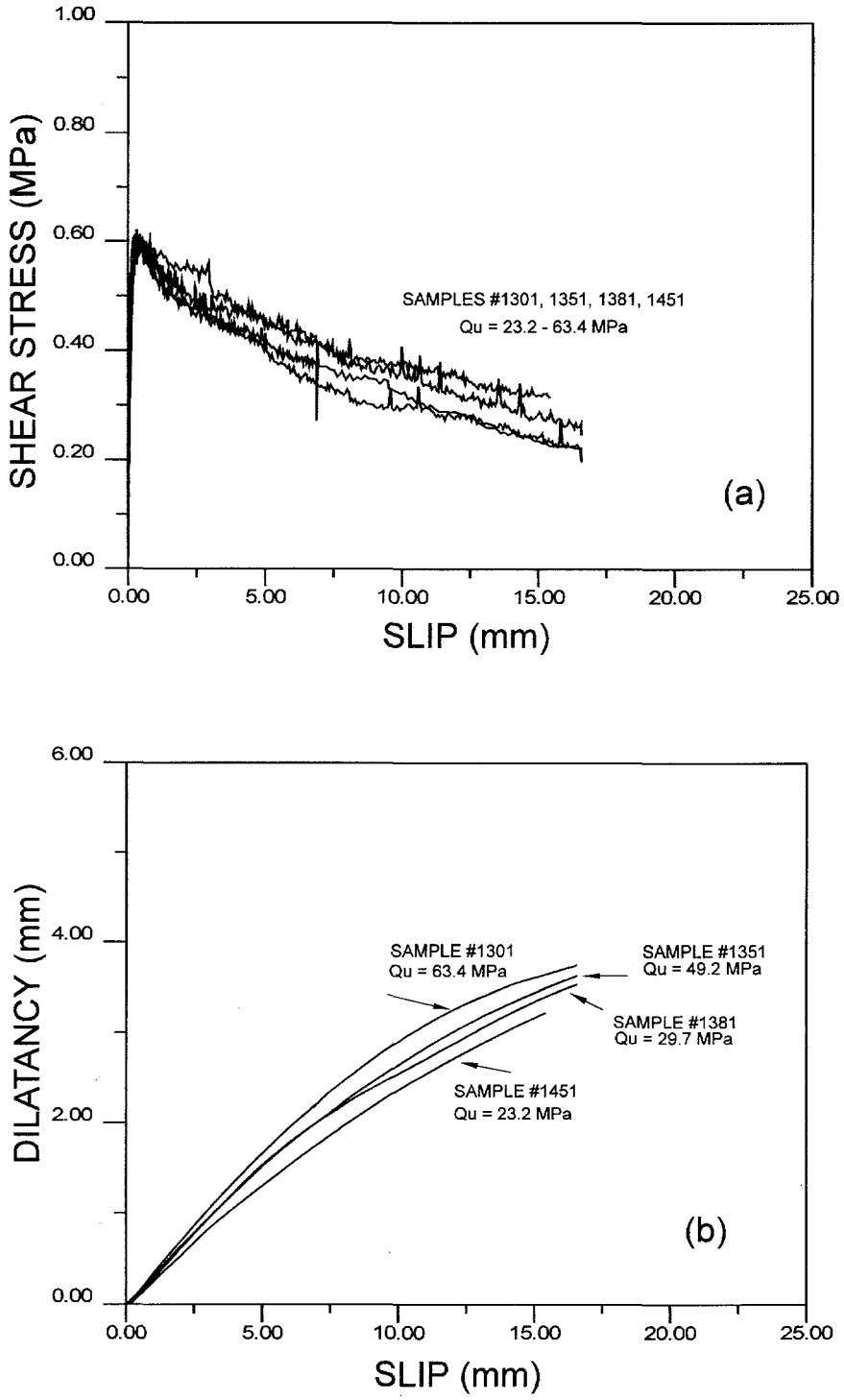

Figure 7. (a) Shear stress vs. slip, and (b) Dilatancy vs. slip response curves for four replicas of fracture #1 with different water-to-gypsum cement ratios of 30% (sample #1301), 35% (sample #1351), 38% (sample #1381) and 45% (sample #1451). All samples were tested under a constant normal stress of 0.4 MPa. Forward shear motion.

Figures 8a and 8b show, respectively, the shear stress versus slip and dilatancy versus slip response curves for forward motion for three fractures having the same 30% water-to-gypsum cement ratio and with initial JRC values of 7.7 (sample #2301), 9.4 (sample #1301) and 12.0 (sample #4301). All fractures were sheared under the same constant normal (nominal) stress of 0.4 MPa. It can be seen that the peak shear strength increases with JRC as expected. On the other hand, the effect of JRC on the dilatancy is not as clear since the dilatancy curve for JRC = 12 is located in between those for JRC = 7.7 and 9.4. This anomaly could be attributed to the fact that during rotary shearing only certain parts of the fracture may have been in contact. The scale effect of JRC plays a particular role here. Therefore, the local JRC around the contact surface affects the dilatancy rather than the global JRC which is calculated over the entire profile.

A summary of the different shear stress versus slip and dilatancy versus slip response curves for reverse shear motion can be found in Appendix D.

4. PREDICTION OF SHEAR BEHAVIOR USING BARTON'S EMPIRICAL EQUATION

The values of the peak shear stress, τ_p, were predicted using Barton's empirical equation [equation (1)], and the results were compared to the actual rotary shear test results. The value of the basic friction angle in equation (1) was taken as 30° based on the results of direct shear tests conducted on smooth surfaces of gypsum cement & reported in Wibowo et al. (1994). Table 8 gives a comparison between the peak shear stresses predicted using Barton's empirical equation and the actual test results for four replicas of fracture #1 tested under different levels of constant normal stress. The replicas have the same 30% water-to-gypsum cement ratio, and the same JCS and JRC values. It appears that for all fractures, Barton's empirical equation underestimates the peak shear strength for forward shear (Figure 9) and gives a very good estimate for reverse shear.

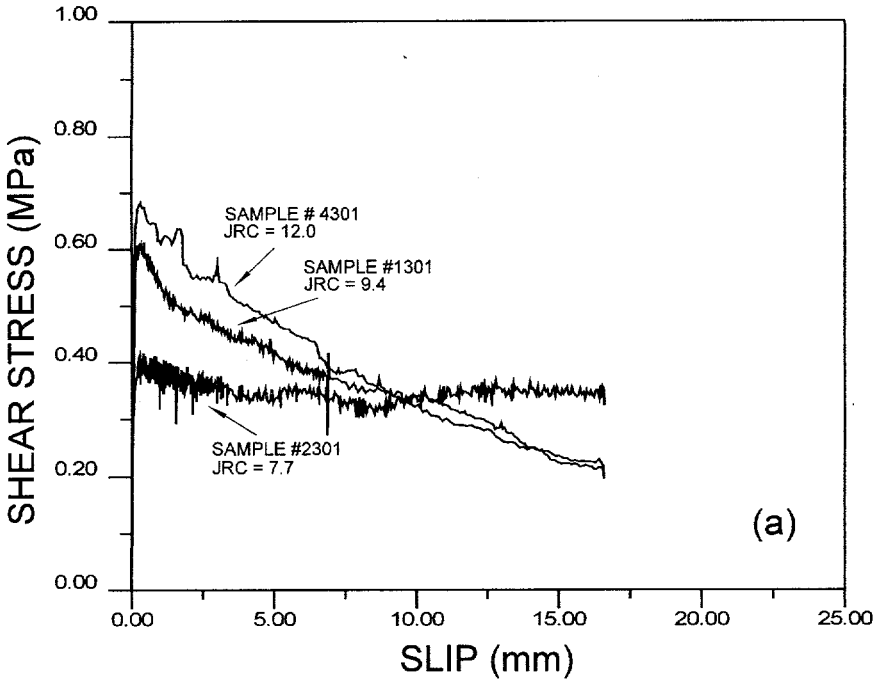

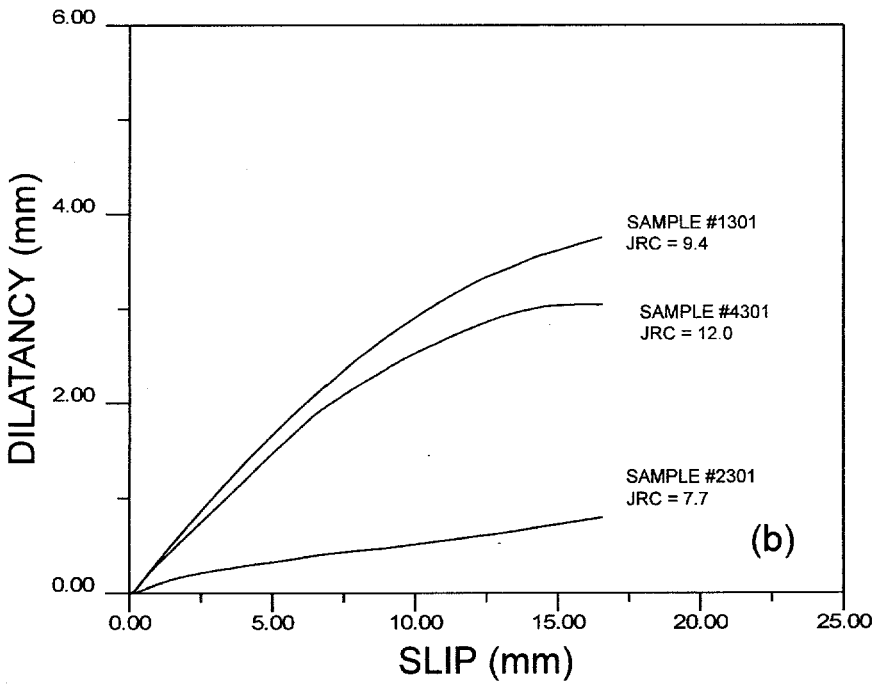

Figure 8. (a) Shear stress vs. slip and (b) dilatancy vs. slip response curves for forward motion for three fractures having the same 30% water-to-gypsum cement ratio and with initial JRC values of 7.7 (sample #2301), 9.4 (sample #1301) and 12.0 (sample #4301). All fractures were sheared under the same constant normal stress of 0.4 MPa.

Table 8

Comparison between peak shear stresses predicted using Barton's empirical equation and the actual test results for four replicas of fracture #1 tested under different levels of constant normal stress. The replicas have the same 30% water-to-gypsum cement ratio.

Sample #	σ_n (MPa)	JRC	JCS (MPa)	$JRC\log_{10}\{JCS/\sigma_n\}$ (Deg)	τ_p (Predict) (MPa)	τ_p (Forward) (MPa)	τ_p (Reverse) (MPa)
1303	0.2	9.4	63.4	23.5	0.27	0.38	0.29
1301	0.4	9.4	63.4	20.7	0.49	0.61	0.48
1302	0.8	9.4	63.4	17.9	0.89	1.14	0.90
1304	1.6	9.4	63.4	15.0	1.60	2.28	1.59

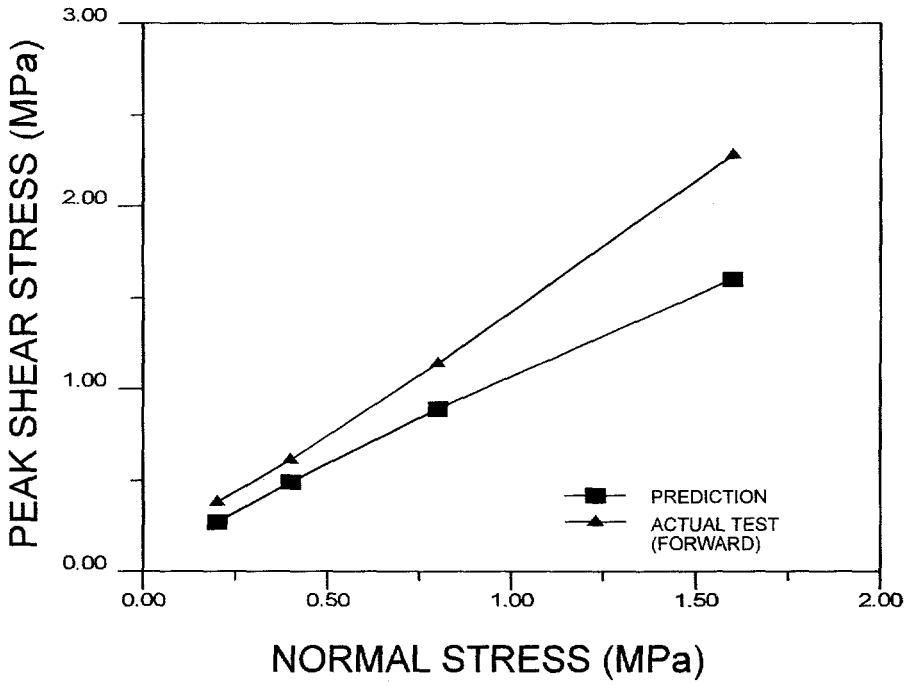

Figure 9. Predicted and observed peak shear stresses for four replicas of fracture #1 tested under different levels of constant normal stress. The replicas have the same 30% water-to-gypsum cement ratio.

Table 9

Comparison between peak shear stresses predicted using Barton's empirical equation and the actual test results for four replicas of fracture #1 tested under the same constant normal stress of 0.4 MPa. The replicas have different water-to-gypsum cement ratios.

Sample #	σ_n (MPa)	JRC	JCS (MPa)	$JRC\log_{10}\{JCS/\sigma_n\}$ (Deg)	τ_p (Predict) (MPa)	τ_p (Forward) (MPa)	τ_p (Reverse) (MPa)
1451	0.4	9.4	23.2	16.6	0.42	0.61	0.50
1381	0.4	9.4	29.7	17.6	0.44	0.59	0.54
1351	0.4	9.4	49.2	19.6	0.47	0.62	0.50
1301	0.4	9.4	63.4	20.7	0.49	0.61	0.48

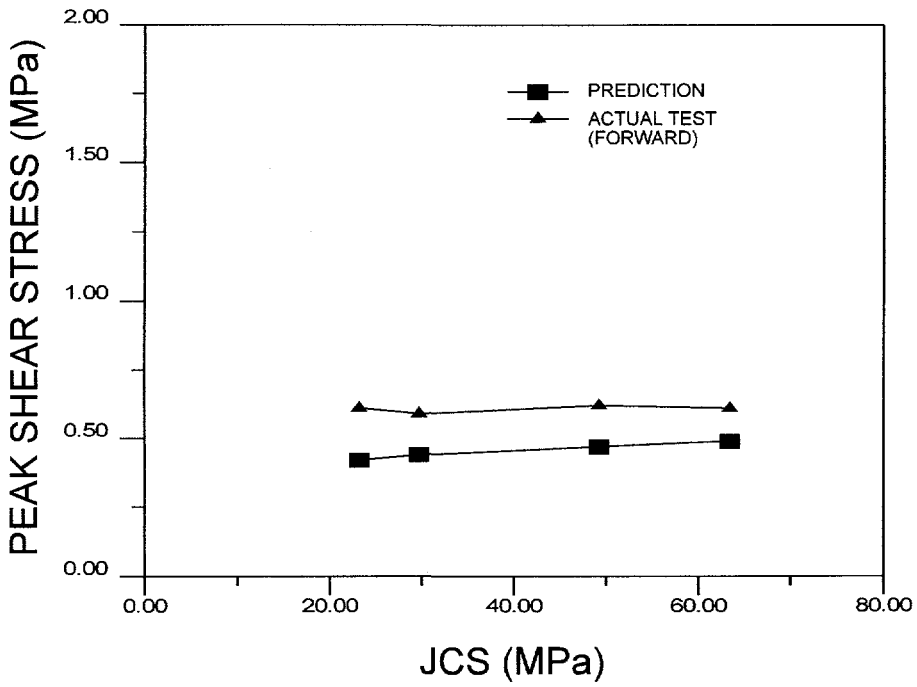

Figure 10. Predicted and observed peak shear stresses for four replicas of fracture #1 tested under the same level of constant normal stress. The replicas have different water-to-gypsum cement ratios.

Table 9 gives a comparison between the peak shear stresses predicted using Barton's empirical equation and the actual test results for four replicas of fracture #1 tested under the same constant normal (nominal) stress of 0.4 MPa and with same initial JRC value of 9.4. The fracture replicas have different water-to-gypsum cement ratios and therefore different values of JCS ranging between 23.2 and 63.4 MPa. It appears that for both forward (Figure 10) and reverse shear, the peak shear strength predictions are always less than the actual values.

Finally, Table 10 gives a comparison between the peak shear stresses predicted using Barton's empirical equation and the actual test results for three fracture replicas tested under a constant normal (nominal) stress of 0.4 MPa. The replicas have the same 30% water-to-gypsum cement ratio and therefore the same JCS, but have different JRC values. For forward shear, the peak shear strength predictions are lower than or equal to the actual test results (Figure 11). For reverse shear, the predictions are closer to the actual test results.

5. PREDICTION OF SHEAR BEHAVIOR USING FRACTURE SURFACE TOPOGRAPHY DATA

5.1 Background

A new approach is proposed below as an alternative to predict the rotary shear behavior of the tested fracture replicas. The approach is based on basic fracture properties such as fracture surface profile data and the compressive strength, modulus of elasticity, and Poisson's ratio of the fracture walls. The predictions of shear stress and dilatancy are made by following the actual physical process of shear between two rough surfaces in contact.

Table 10

Comparison between peak shear stresses predicted using Barton's empirical equation and the actual test results for three fracture replicas tested under the same constant normal stress of 0.4 MPa. The replicas have same 30% water-to-gypsum cement ratio but have different JRC values.

Sample #	σ_n (MPa)	JRC	JCS (MPa)	$JRC\log_{10}\{JCS/\sigma_n\}$ (Deg)	τ_p (Predict) (MPa)	τ_p (Forward) (MPa)	τ_p (Reverse) (MPa)
2301	0.4	7.7	63.4	16.9	0.43	0.42	0.36
1301	0.4	9.4	63.4	20.7	0.49	0.61	0.48
4301	0.4	12.0	63.4	26.4	0.60	0.68	0.58

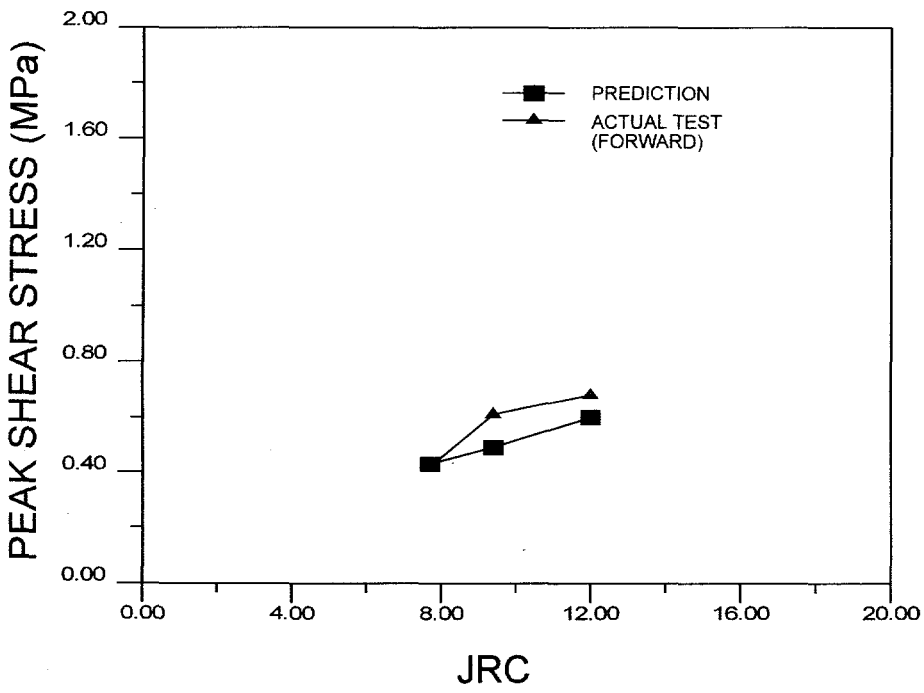

Figure 11. Predicted and observed peak shear stresses for three fracture replicas tested under the same level of constant normal stress. The replicas have different JRC values.

5.1.1 Theory of Friction

The classical adhesion theory of friction developed by Bowden and Tabor (1930) for metals, which is to a large extent based on concept of plasticity, does not apply to many geologic materials. Byerlee (1967) developed an alternative approach based on brittle fracture behavior. He considered a wedge-shaped brittle asperity such as that shown in Figure 12, which is subject to a normal force, N and a horizontal force, F. These forces create radial stresses in the asperity that can be calculated from the theory of elasticity (Timoshenko and Goodier, 1951). The radial stress, σ_{rr}, at (r,θ) is expressed as follows,

$$\sigma_{rr} = \frac{1}{rL}\left(\frac{-F\sin\theta}{\alpha - 0.5\sin 2\alpha} + \frac{N\cos\theta}{\alpha + 0.5\sin 2\alpha} \right), \qquad (8)$$

where 2α is the asperity angle and L the asperity width. For the loading shown in Figure 12, tension develops on the right-hand side of the asperity with maximum tension along the edge $\theta = \alpha$.

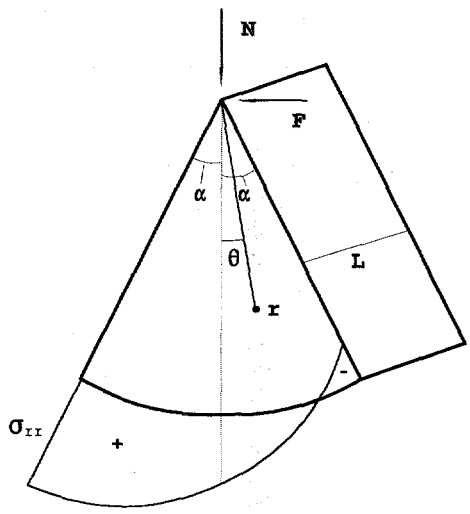

Figure 12. Single wedge under a vertical load N and a horizontal load F.

Substituting this into equation (8) and solving for r gives

$$r = \frac{1}{\sigma_{rr} L}\left(\frac{-F\sin\alpha}{\alpha - 0.5\sin 2\alpha} + \frac{N\cos\alpha}{\alpha + 0.5\sin 2\alpha} \right). \qquad (9)$$

Failure of the asperity is assumed to be brittle and to take place when the radial stress along the edge $\theta = \alpha$ is equal to the tensile strength, T, of the asperity material, that is

$$\sigma_{rr} = T. \qquad (10)$$

For most hard rocks, Hoek (1968, after Hoek and Bray, 1981) has suggested that the tensile strength is approximately equal to 10% of the unconfined compressive strength. The coefficient of friction μ can be calculated as follows

$$\mu = \frac{\tau}{\sigma_n} = \frac{F}{N}. \qquad (11)$$

Substituting equations (10) and (11) into equation (9), the value of r for which σ_{rr} = T, is equal to

$$r_d = \frac{N}{TL}\left(\frac{-\mu\sin\alpha}{\alpha - 0.5\sin 2\alpha} + \frac{\cos\alpha}{\alpha + 0.5\sin 2\alpha} \right), \qquad (12)$$

The area of asperity damage, a, is then equal to

$$a = 2\, r_d\, L \sin\alpha \qquad (13)$$

and the percentage of damaged area to the total joint cross-sectional area (A) is

$$t = \frac{a}{A} \tag{14}$$

5.1.2 Asperity Slope and Type of Failure

Newland and Allely (1957) indicated that irregularities along the failure surface of a sand specimen has an important influence on its shear strength. When two particles of sand are in contact with an angle of contact,i, as shear takes place the grains will rise on top of one another along that contact (dilatancy). The angle, i, contributes to the shear strength of the sand.

Patton (1966) extended this formulation to evaluate the shear behavior of artificial rock joint surfaces with different angles of saw tooth asperities. After performing about 300 direct shear experiments, Patton found that the equation describing the shear strength failure envelope can be expressed as a bilinear equation. Under relatively low normal loads, sliding friction failure occurs, and the initial part of the failure envelope is expressed as follows

$$S = N \tan(\phi + i) \tag{15}$$

where S is the sliding friction load, N is the applied normal load, ϕ is the base friction angle, and i is the angle of the surfaces in contact.

Under relatively high normal loads, shear failure takes place across the asperities, and the asperity angle, i, does not influence the shear strength anymore. The value of the local shear load can be expressed as follows,

$$S = \tau_r A_{ls}, \tag{16}$$

where τ_r is the local shear strength of the intact material, and A_{ls} is the area over which shearing occurs. In this report, the shear strength, τ_r, of the intact material is assumed to follow the failure criterion for intact rock proposed by Fairhurst (1964),

$$\tau_r = q_u \frac{\sqrt{(1-n)}-1}{n}\left(1+n\frac{\sigma_n}{q_u}\right), \qquad (17)$$

where q_u is the unconfined compressive strength of the intact material, n is the ratio between the rock compressive and tensile strengths (assumed equal to 10, as suggested by Hoek [1968, after Hoek and Bray (1981)] for most of hard rocks), and σ_n is the local normal stress.

At any contact position during shear, the type of failure can be evaluated. Whether or not shear failure occurs can be determined by comparing the horizontal sliding friction force calculated using equation (15) to the intact shear resistance calculated using equation (16).

5.1.3 Bearing Area Curve and Composite Topography

One way to describe joint surface roughness is by using a bearing area curve. The bearing curve was first introduced by Abbot and Firestone (1933). Consider a rough surface, as shown in Figure 13a, whose asperities are in contact with a horizontal flat surface. Suppose that the asperity tips have worn to a depth, x1, leaving two flat surfaces of width a1 and c1. These surfaces form two contact areas against the horizontal plate. The bearing curve at depth x1 is equal to a1 + c1. The bearing curve can be constructed for other depths as shown in Figure 13b.

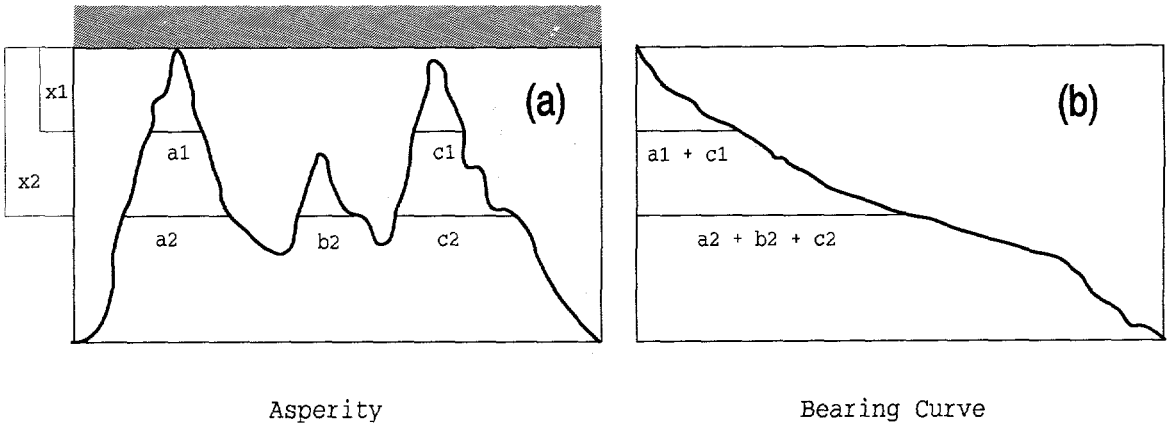

Figure 13. Abbot's bearing area curve concept.

While studying the effect of "matedness" on the behavior of rock joints, Brown and Scholz (1986) introduced the concept of composite topography for unmated joints. Basically, the composite topography of two rough surfaces in contact is the inverted aperture between the two surfaces. This concept is extended below for determining the micro-damage of joint surface contact which influences the value of dilatancy. The analysis of two rough surfaces in contact is replaced by the analysis of the composite topography of the two surfaces against a flat and stiff surface.

5.1.4 Elastic Displacement of Contact Asperities

The elastic displacement that occurs when two asperities in contact are subject to a normal load can be determined using Hertzian contact theory (Lubkin, 1962). Assuming that the two contacting asperities are modelled as two cylinders with radii R_1 and R_2, as shown in Figure 14, the asperity contact area, 2b, can be expressed as follows

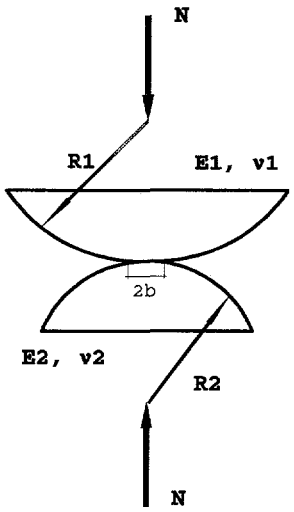

Figure 14. Hertzian contact of two cylinders.

$$2b = \sqrt{\frac{16NR_o}{\pi E_o}}, \tag{18}$$

where N is the normal load per unit length of cylinder, $1/R_0$ is equal to $1/R_1 + 1/R_2$, $1/E_0$ is equal to $(1-\upsilon^2)/E_1 + (1-\upsilon^2)/E_2$, E_1 is the Young's Modulus of the 1st cylinder, and E_2 is the Young's Modulus of the 2nd cylinder.

The displacements of the centers of the two cylinders in the loading direction are equal to

$$\delta_1 = \frac{N(1-\nu^2)}{\pi E_1} \ln\left(\frac{4R_1}{b} - \frac{1}{2}\right), \tag{19}$$

and

$$\delta_2 = \frac{N(1-\nu^2)}{\pi E_2} \ln\left(\frac{4R_2}{b} - \frac{1}{2}\right), \tag{20}$$

respectively. The total elastic displacement is then equal to

$$\delta = \delta_1 + \delta_2 \qquad (21)$$

5.2 Procedure for Predicting Shear Behavior

The concepts summarized in section 5.1 can be combined to predict the shear and dilatancy behavior of two rough surfaces in contact. This is applied here to the rotary shear tests.

5.2.1 Checking the Mode of Failure

During rotary shear, the top and bottom surfaces of each fracture are held firmly by the machine and stay horizontal. Thus, for a given amount of rotation, the top and bottom surfaces have only one point of contact. The slope angle, i, of that contact can be determined once the surface topographies are known. The local horizontal sliding friction force can be calculated using equation (15). The local shear area, A_{ls}, can also be determined and the local intact shear resistance can be calculated using equation (16). The type of failure can then be evaluated whether it is sliding friction or intact shear failure by comparing the horizontal sliding friction force with the local intact shear resistance.

5.2.2 Sliding Friction Failure

Shear Prediction

If sliding friction failure occurs, the value of the local horizontal sliding force becomes the local shear load. Since only one surface contact occurs at a given time, the value of the global shear load is equal to the value of the local shear load. The value of the global shear stress for a particular shear displacement or

slip is equal to the global shear load divided by the total joint fracture area.

Dilatancy Prediction

For a particular amount of rotational shear, the composite topography of the top and bottom fracture surfaces can be determined and the bearing area curve constructed following the procedure mentioned in Section 5.1.3. Assuming that each surface asperity can be modelled as a wedge, the damage area can be calculated using equations (12) and (13). By combining the damage area and the bearing area curve, the thickness of damage can be determined. Using the Hertzian contact theory, the elastic displacement of the asperity can be determined using equations (18) through (21). The amount of dilatancy because of geometry only can be determined by recording the vertical movement of reference points on the top and bottom parts of the fractures. The final value of dilatancy is equal to the dilatancy due to geometry subtracted by the damage and elastic displacement.

5.2.3 Shear Failure

If shear failure occurs across an asperity, the value of the local shear load is now equal to the local intact shear resistance. The value of the local dilatancy is practically zero.

5.2.4 Final Prediction Results

Global shear stress and dilatancy responses at a particular slip can be predicted. The process of calculation is continued for another step of slip. Since three annular profiles are measured for each fracture, shear and dilatancy predictions can be done for each annular profile. The final result is the average of the three calculations.

5.2.5 Flowchart for Predicting Shear Behavior

Figure 15 shows a flowchart of the procedure for predicting shear behavior. The input data are top and bottom profiles in mated position, material properties (i.e., modulus of elasticity, Poisson's ratio, and unconfined compressive strength), steps of shear displacement or slip, and a number of steps to reach maximum slip. The processes of looping follow the procedure mentioned in Sections 5.2.1 through 5.2.4. The final results are shear stress versus slip and dilatancy versus slip curves.

5.2.6 Example

The process of shearing of fracture #1 is simulated in Figures 16 to 18. Figure 16a shows that the bottom and top surfaces of fracture #1 are initially in a mated position. Figure 16b gives the corresponding bearing curve. In this figure, the bearing curve is expressed as the proportional bearing curve, tp, which is the ratio (or percentage) between its length, np, and the total profile length, l (Kragelsky, 1982). After 1 and 10 mm of slip, Figures 17a and b, and Figures 18a and b show respectively the contact of the two surfaces of fracture #1 and the corresponding bearing area curves. Figures 16 through 18 show that during rotary shear, surface contact occurs only on a fraction of the overall fracture surface profile. Only certain parts of the fracture around the contact area control the shear stress and dilatancy behavior. A complete set of shear processes for fracture profiles #1, 2, and 4 can be found in Appendix E.

5.3 Comparison between Predicted and Actual Shear Behavior

Predictions were made for four replicas of fracture #1, with same water-to-gypsum cement ratio of 30%, and tested under constant normal stresses of 0.2, 0.4, 0.8, and 1.6 MPa, respectively. Comparison between predictions and actual test results can be found in Figures 19a and 19b. Predicted and measured shear stress versus

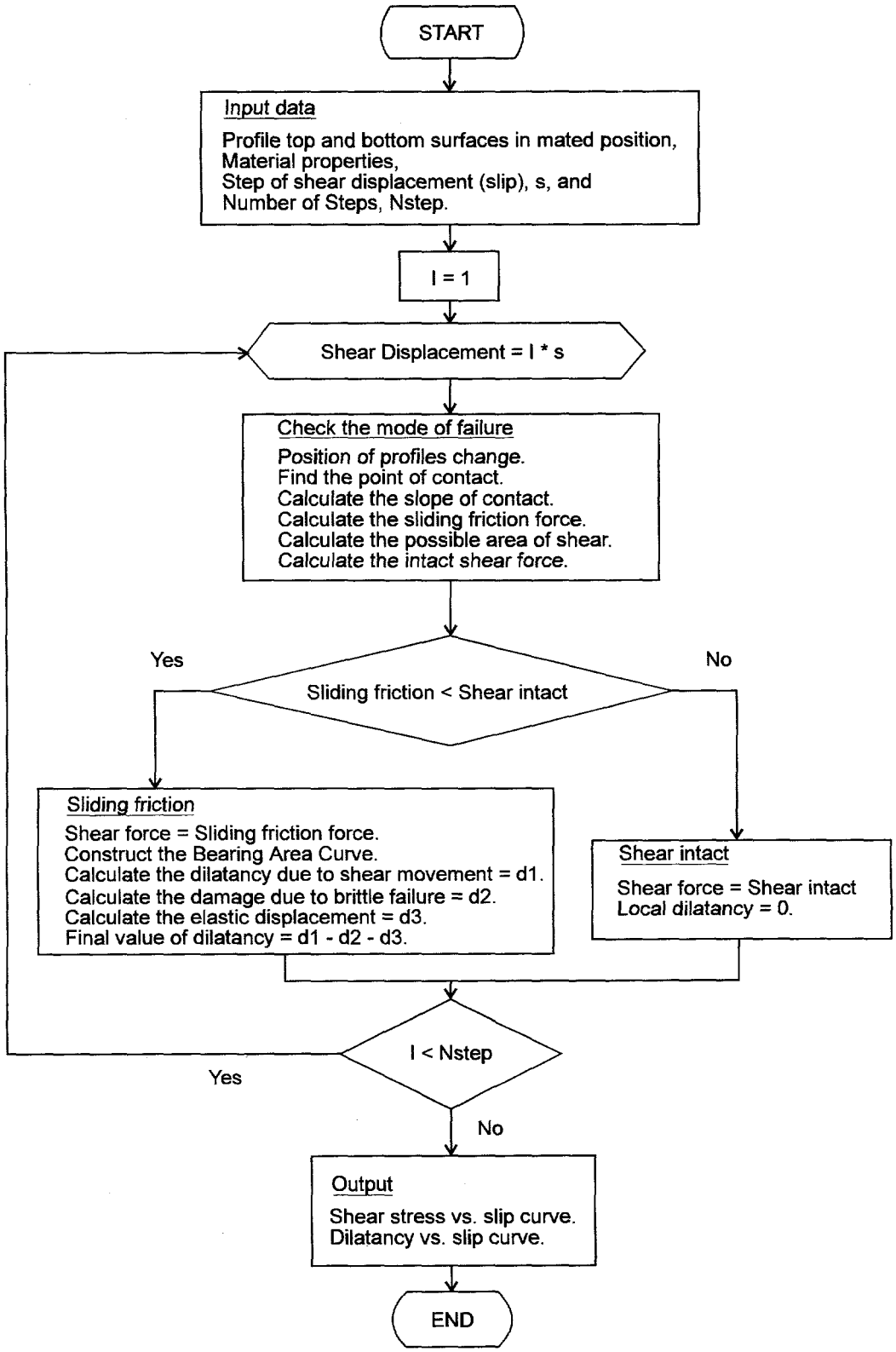

Figure 15. Flowchart for predicting shear behavior.

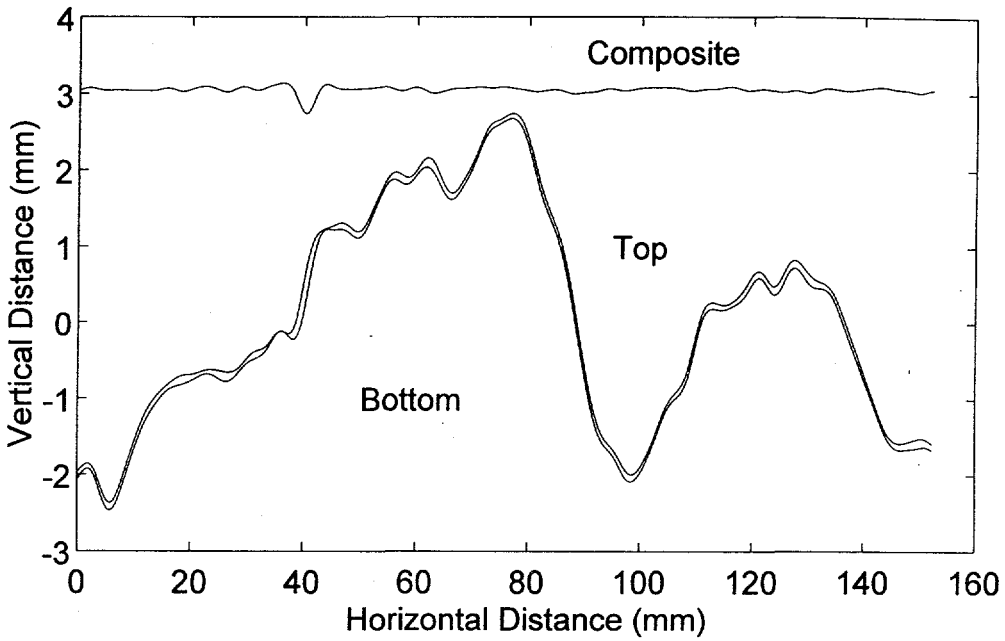

(a)

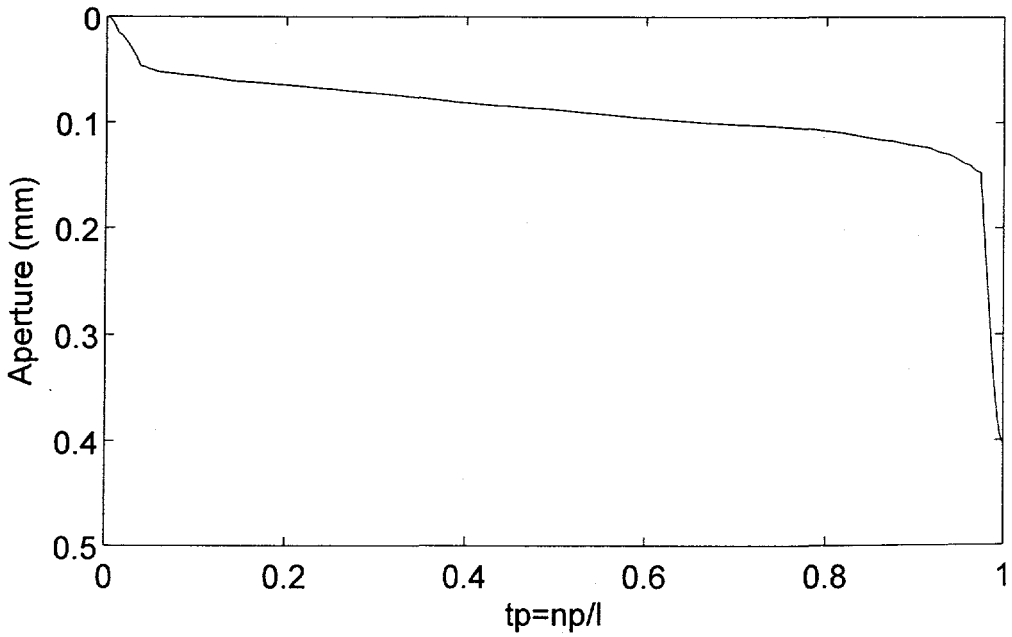

(b)

Figure 16. (a) Bottom, top, and composite topography, and (b) Bearing area curve for fracture #1 in a mated position.

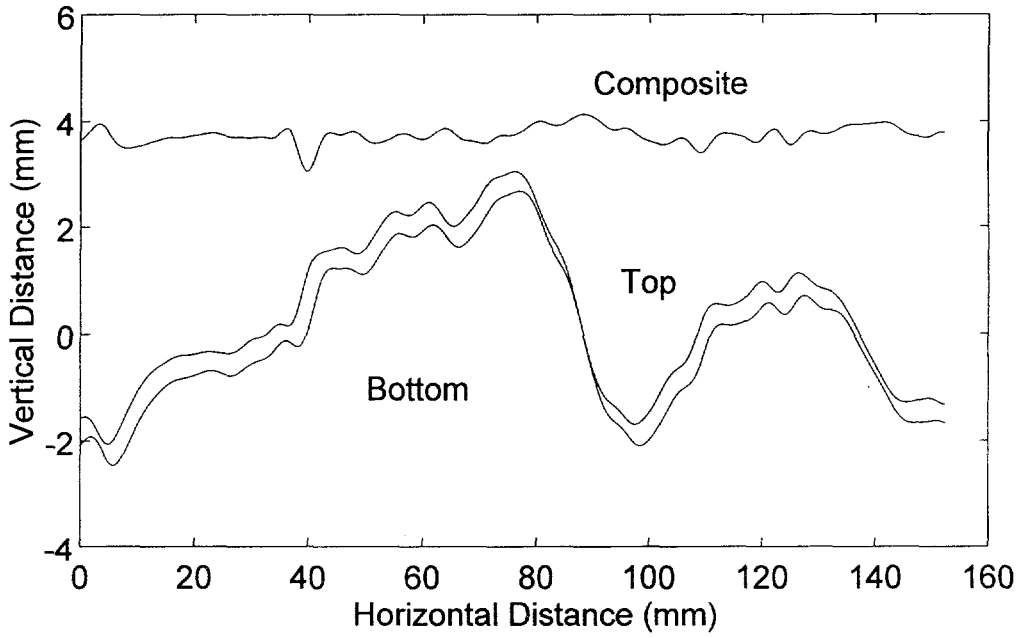

(a)

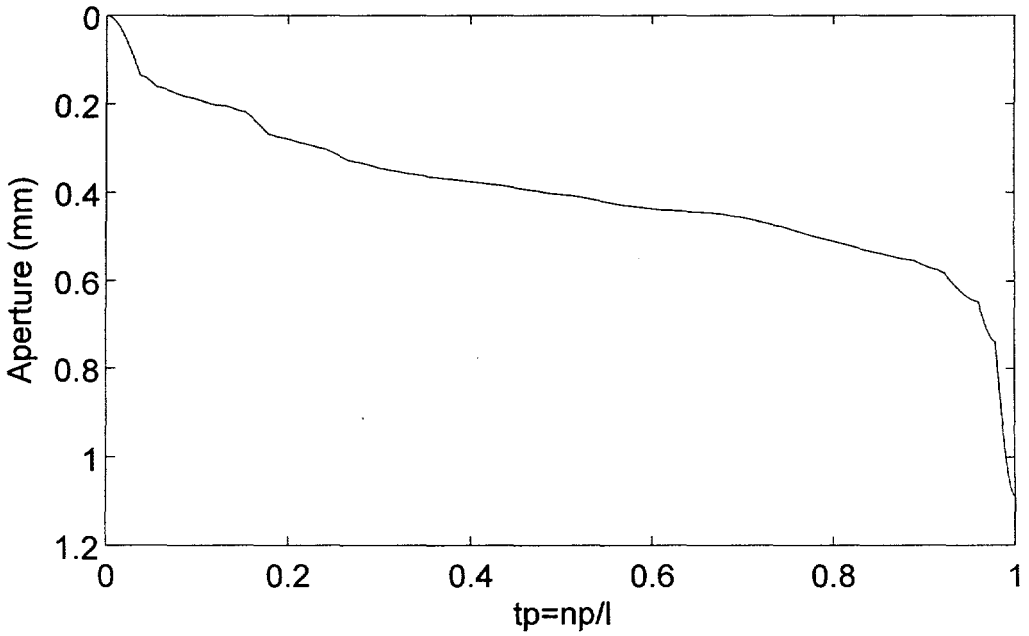

(b)

Figure 17. (a) Bottom, top, and composite topography, and (b) Bearing area curve for fracture #1 after 1 mm of slip.

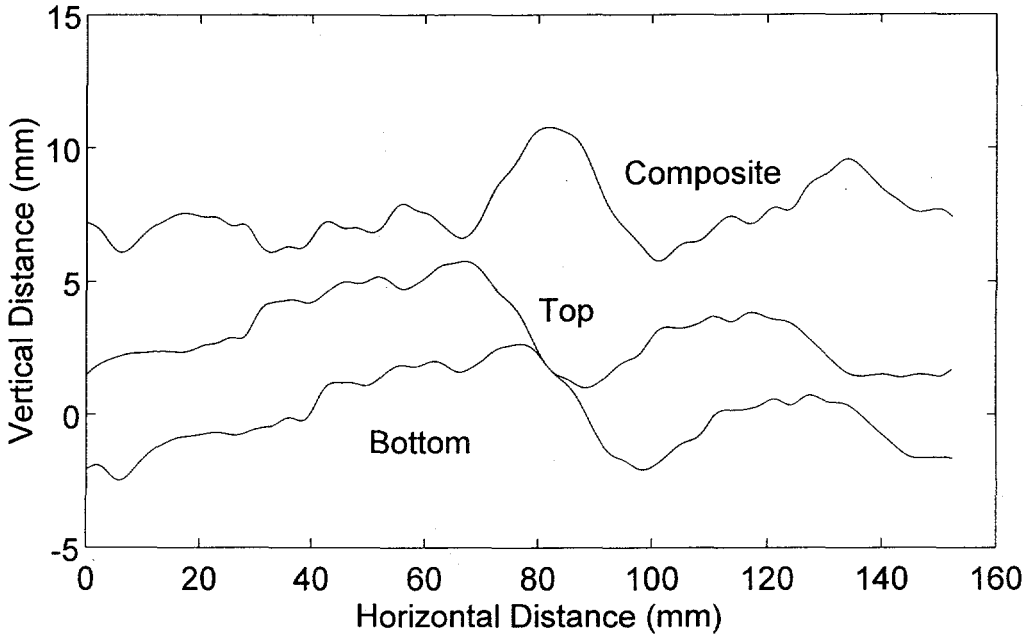

(a)

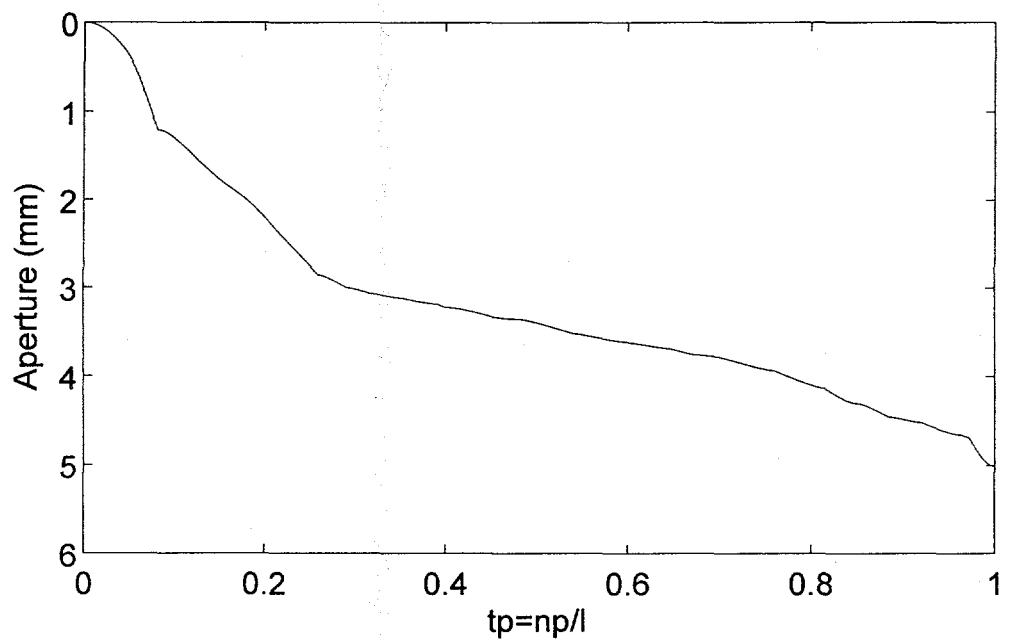

(b)

Figure 18. (a) Bottom, top, and composite topography, and (b) Bearing area curve for fracture #1 after 10 mm of slip.

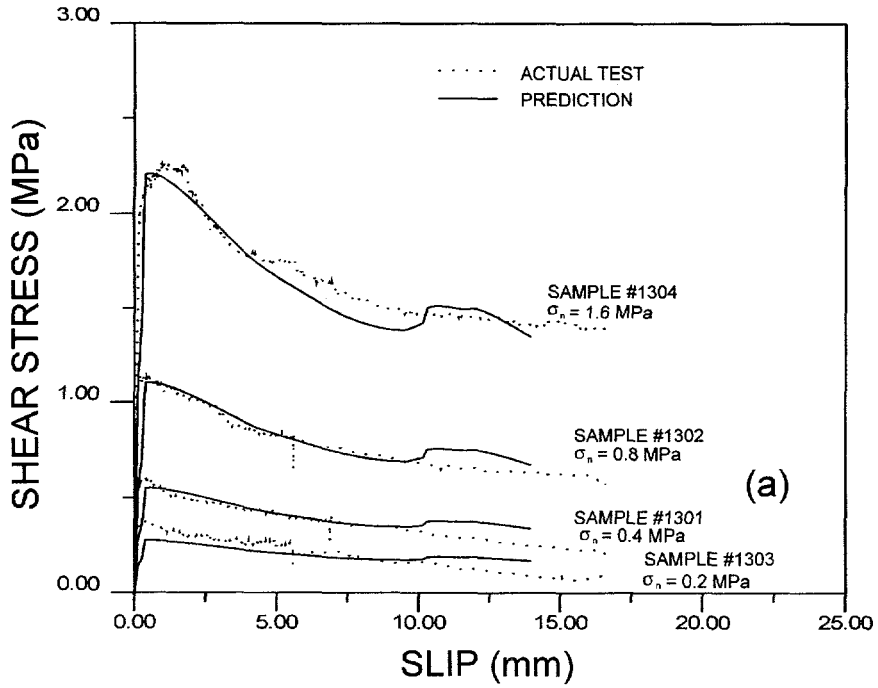

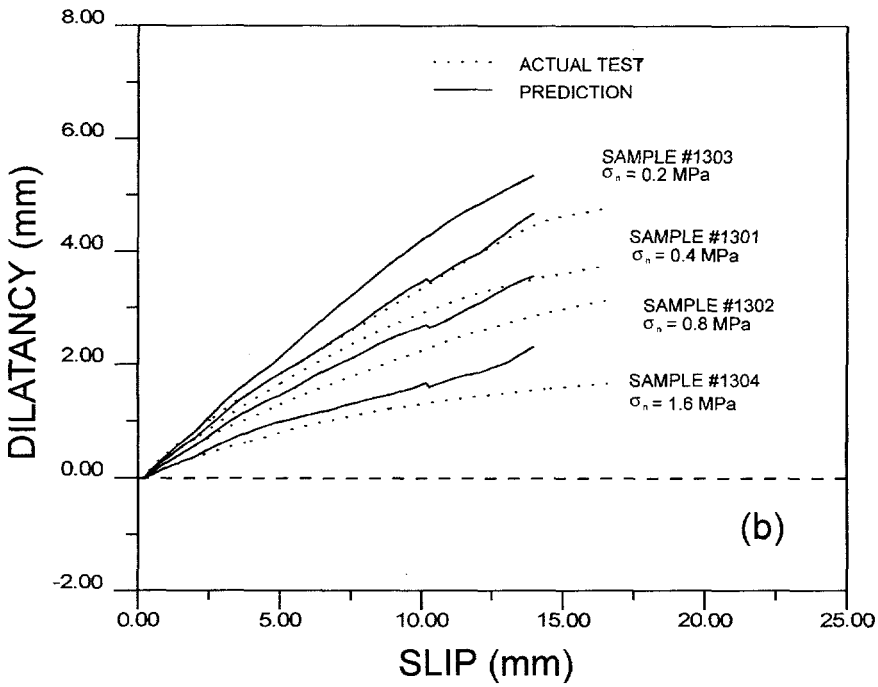

Figure 19. Predicted and observed (a) Shear stress vs. slip, and (b) Dilatancy vs. slip response curves for four replicas of fracture #1 with same 30% water-to-gypsum cement ratio. All replicas were tested under different levels of applied normal stress. Forward shear motion.

slip response curves agree well. Predicted and measured dilatancy versus slip curves look similar but the predicted dilatancy is always larger than the measured dilatancy.

A second set of predictions was made for four replicas of fracture #1 with water-to-gypsum cement ratios of 30, 35, 38, and 45% respectively and tested under the same constant normal stress of 0.4 MPa. Predicted and observed shear versus slip and dilatancy versus slip response curves are shown in Figures 20a and 20b, respectively. Both predictions and observations indicate that the water-to-gypsum cement ratio and therefore the strength of the fracture walls does not have much of an effect on the shear behavior. Both predictions and observations also show that dilatancy decreases slightly as the water-to-gypsum cement ratio increases and therefore the strength decreases. As in Figure 19b, dilatancy predictions are higher than the observed dilatancy for values of the water-to-gypsum cement ratio of 30 and 35%. For water-to-gypsum cement ratios of 38 and 45%, both predicted and observed dilatancy curves agree quite well.

The third set of predictions was carried out for fractures #1, 2, and 4 with JRC values of 9.4, 7.7, and 12, respectively. Predicted and observed shear versus slip and dilatancy versus slip response curves are shown in Figures 21a and 21b, respectively. Compared to the actual test results, the shear strength predictions are reasonable for the fractures with JRC values of 12 and 9.4. For the fracture with a JRC of 7.7, the predictions are much less than the actual values. The predictions tend to overestimate slightly the fracture dilatancy behavior. This behavior is probably due to the fact that the deformation applied in this procedure is assumed as elastic deformation (no plastic deformation).

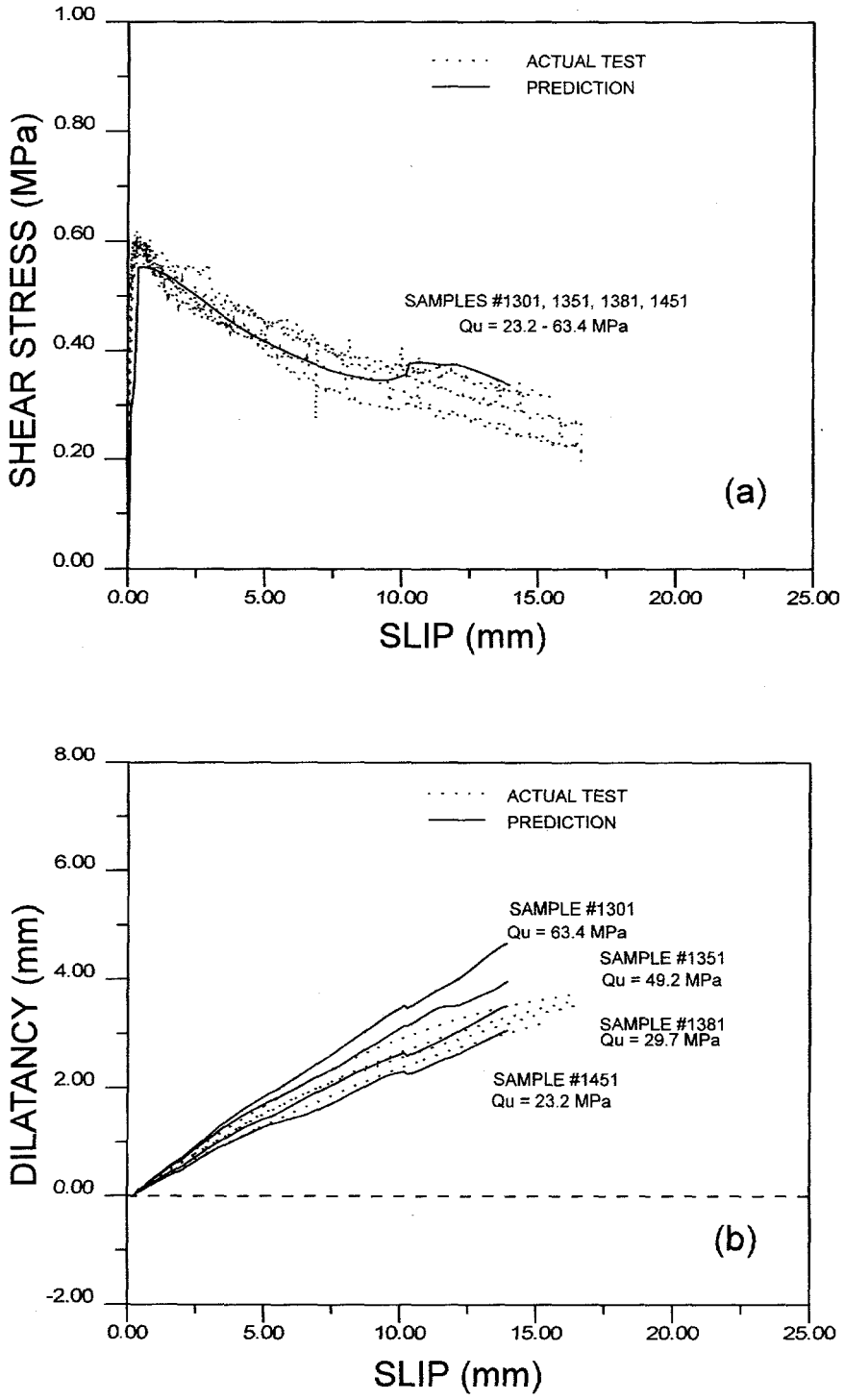

Figure 20. Predicted and observed (a) Shear stress vs. slip, and (b) Dilatancy vs. slip response curves for four replicas of fracture #1 with different water-to-gypsum cement ratios of 30, 35, 38, and 45%. All samples were tested under a constant normal stress of 0.4 MPa. Forward shear motion.

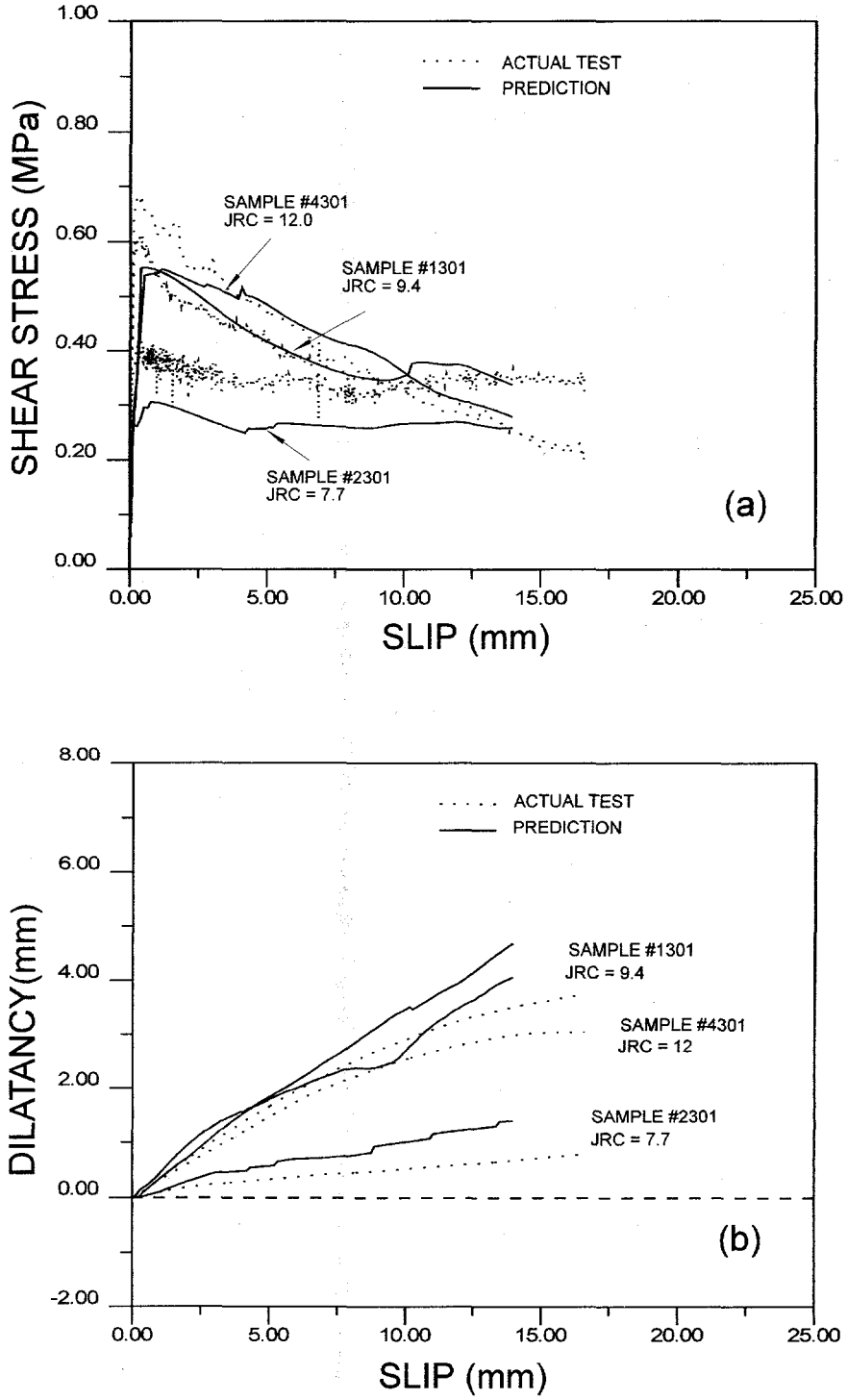

Figure 21. Predicted and observed (a) Shear stress vs. slip, and (b) Dilatancy vs. slip response curves for three fractures having the same 30% water-to-gypsum cement ratio and with initial JRC values of 7.7, 9.4, and 12.0. All fractures were sheared under the same constant normal stress of 0.4 MPa. Forward shear motion.

6. CONCLUDING REMARKS

Several concluding remarks can be made from the work reported in this report:

1. When using equation (2), the JRC values are determined using all the fracture profile data. On the other hand, experimental observations seem to indicate that only certain portions of the profiles around the points of contact directly influence the fracture shear behavior.

2. For the three fractures, Barton's empirical equation underestimates the peak shear strength for forward shear, however it gives a good estimate for reverse shear. The JRC standard profile gives an estimated coefficient of roughness without considering the direction of shear, which behaves differently.

3. The joint wall compressive strength (JCS) does not seem to have a significant role in the rotary shear behavior under relatively low applied normal stresses.

4. An alternative procedure was developed for predicting the rotary shear behavior of fractures based on fracture surface profile data and the compressive strength, modulus of elasticity, and Poisson's ratio of the fracture walls. In this procedure, fracture surface asperities are assumed to fail in a brittle manner. Reasonably good predictions of shear and dilatancy behavior were obtained.

7. REFERENCES

Abbot, E. J., and F. A. Firestone, 1933. Specifying Surface Quality. Mechanical Engineering, Vol. 55, pp. 569-572.

Barton, N., 1976. Rock Mechanics Review, The Shear Strength of Rock and Rock Joints. Int. J. Rock Mech. Min. Sci & Geomech. Abstr., Vol. 13, pp. 255-279.

Barton, N., and S. Bandis, 1990. Review of Predictive Capabilities of JRC-JCS Model in Engineering Practice. Proc. Int. Conf. on Rock

Joints, pp. 603-610. Loen, Norway.

Barton, N., and V. Choubey, 1977. The Shear Strength of Rock Joints in Theory and Practice. Rock Mechanics, 10, pp. 1-54.

Bowden, F. P., and D. Tabor, 1950. The Friction and Lubrication of Solids. Clarendon Press, Oxford.

Brown, S. R., and C. H. Scholz, 1986. Closure of Rock Joints. Journal of Geophysical Research, Vol. 91, No. B5, pp. 4939-4948.

Byerlee, J. D., 1967. Theory of Friction Based on Brittle Fracture. Journal of Applied Physics, Vol. 38, No. 7, pp. 2928-2934.

Fairhurst, C., 1964. On the Validity of Brazilian Tests for Brittle Materials. Int. J. Rock Mech. Min. Sci & Geomech. Abstr., Vol. 1, pp. 535-546.

Holcomb, D. J., and A. K. Jones, 1982. Data Acquisition for the Rock Mechanics Laboratories. SAND 83-0646, Sandia National Laboratories, Albuquerque, NM.

Huang, C., I. White, E. G. Thwaite, and A. Bendeli, 1988. A Noncontact Laser System for Measuring Soil Surface Topography. Soil Sci. Soc. Am. J. Vol. 52, pp. 350-355.

ISRM, 1981. Suggested Methods For Rock Characterization, Testing, and Monitoring. ISRM Commission on Testing Methods, E. T. Brown, Ed. Pergamon Press, Oxford.

Kragelsky, I. V., M. N. Dobychin, and V. S. Kombalov, 1982. Friction and Wear, Calculation Methods. Pergamon Press, Oxford.

Lubkin, J. L., 1962. Contact Problems. Handbook of Engineering Mechanics, W. Flügge ed. McGraw-Hill, New York, pp. 42.1-42.12.

Newland, P. L., and B. H. Allely, 1957. Volume Changes in Drained Triaxial Tests on Granular Materials. Geotechnique, Vol. VII, pp. 17-34.

Olsson, W. A., 1987. Rock Joint Compliance Studies. SAND 86-0177, Sandia National Laboratories, Albuquerque, NM.

Patton, F. D., 1966. Multiple Modes of Shear Failure in Rock. Proceedings of the 1st Int. Congress of Rock Mechanics, Lisbon, Vol. 1, pp. 509-513.

Tabor, D., 1951. The Hardness of Metals, Clarendon Press, Oxford.

Timoshenko, S. P., and J. N. Goodier, 1970. Theory of Elasticity. McGraw-Hill, New York, pp. 109-112.

Tse, R., and D. M. Cruden, D. M., 1979. Estimating Joint Roughness Coefficients. Int. J. Rock Mech. Min. Sci & Geomech. Abstr., Vol. 16, pp. 303-307.

Yu, X., and B. Vayssade, 1991. Technical Note: Joint Profiles and Their Roughness Parameter. Int. J. Rock Mech. Min. Sci & Geomech. Abstr., Vol. 28, pp. 333-336.

Wibowo, J., B. Amadei, S. Sture, and R. H. Price, 1994. Effect of Boundary Condition on the Strength and Deformability of Replicas of Natural Fractures in Welded Tuff: Data Analysis. SAND 93-7079. Sandia National Laboratories, Albuquerque, NM.

APPENDICES

CONTENT

APPENDIX A

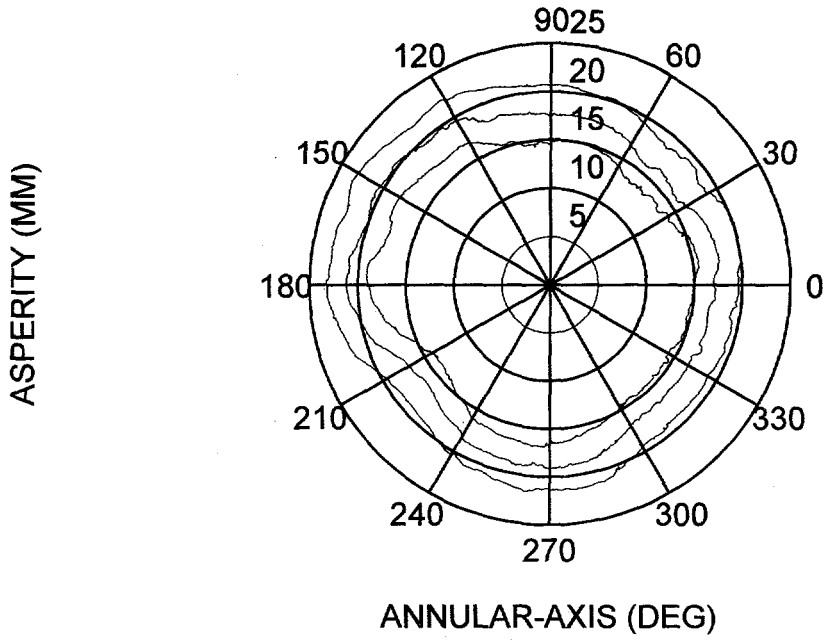

Annular topography of bottom part of fracture #1.

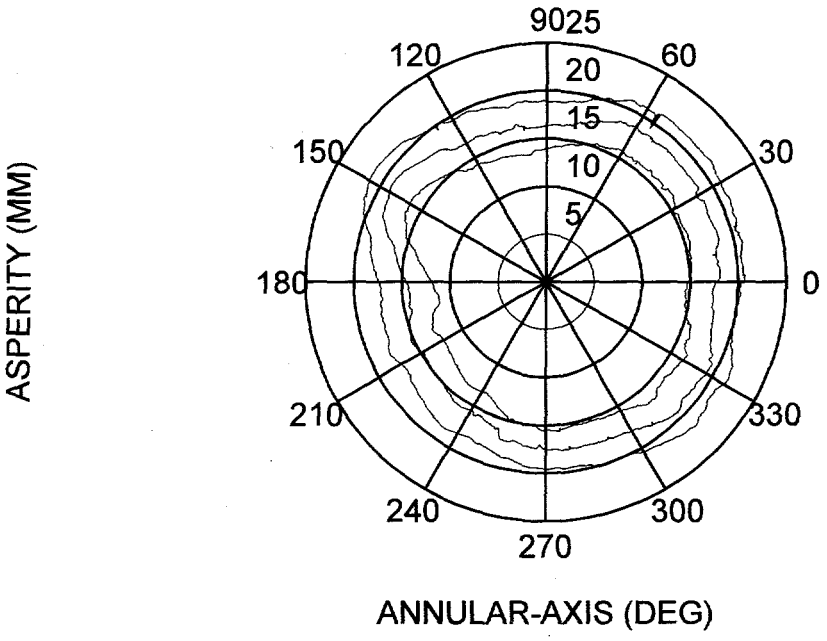

Annular topography of top part of fracture #1.

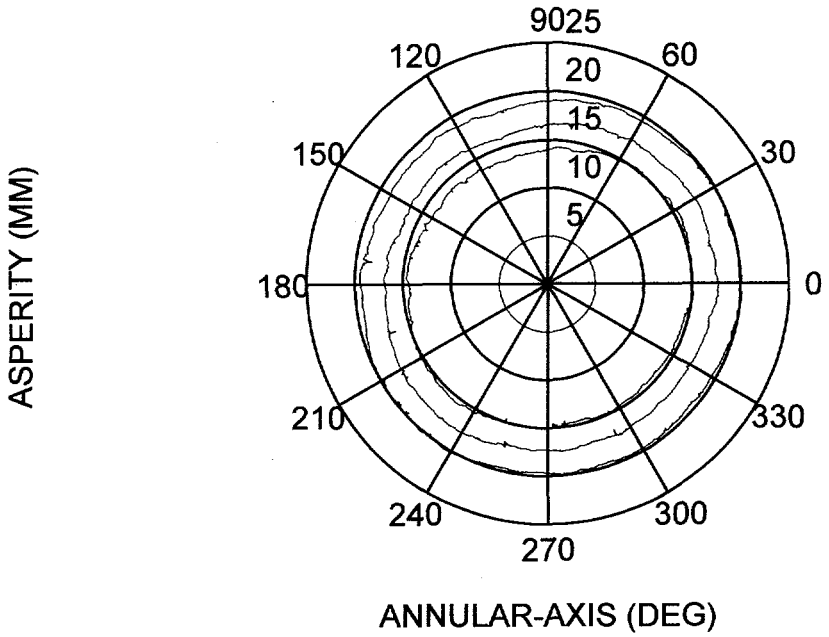

Annular topography of bottom part of fracture #2.

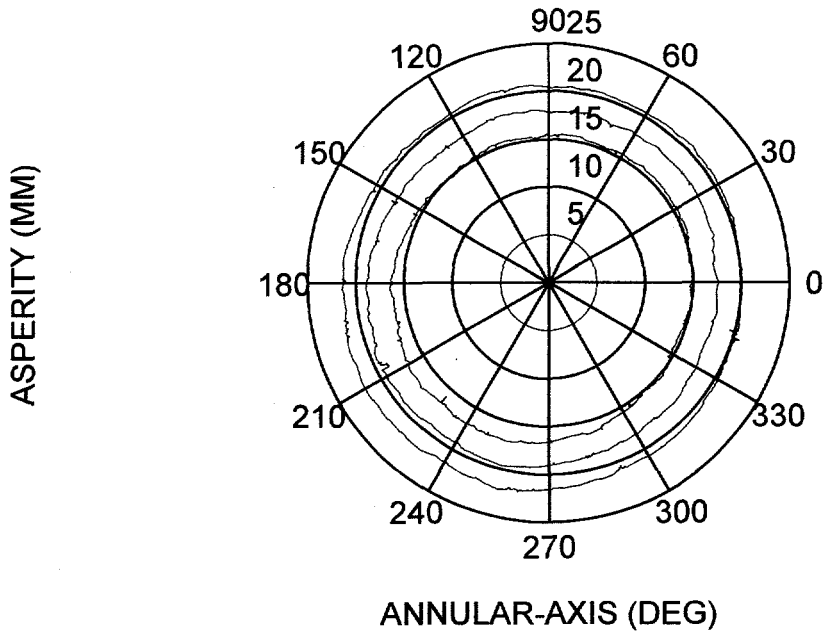

Annular topography of top part of fracture #2.

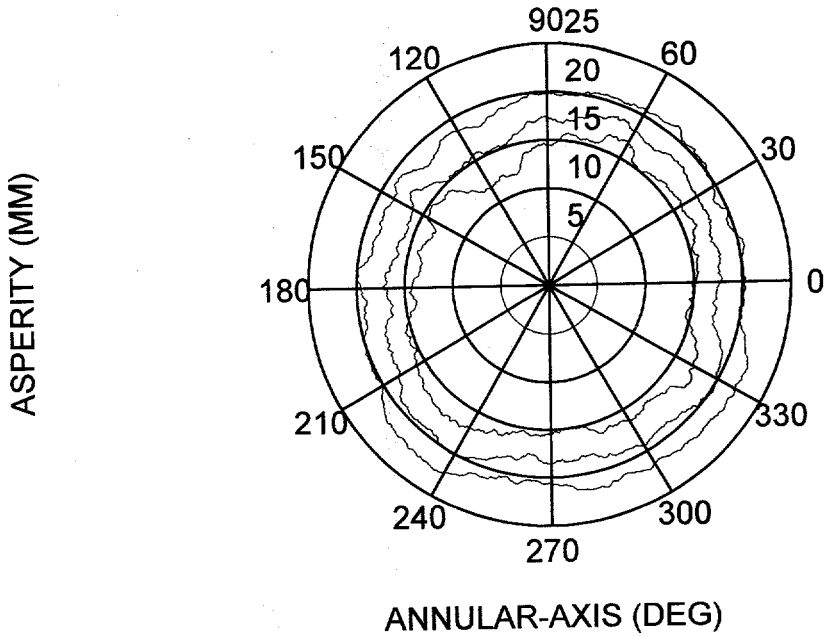

Annular topography of bottom part of fracture #3.

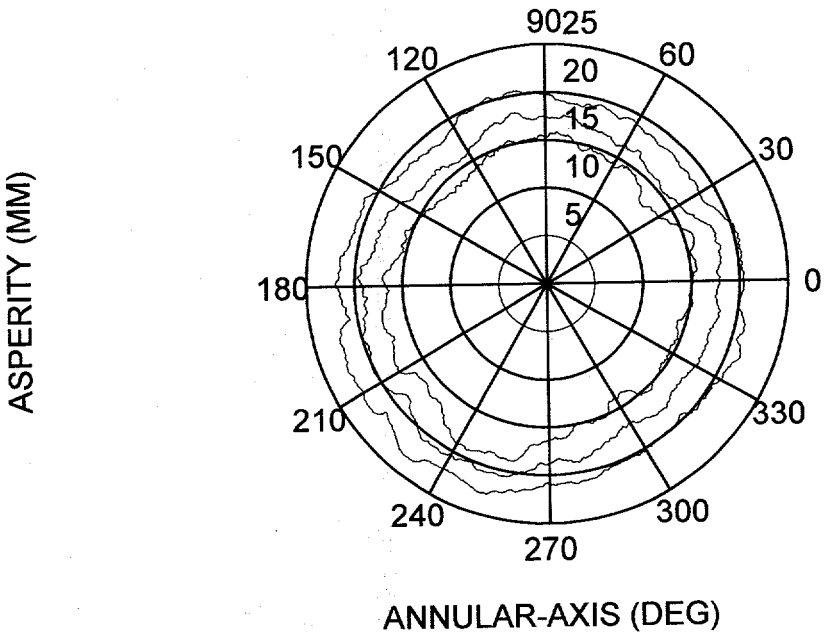

Annular topography of top part of fracture #3.

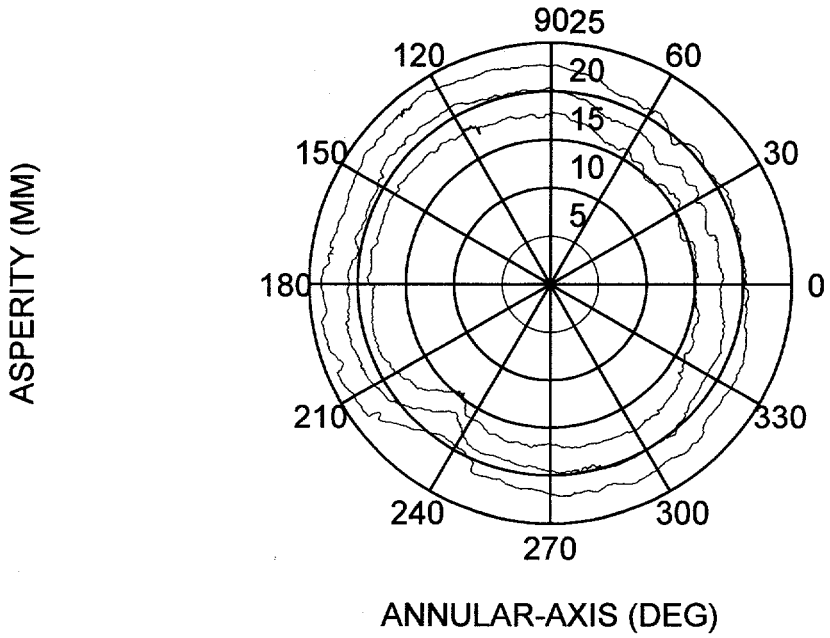

Annular topography of bottom part of fracture #4.

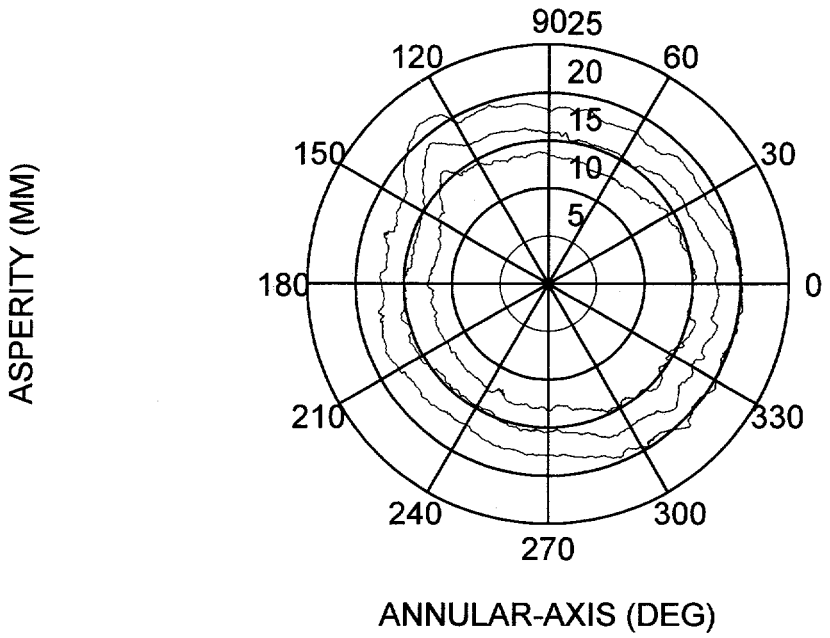

Annular topography of top part of fracture #4.

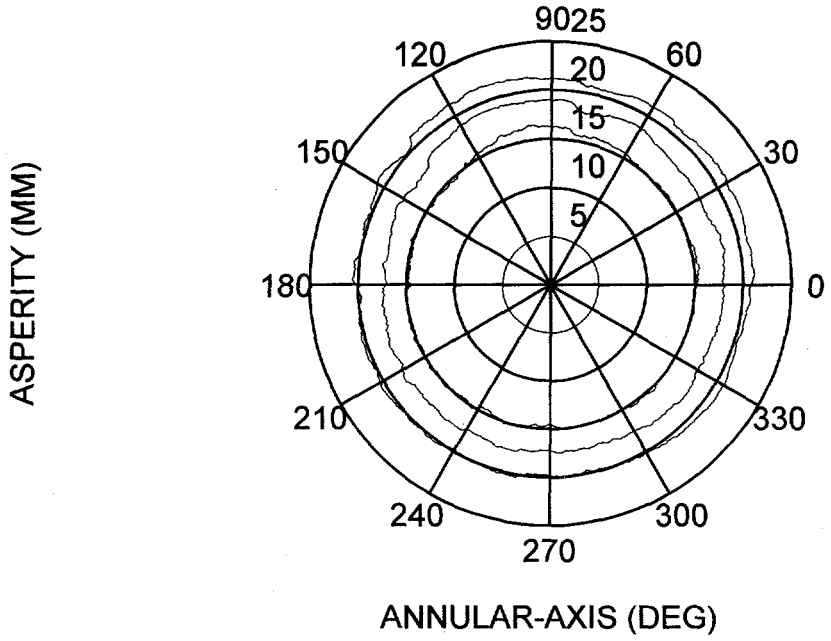

Annular topography of bottom part of fracture #5.

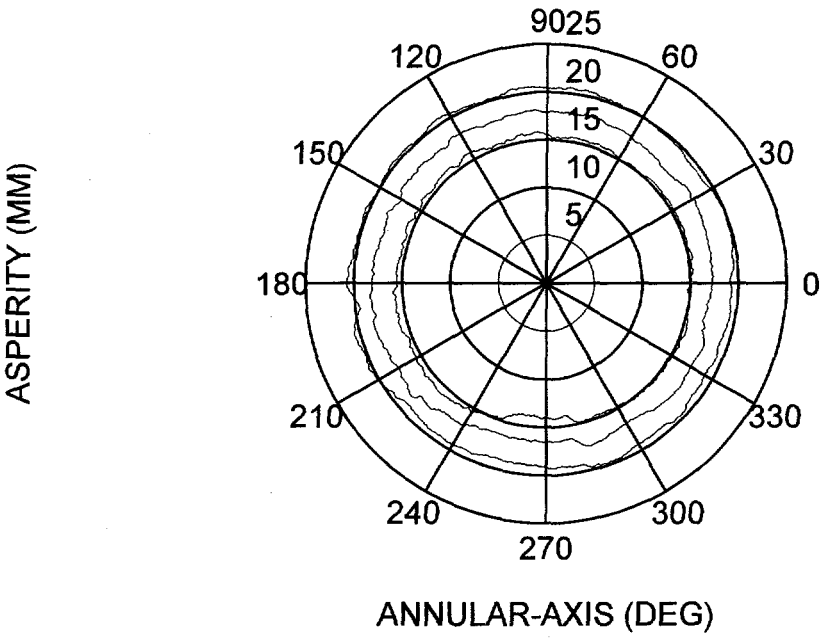

Annular topography of top part of fracture #5.

APPENDIX B

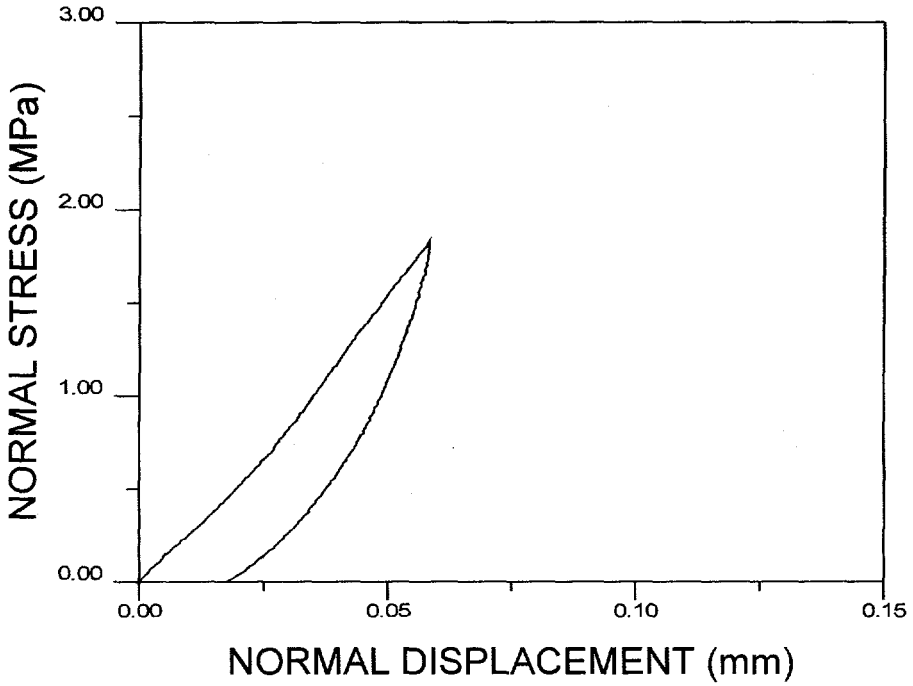

Normal compression test result for sample #1301.

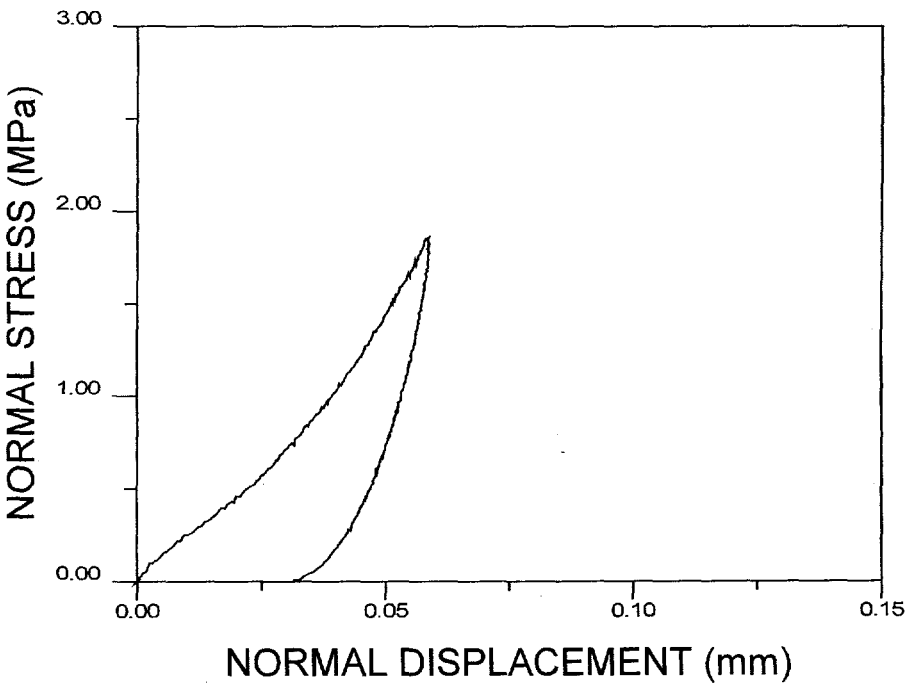

Normal compression test result for sample #1302.

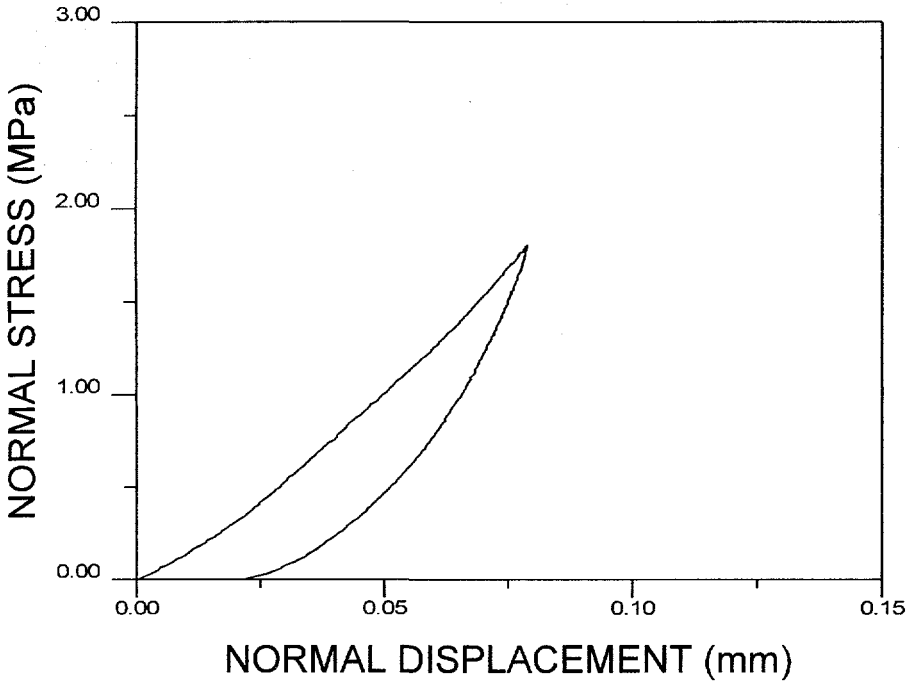

Normal compression test result for sample #1303.

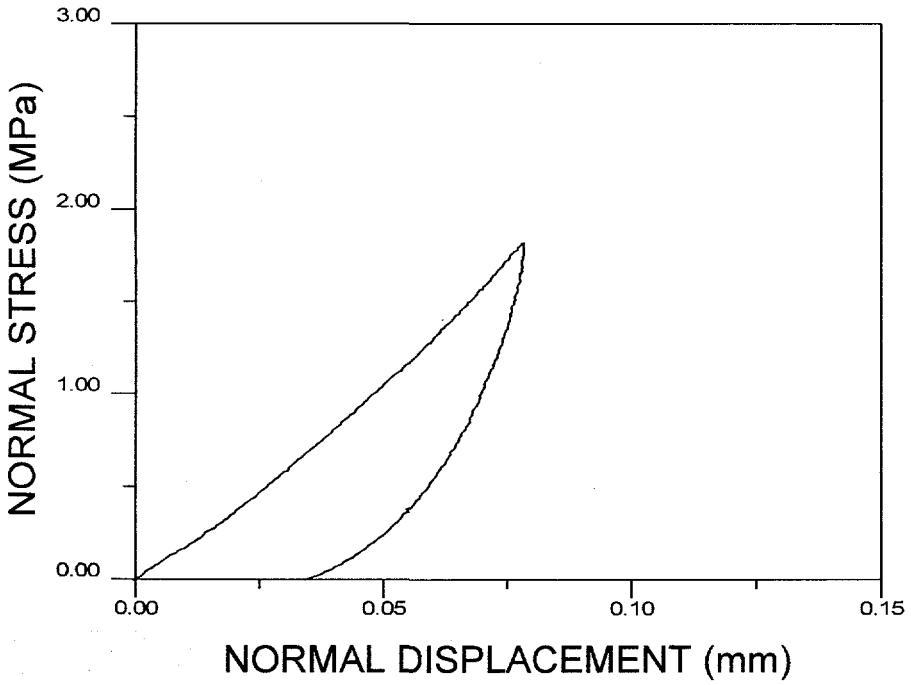

Normal compression test result for sample #1304.

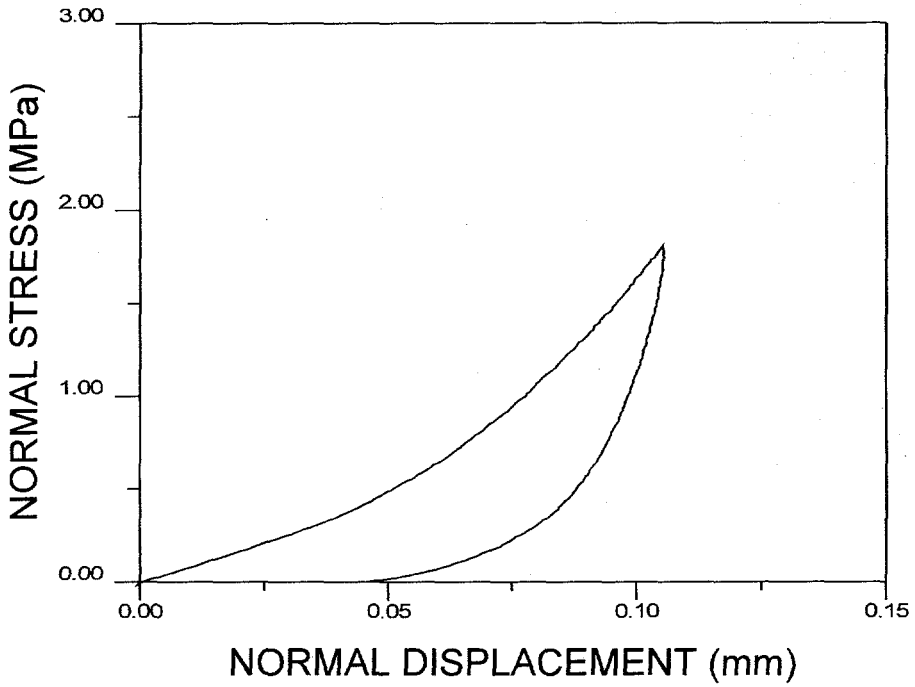

Normal compression test result for sample #1305.

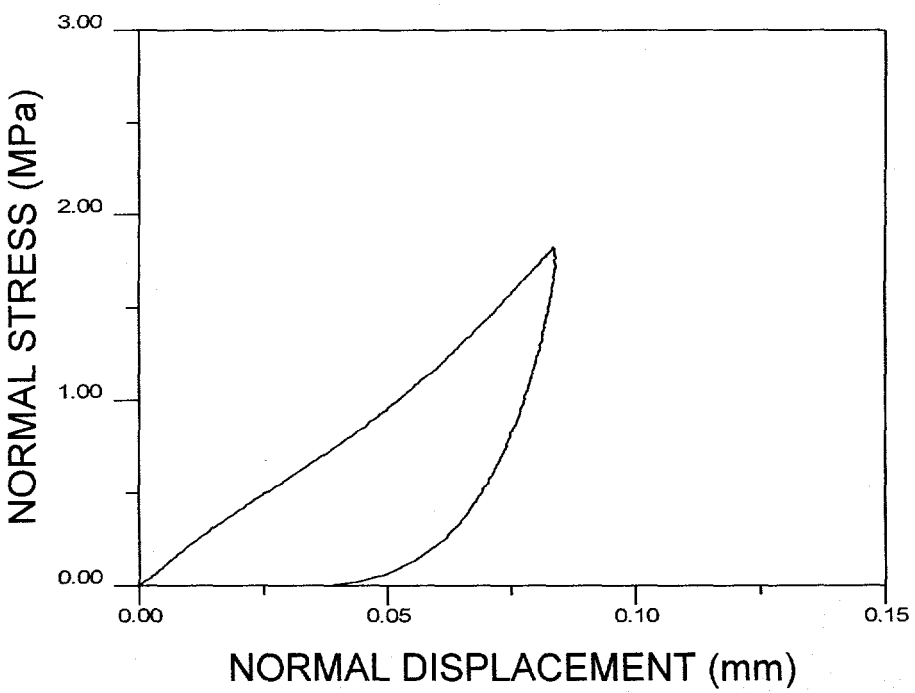

Normal compression test result for sample #1306.

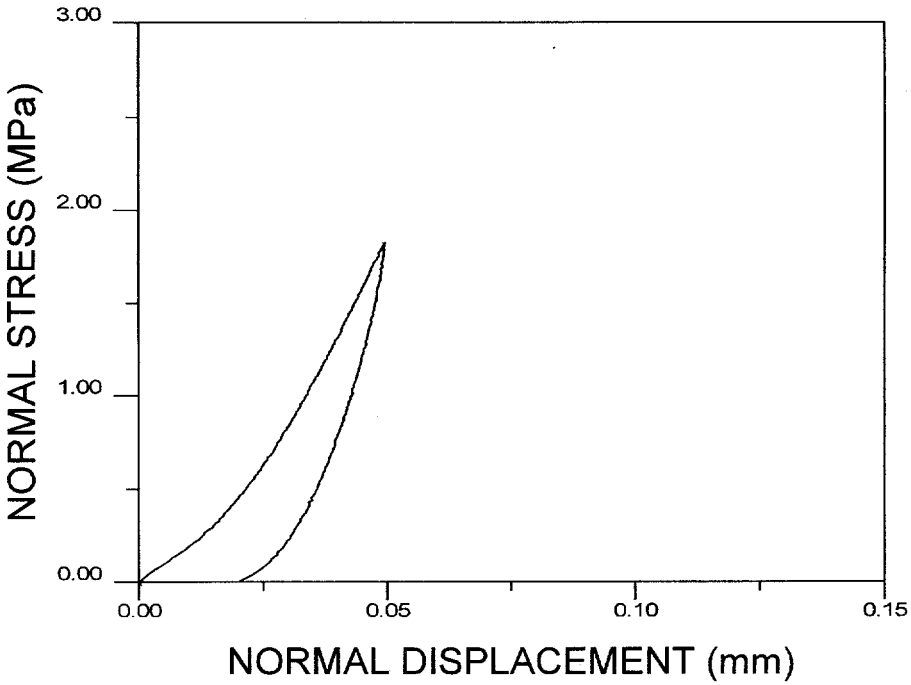

Normal compression test result for sample #1351.

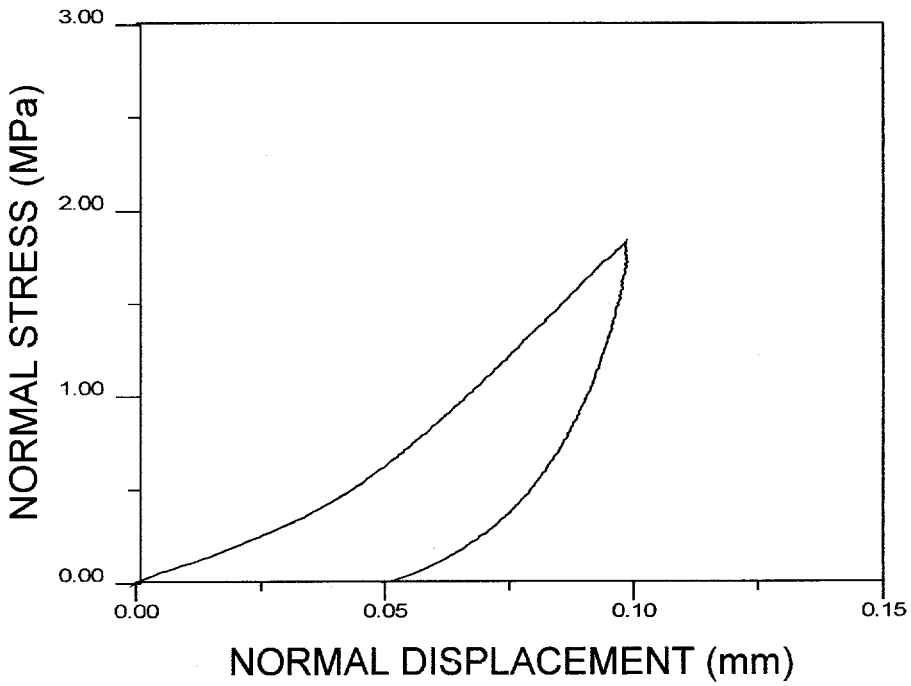

Normal compression test result for sample #1381.

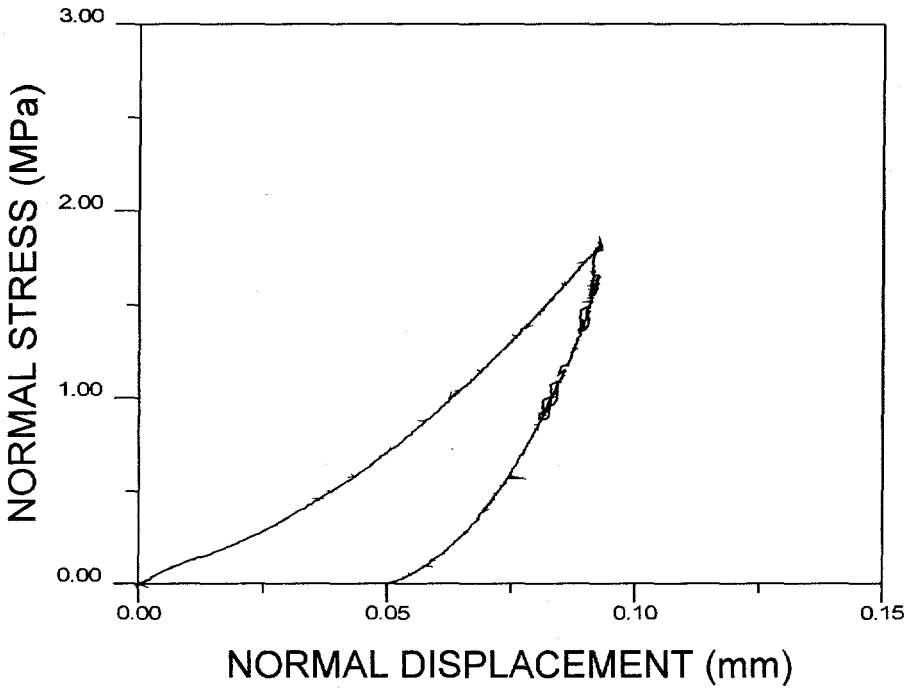

Normal compression test result for sample #1451.

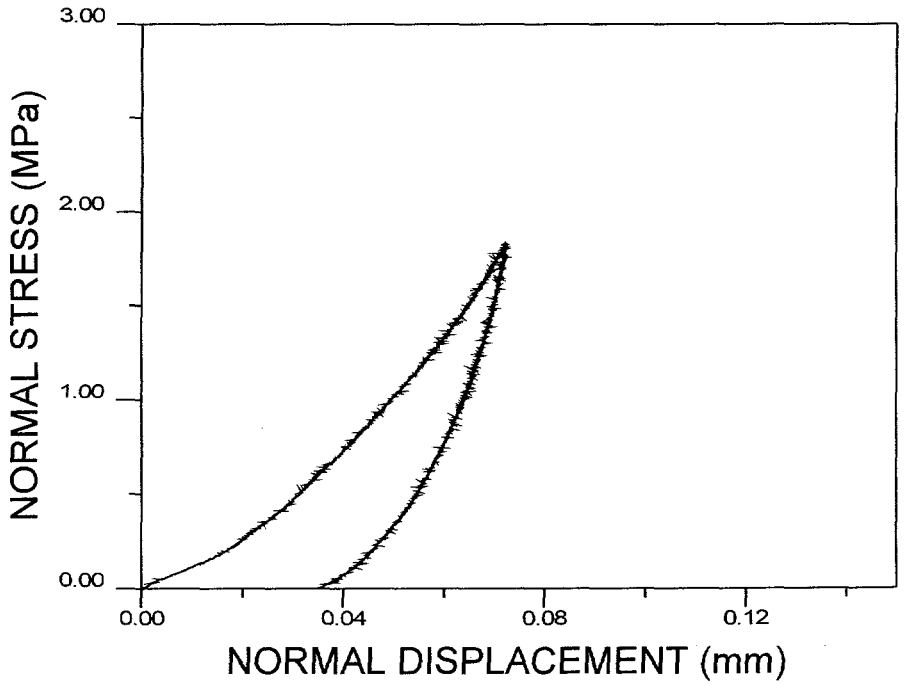

Normal compression test result for sample #2301.

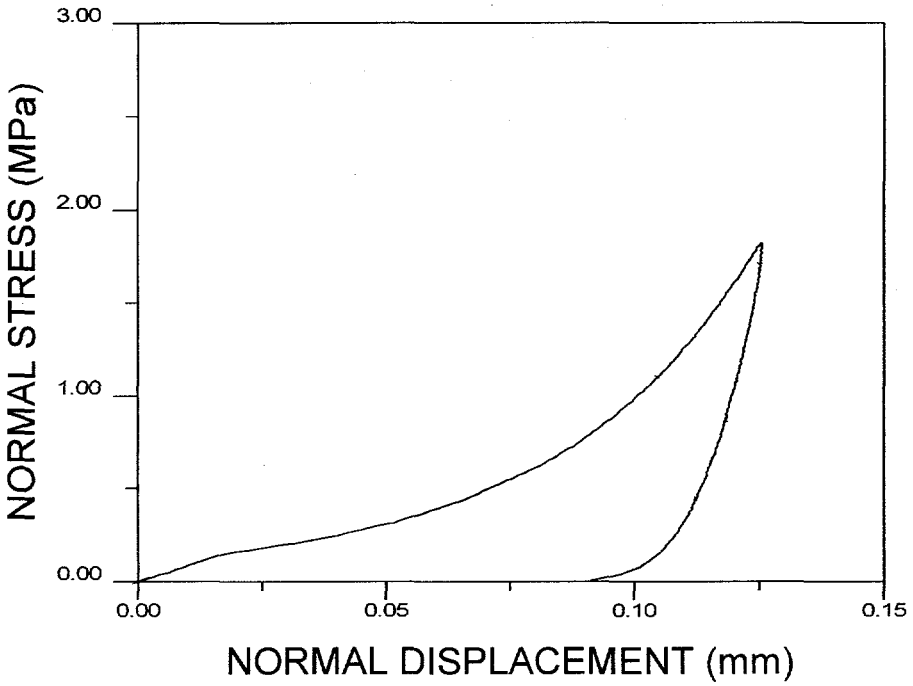

Normal compression test result for sample #4301.

APPENDIX C

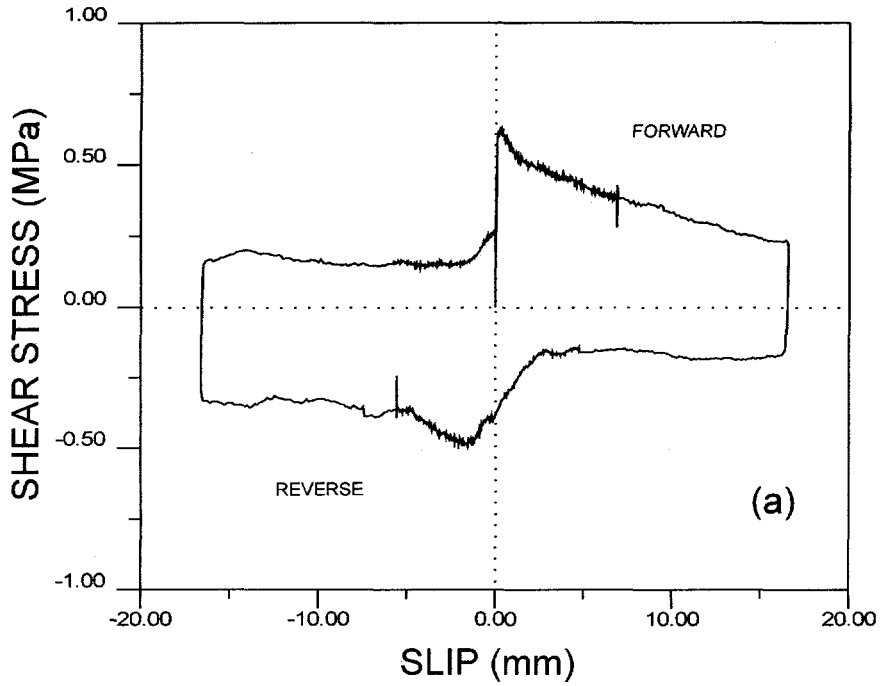

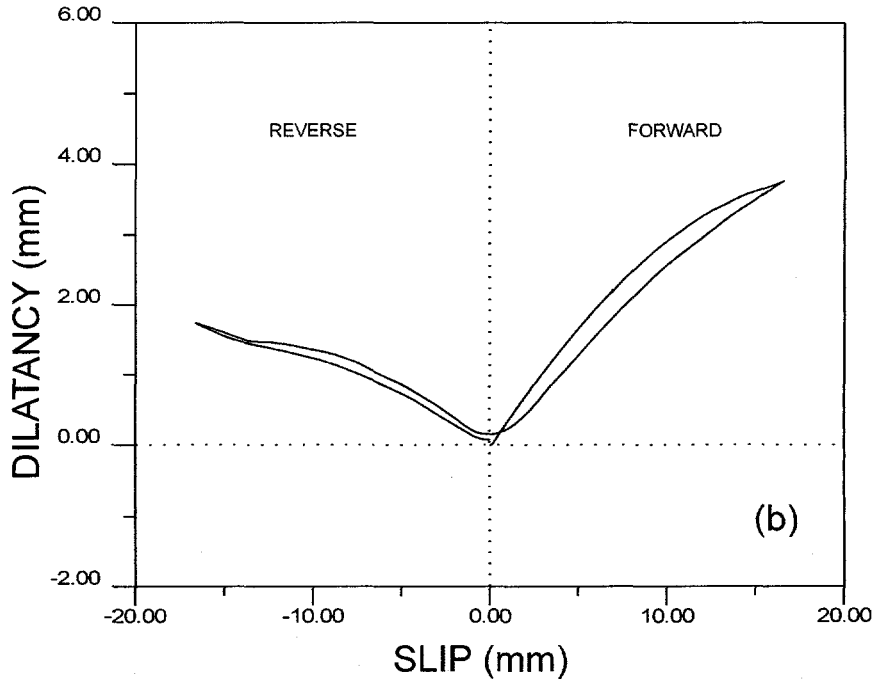

(a) Shear stress vs. slip, and (b) Dilatancy vs. slip response curves for sample #1301 tested under a constant normal stress of 0.4 MPa.

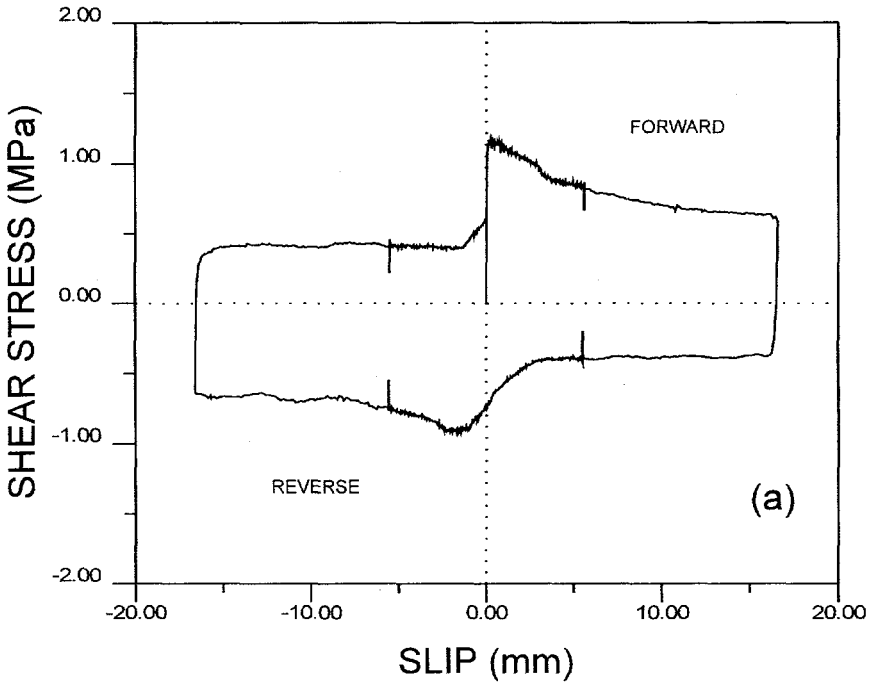

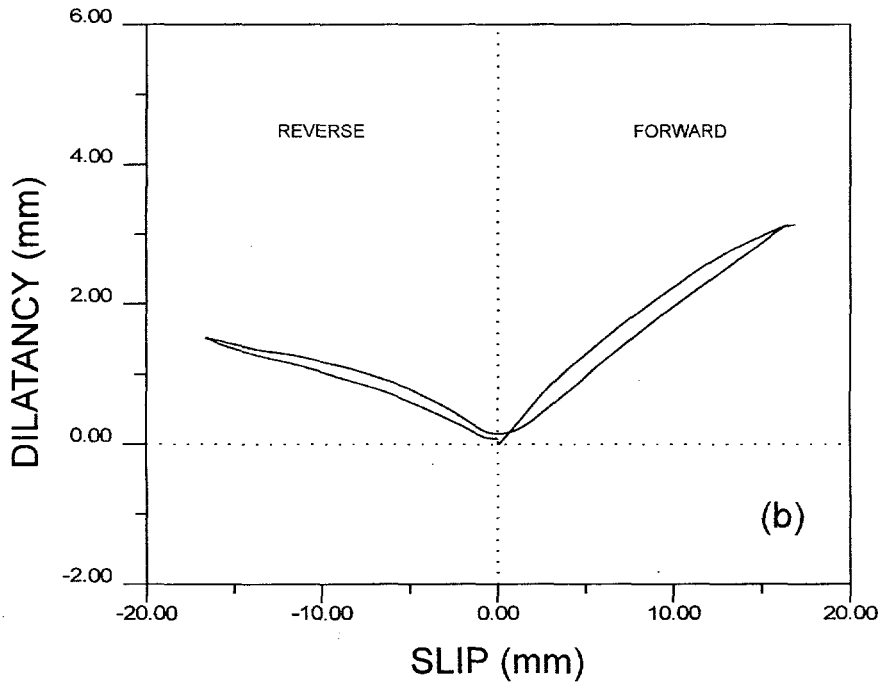

(a) Shear stress vs. slip, and (b) Dilatancy vs. slip response curves for sample #1302 tested under a constant normal stress of 0.8 MPa.

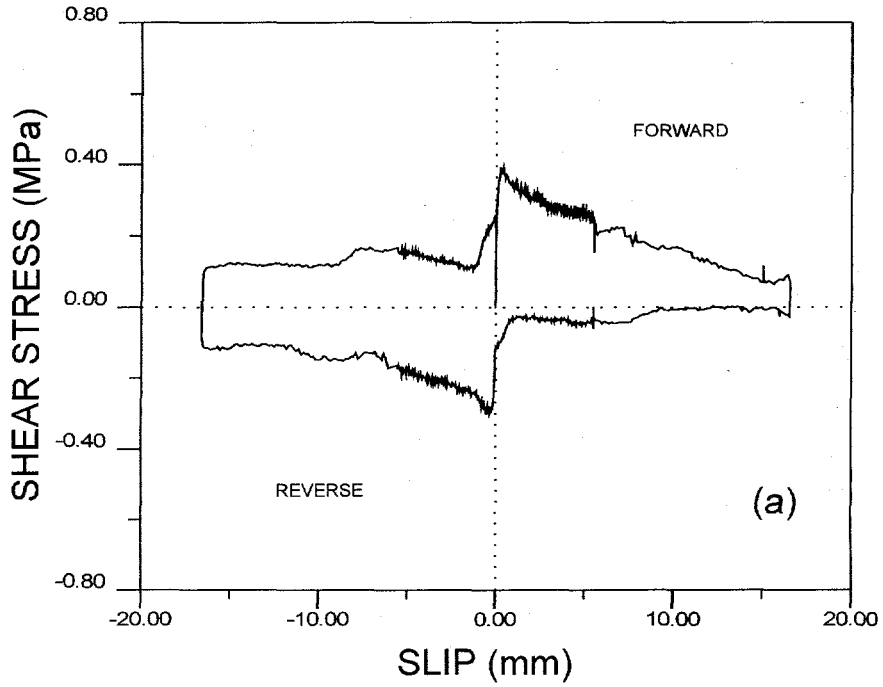

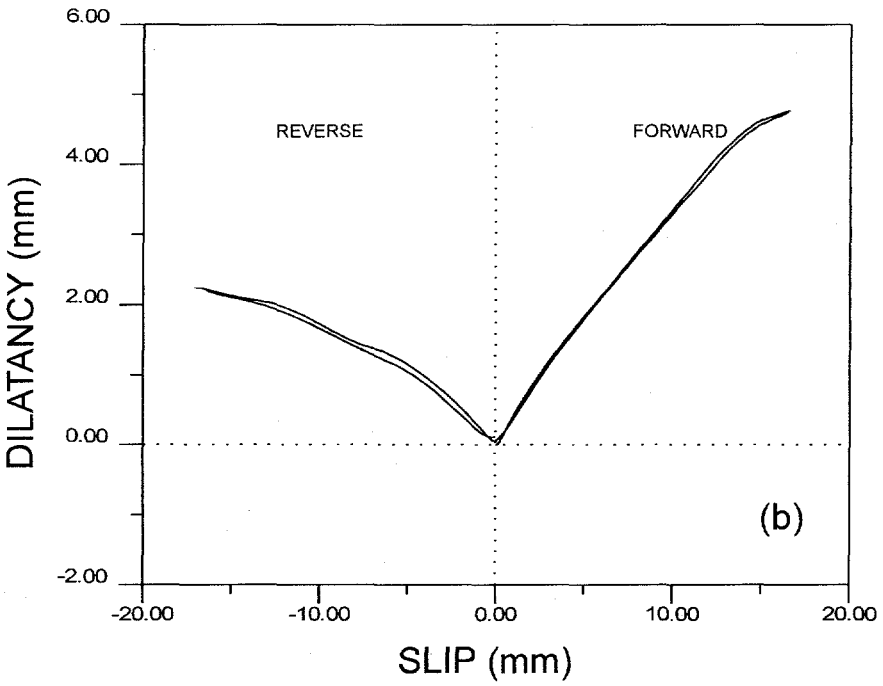

(a) Shear stress vs. slip, and (b) Dilatancy vs. slip response curves for sample #1303 tested under a constant normal stress of 0.2 MPa.

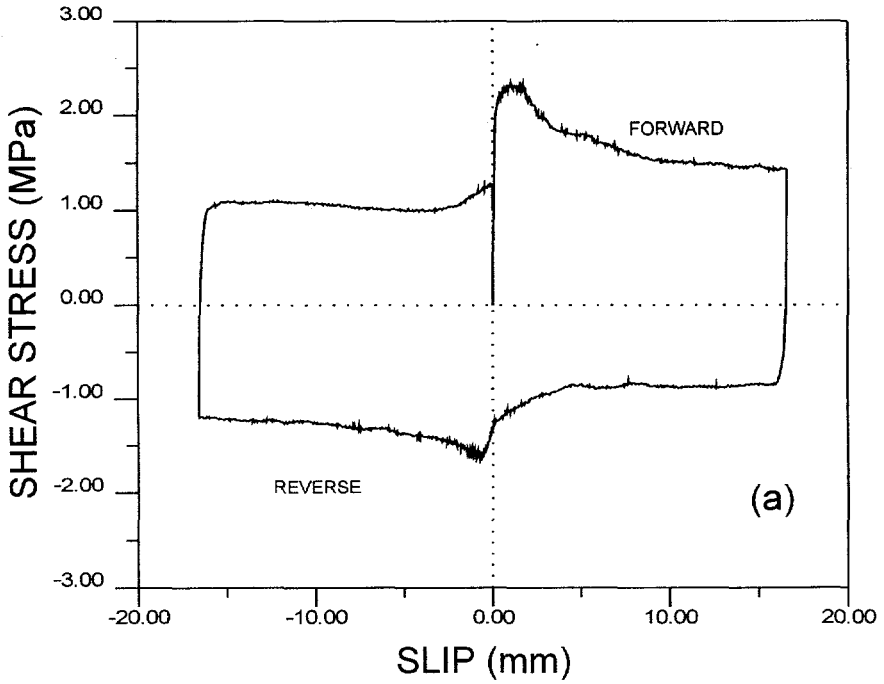

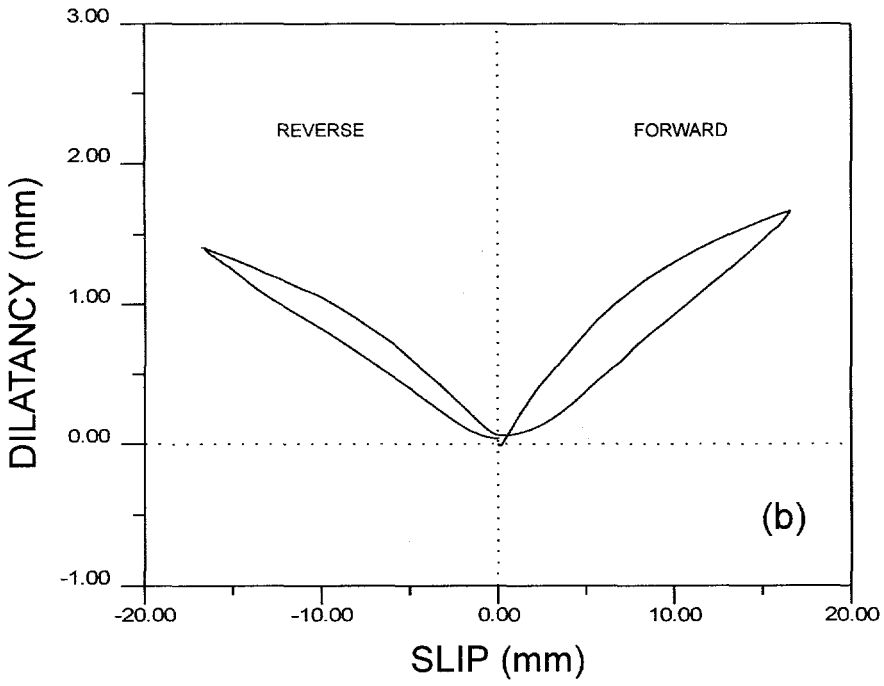

(a) Shear stress vs. slip, and (b) Dilatancy vs. slip response curves for sample #1304 tested under a constant normal stress of 1.6 MPa.

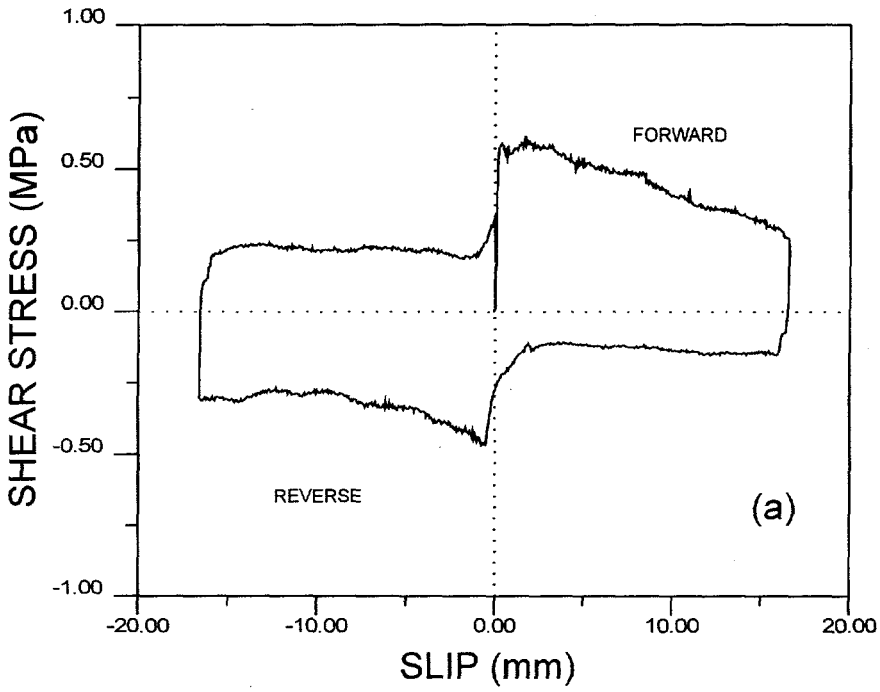

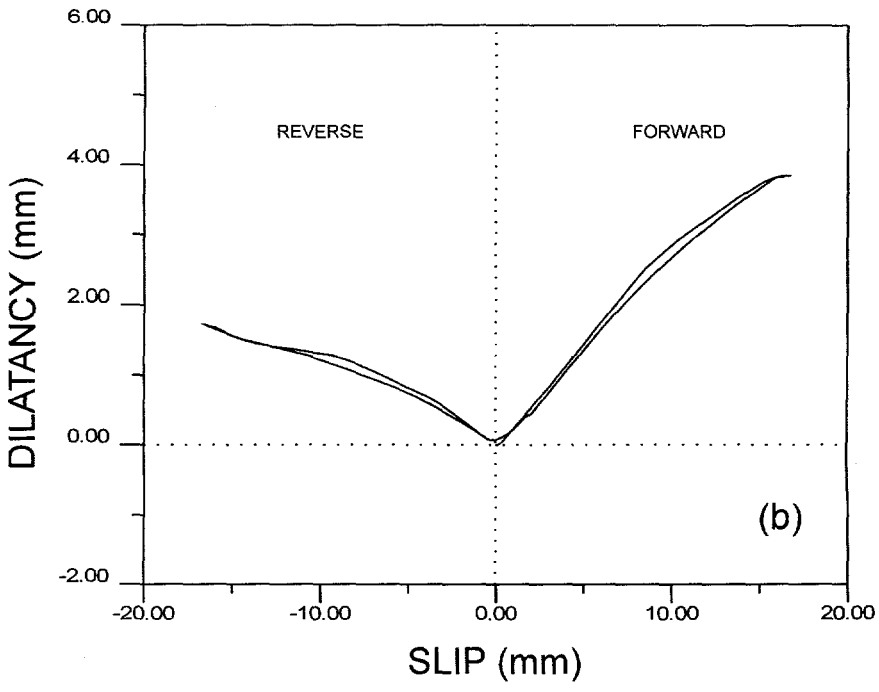

(a) Shear stress vs. slip, and (b) Dilatancy vs. slip response curves for sample #1305 tested under a constant normal stress of 0.4 MPa.

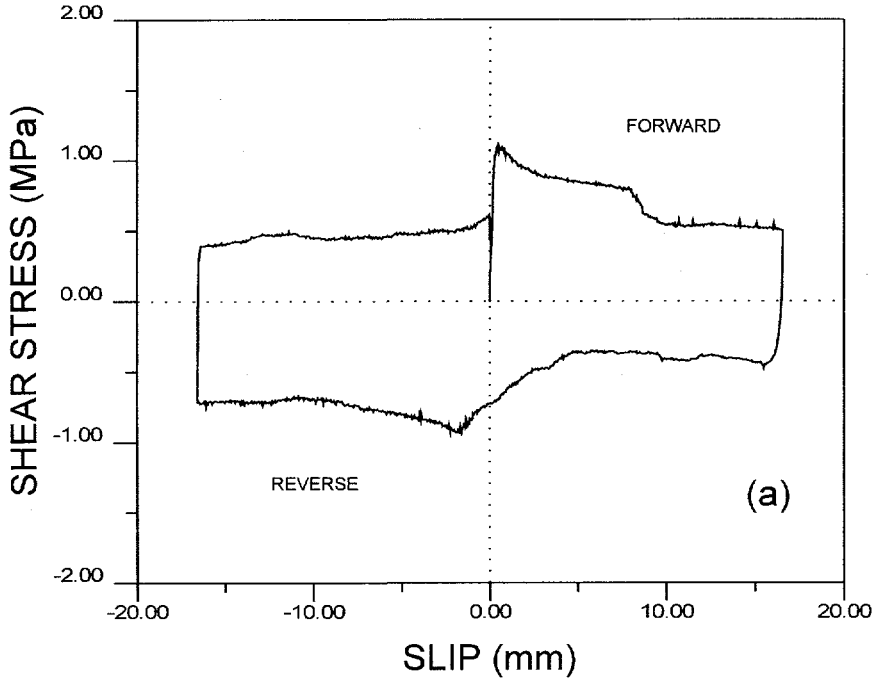

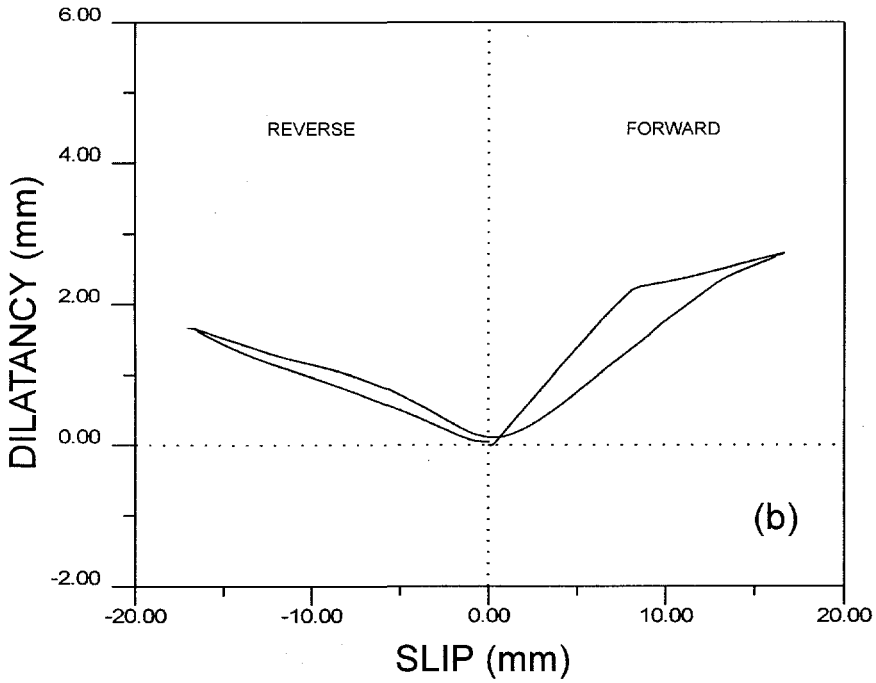

(a) Shear stress vs. slip, and (b) Dilatancy vs. slip response curves for sample #1306 tested under a constant normal stress of 0.8 MPa.

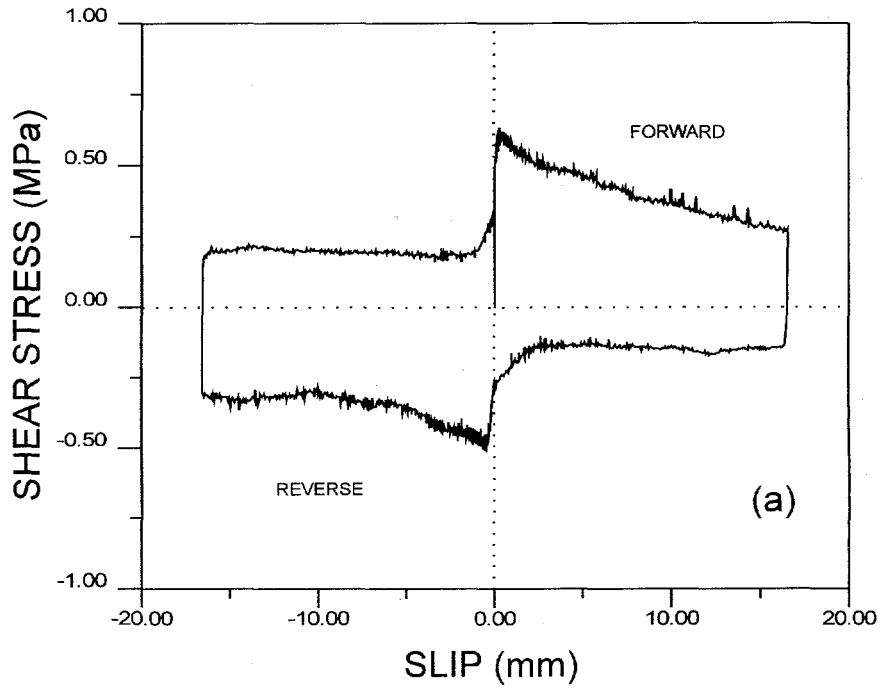

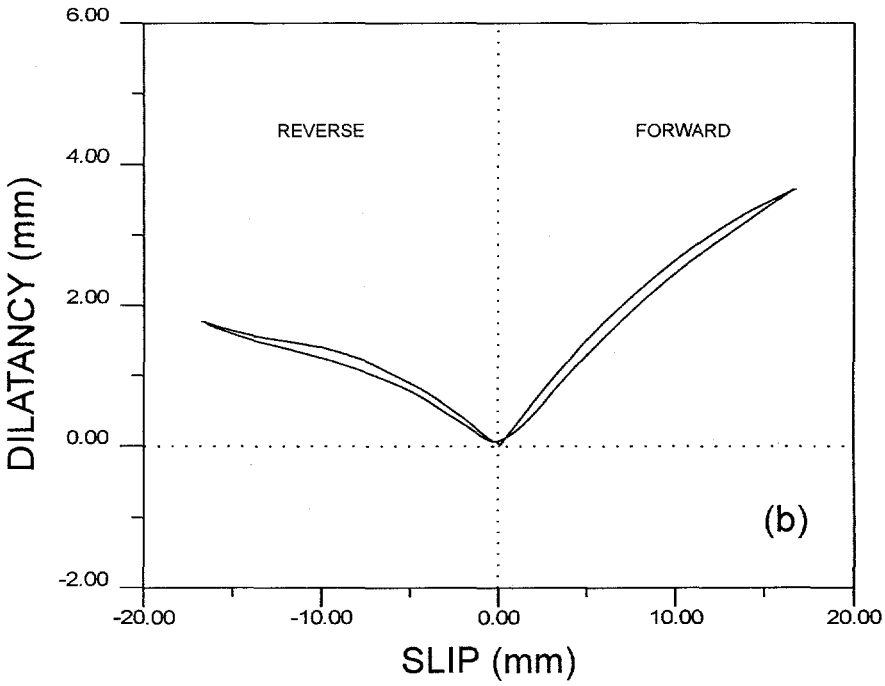

(a) Shear stress vs. slip, and (b) Dilatancy vs. slip response curves for sample #1351 tested under a constant normal stress of 0.4 MPa.

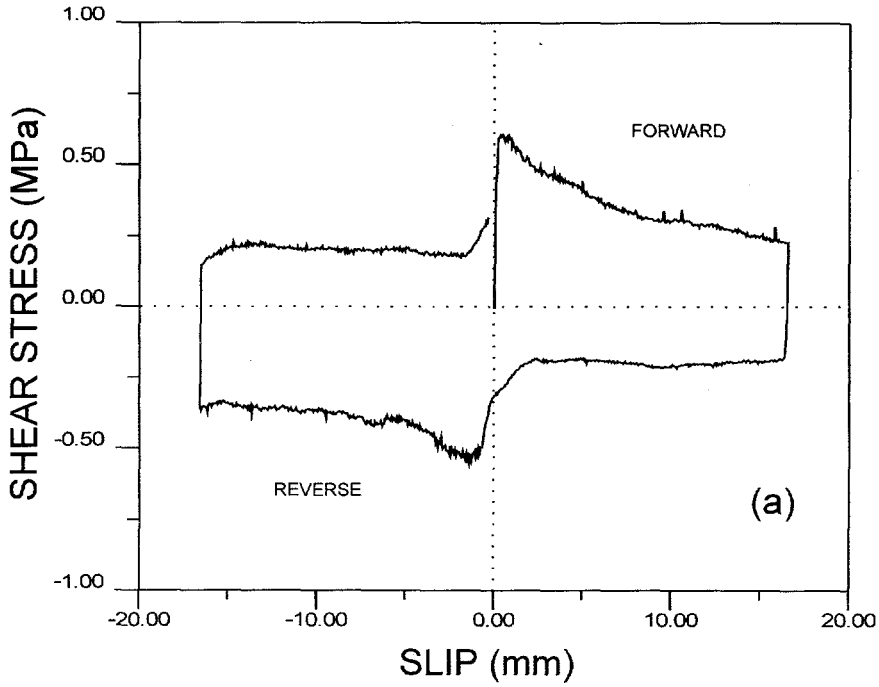

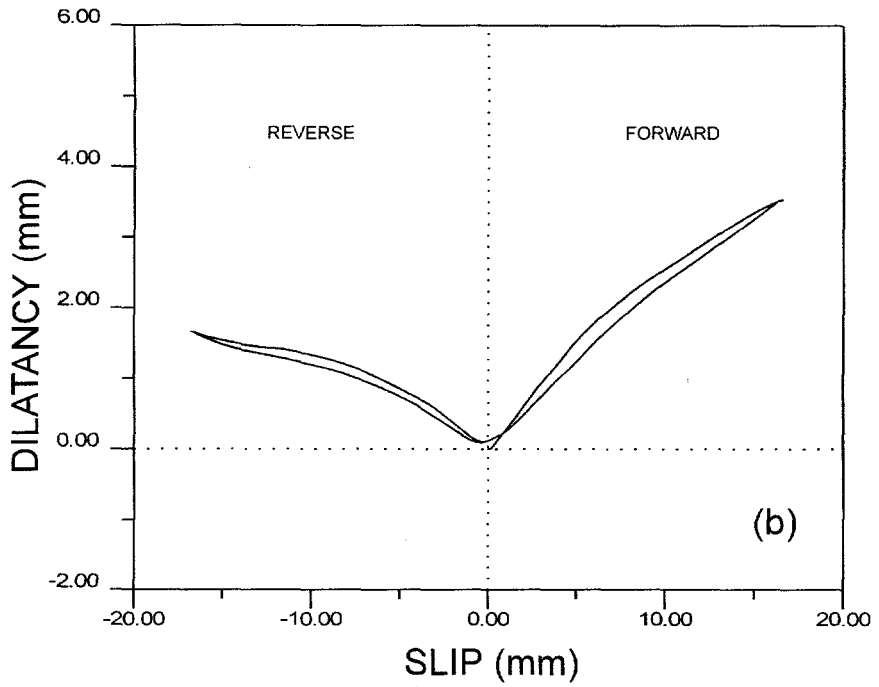

(a) Shear stress vs. slip, and (b) Dilatancy vs. slip response curves for sample #1381 tested under a constant normal stress of 0.4 MPa.

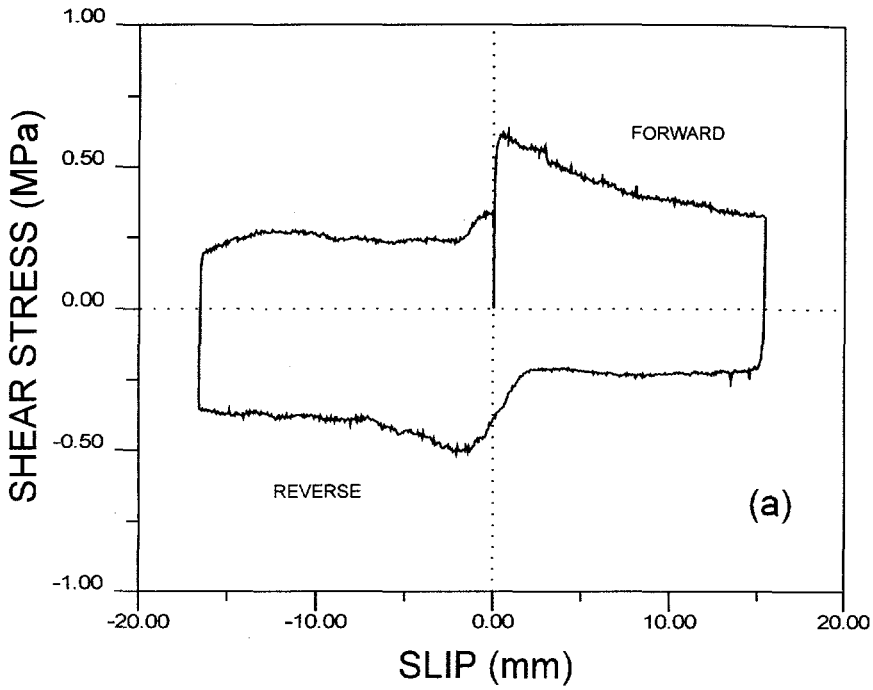

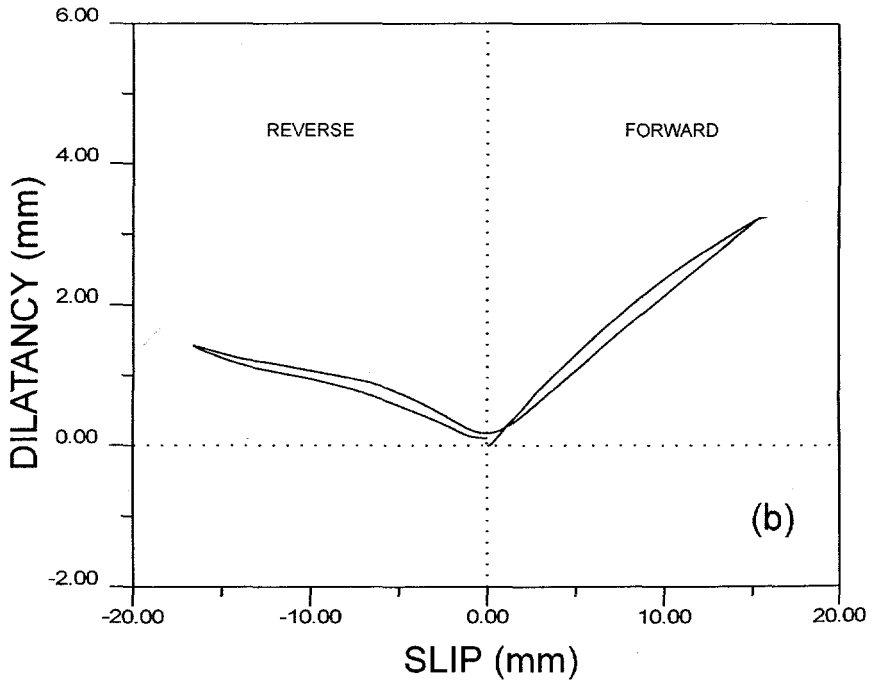

(a) Shear stress vs. slip, and (b) Dilatancy vs. slip response curves for sample #1451 tested under a constant normal stress of 0.4 MPa.

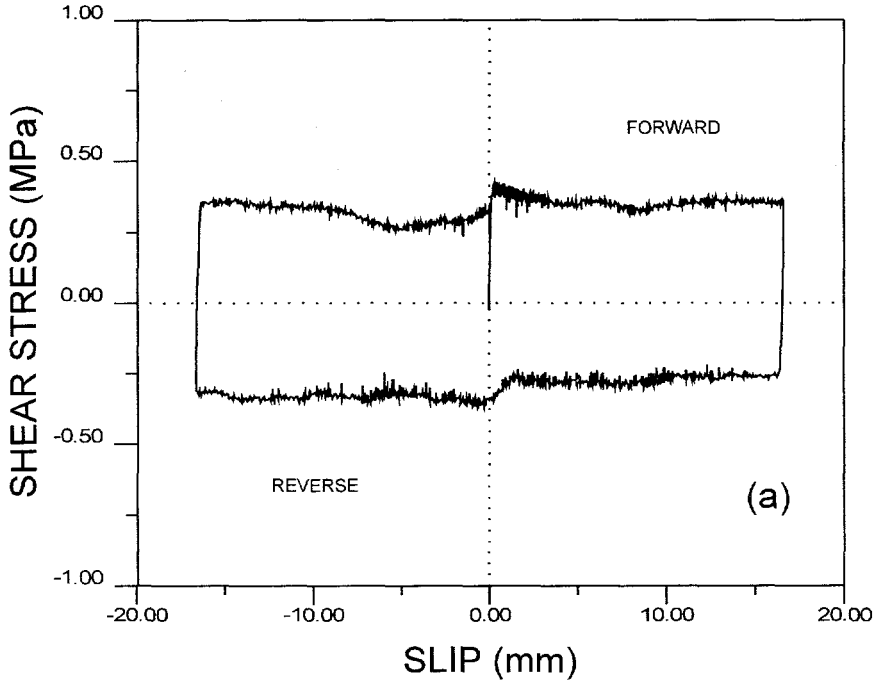

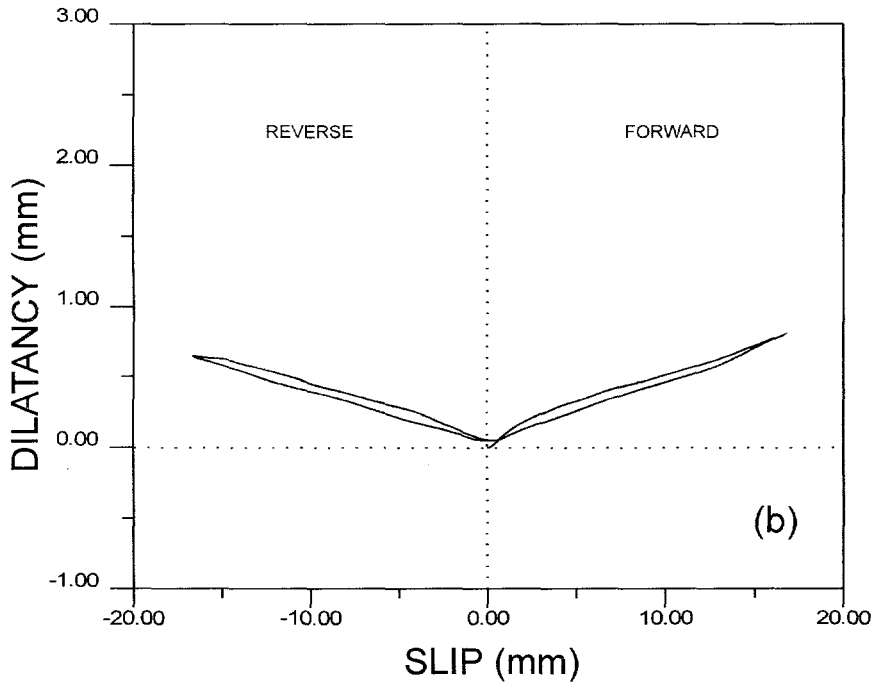

(a) Shear stress vs. slip, and (b) Dilatancy vs. slip response curves for sample #2301 tested under a constant normal stress of 0.4 MPa.

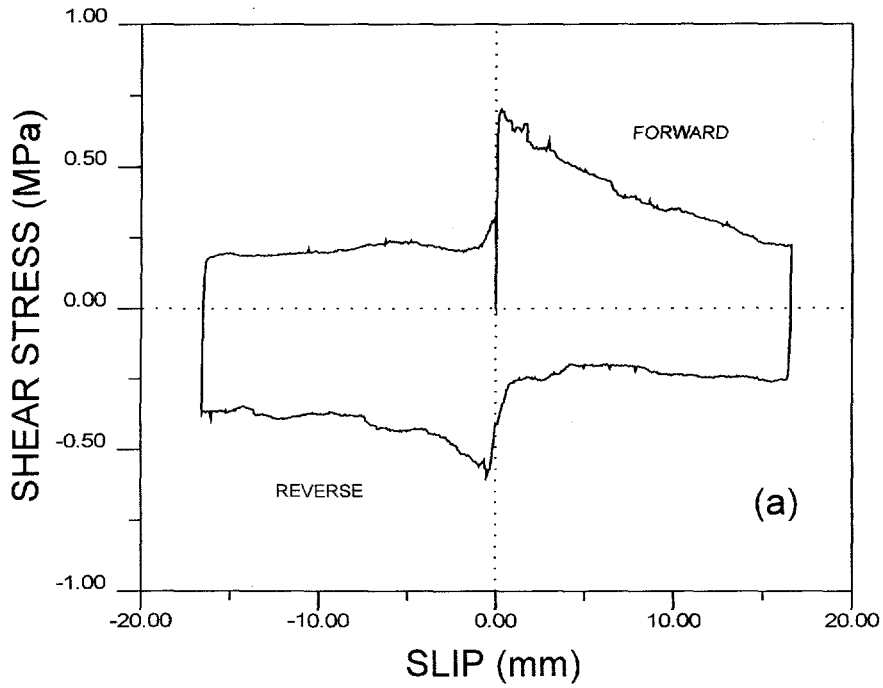

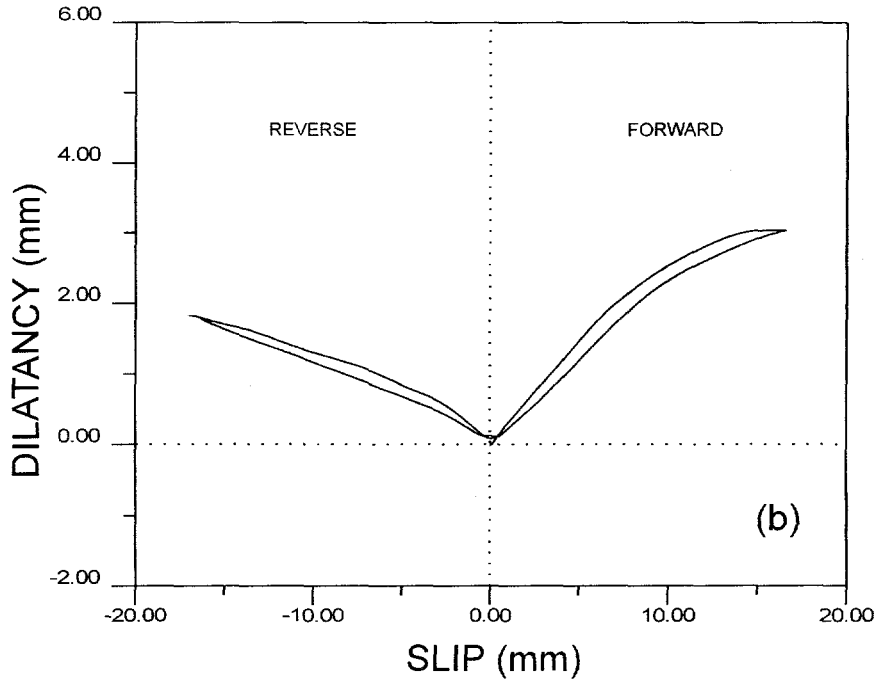

(a) Shear stress vs. slip, and (b) Dilatancy vs. slip response curves for sample #4301 tested under a constant normal stress of 0.4 MPa.

APPENDIX D

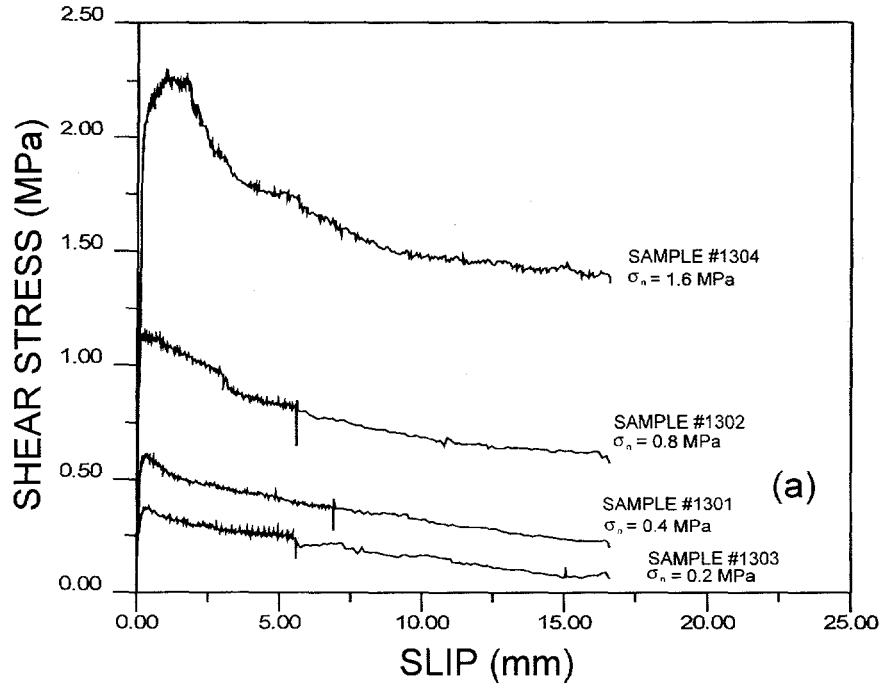

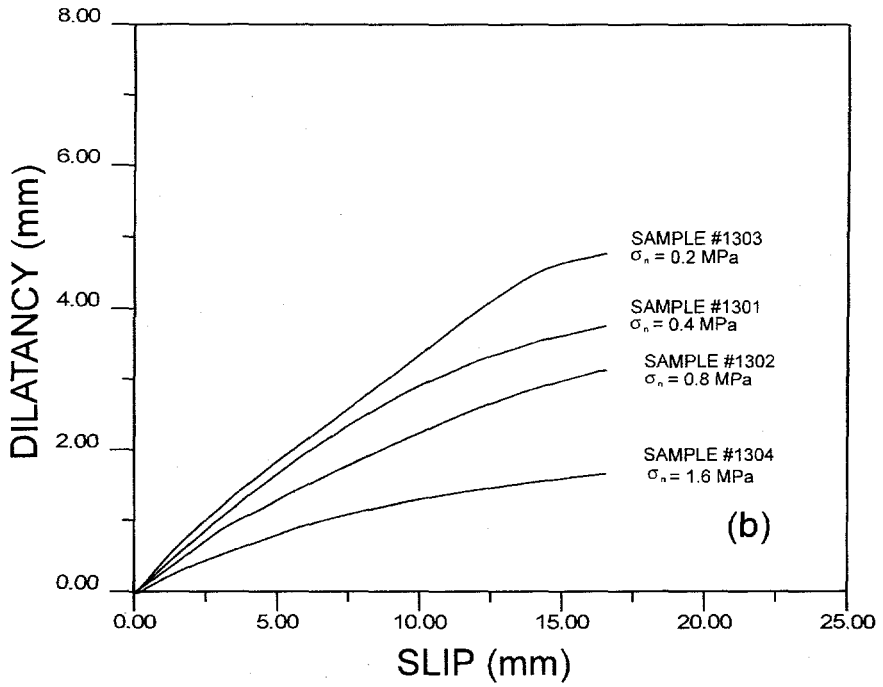

(a) Shear stress vs. slip, and (b) Dilatancy vs. slip response curves for four replicas of fracture #1 with same 30% water-to-gypsum cement ratio and tested under different levels of applied normal stress. Forward shear motion. Samples #1301, 1302, 1303, and 1304.

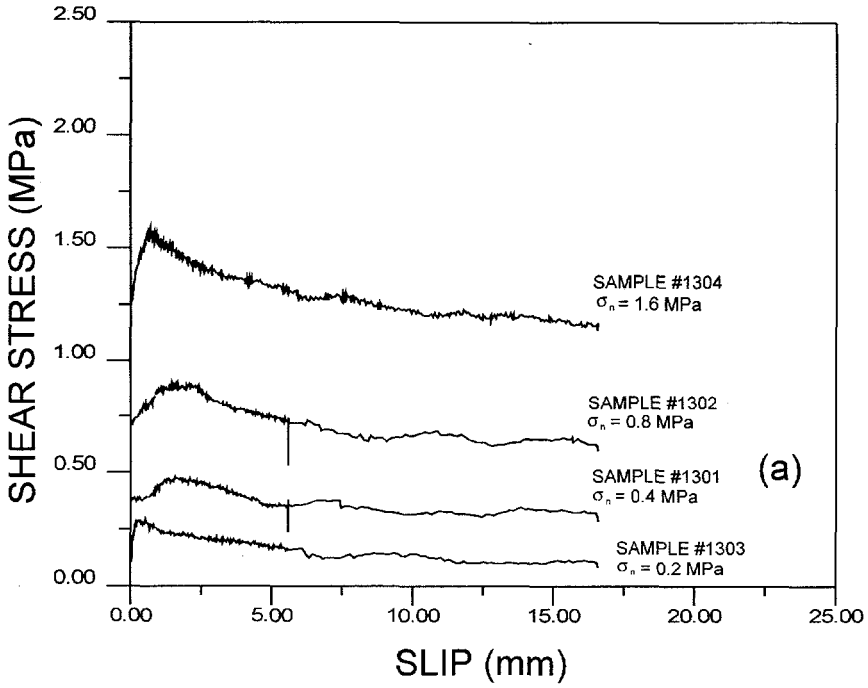

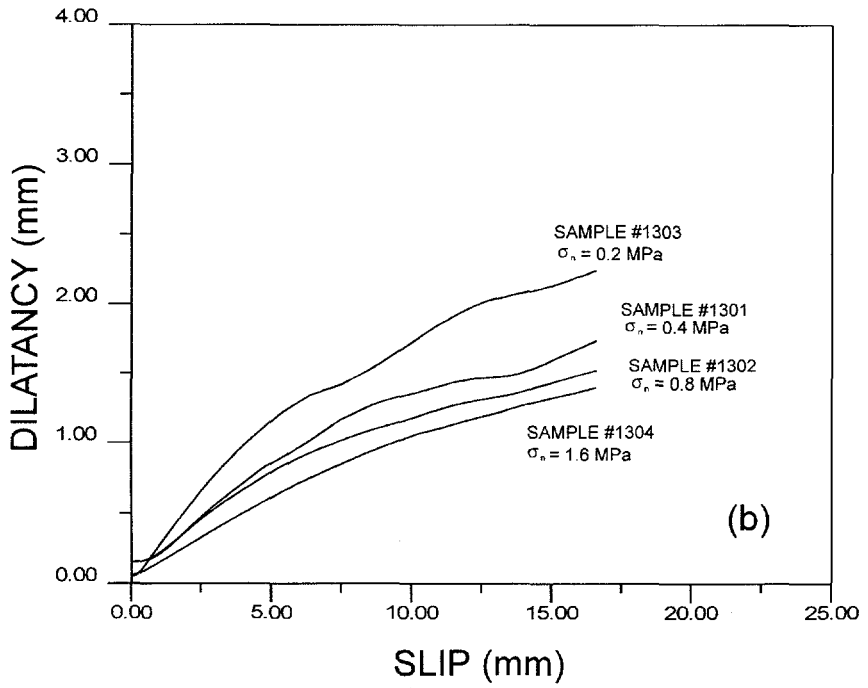

(a) Shear stress vs. slip, and (b) Dilatancy vs. slip response curves for four replicas of fracture #1 with same 30% water-to-gypsum cement ratio and tested under different levels of applied normal stress. Reverse shear motion. Samples #1301, 1302, 1303, and 1304.

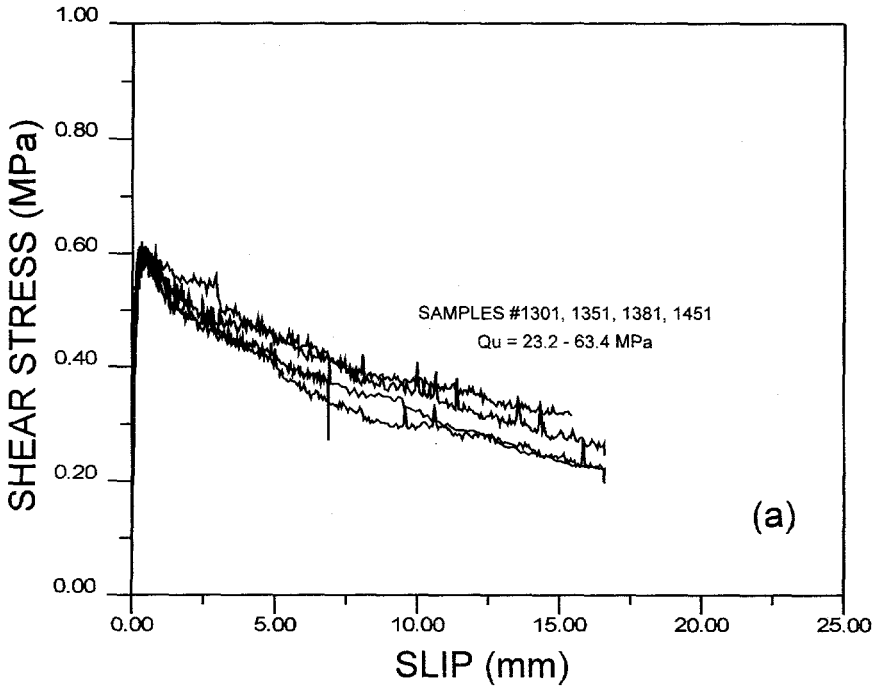

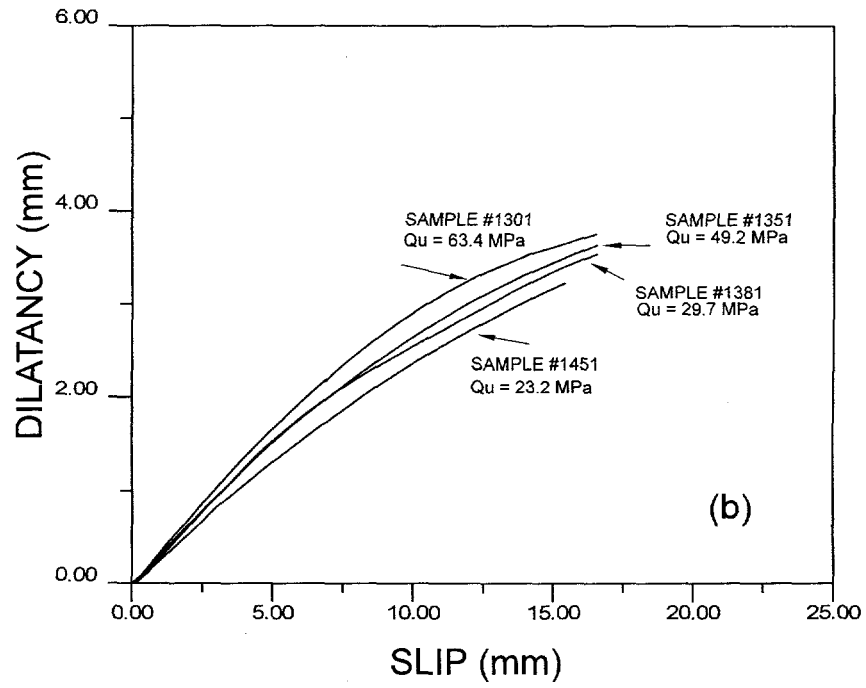

(a) Shear stress vs. slip, and (b) Dilatancy vs. slip response curves for four replicas of fracture #1 with different water-to-gypsum cement ratios of 30, 35, 38, and 45%. All sample tested under a constant normal stress of 0.4 MPa. Forward shear motion. Sample #1301, 1351, 1381, and 1451.

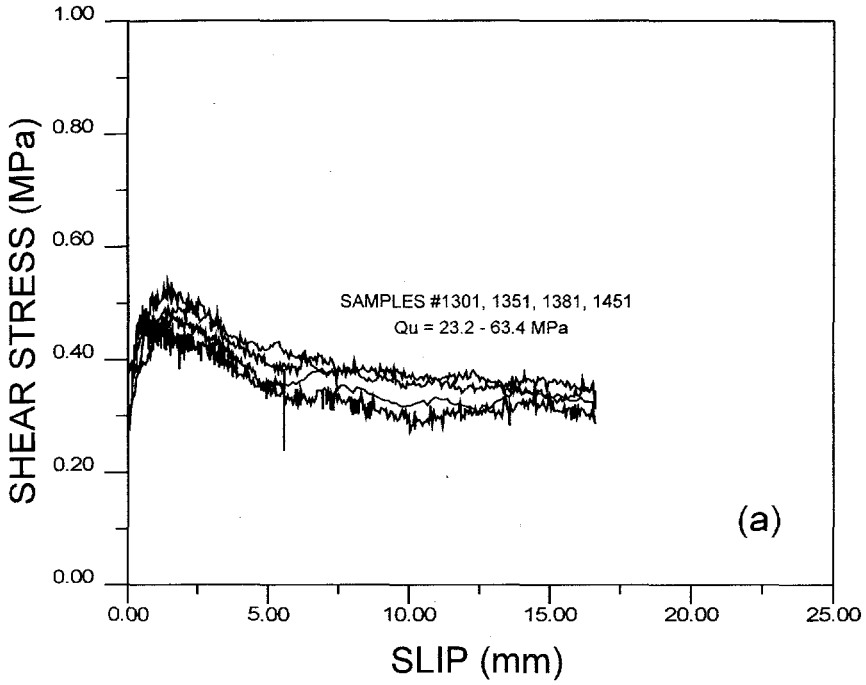

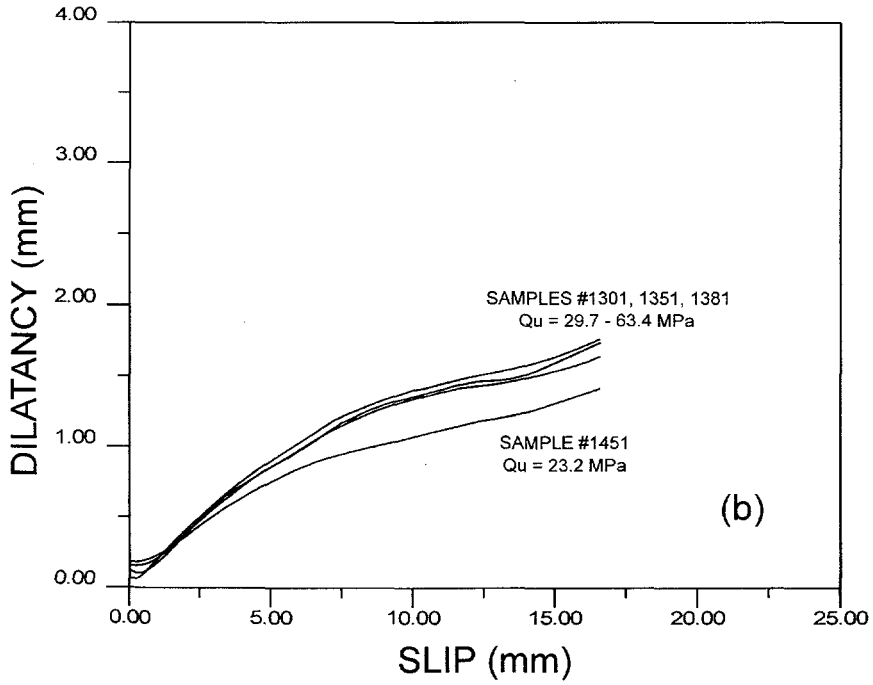

(a) Shear stress vs. slip, and (b) Dilatancy vs. slip response curves for four replicas of fracture #1 with different water-to-gypsum cement ratios of 30, 35, 38, and 45%. All sample tested under a constant normal stress of 0.4 MPa. Reverse shear motion. Sample #1301, 1351, 1381, and 1451.

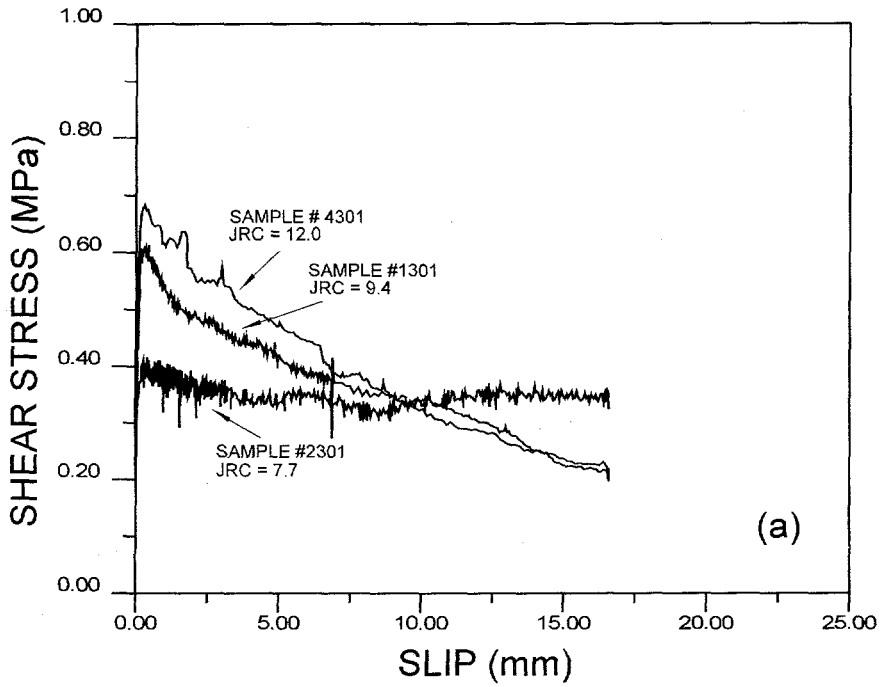

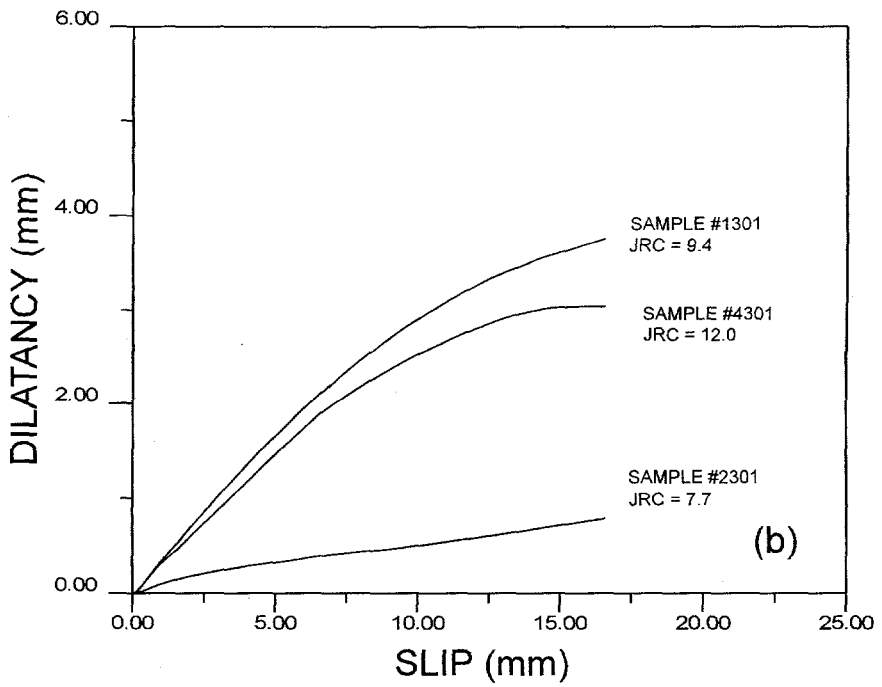

(a) Shear stress vs. slip, and (b) Dilatancy vs. slip response curves for forward shear motion for three fractures having the same 30% water-to-gypsum cement ratio and with initial JRC values of 7.7, 9.4, and 12.0. All fractures were sheared under the same constant normal stress of 0.4 MPa.

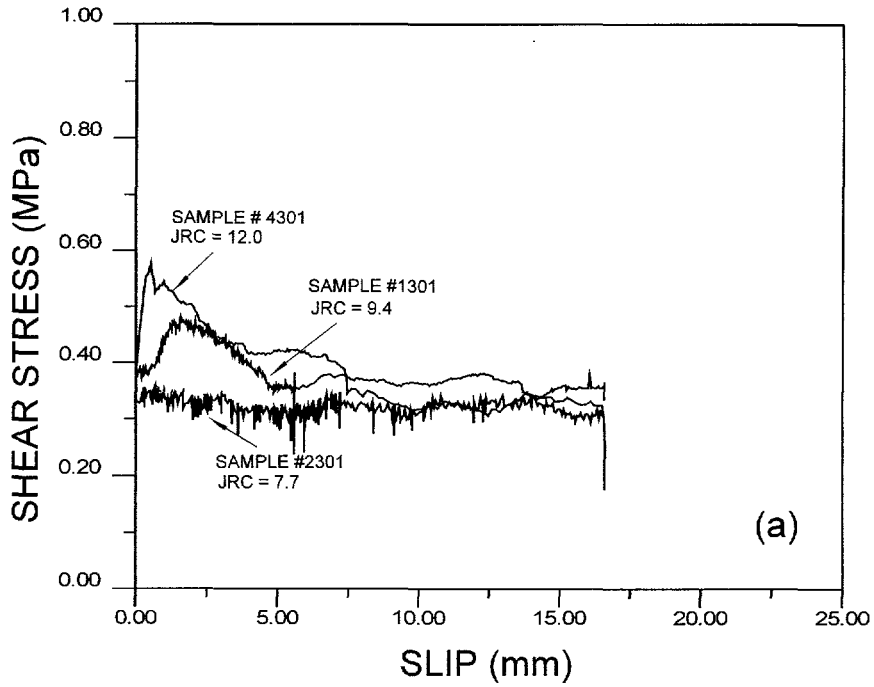

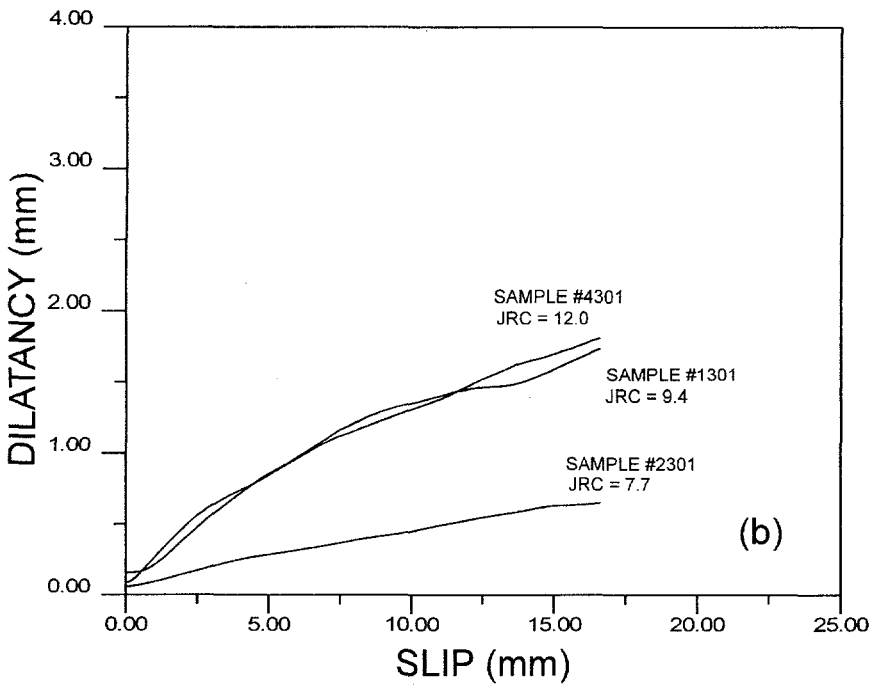

(a) Shear stress vs. slip, and (b) Dilatancy vs. slip response curves for reverse shear motion for three fractures having the same 30% water-to-gypsum cement ratio and with initial JRC values of 7.7, 9.4, and 12.0. All fractures were sheared under the same constant normal stress of 0.4 MPa.

APPENDIX E

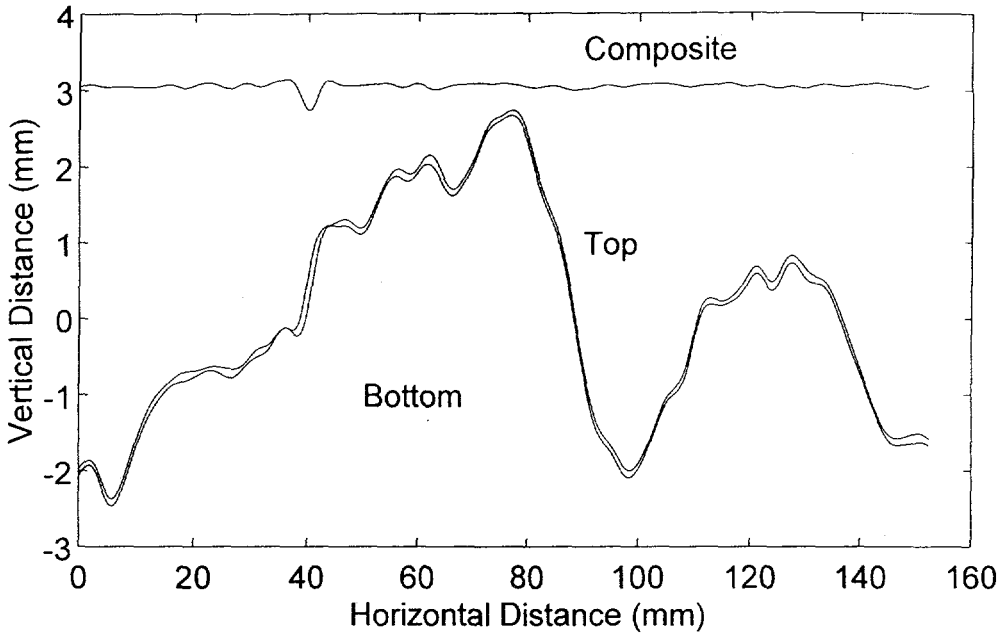

(a)

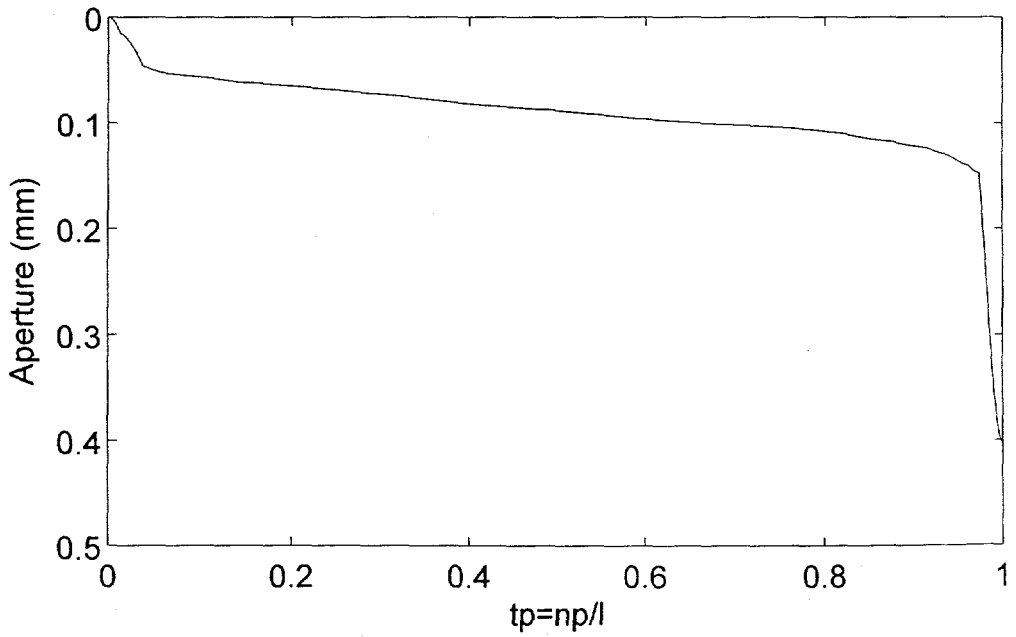

(b)

(a) Bottom, top, and composite topography, and (b) Bearing area curve for fracture #1 in a mated position.

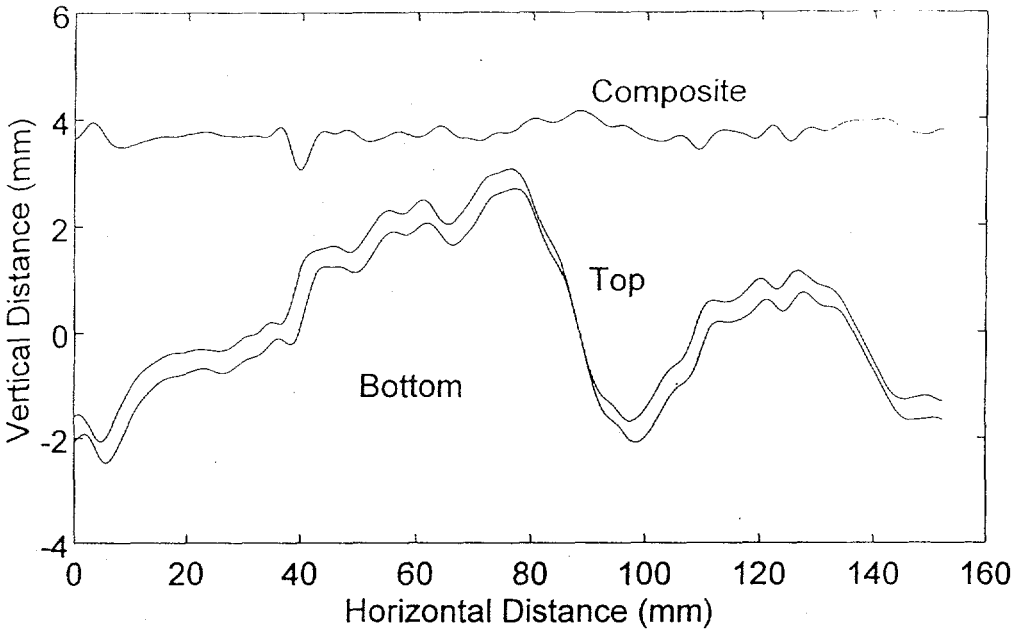

(a)

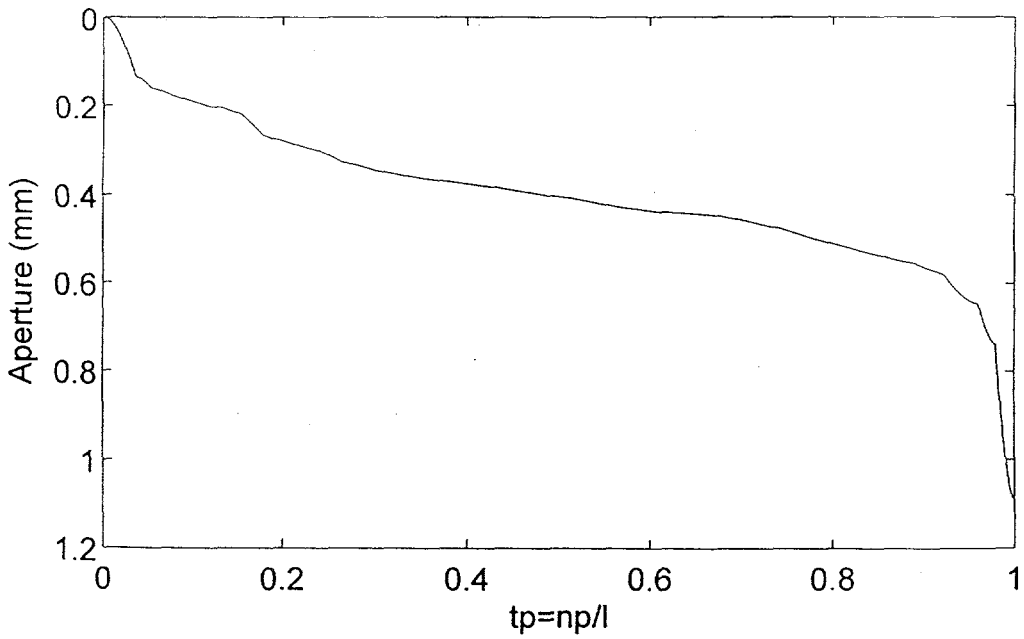

(b)

(a) Bottom, top, and composite topography, and (b) Bearing area curve for fracture #1 after 1 mm of slip.

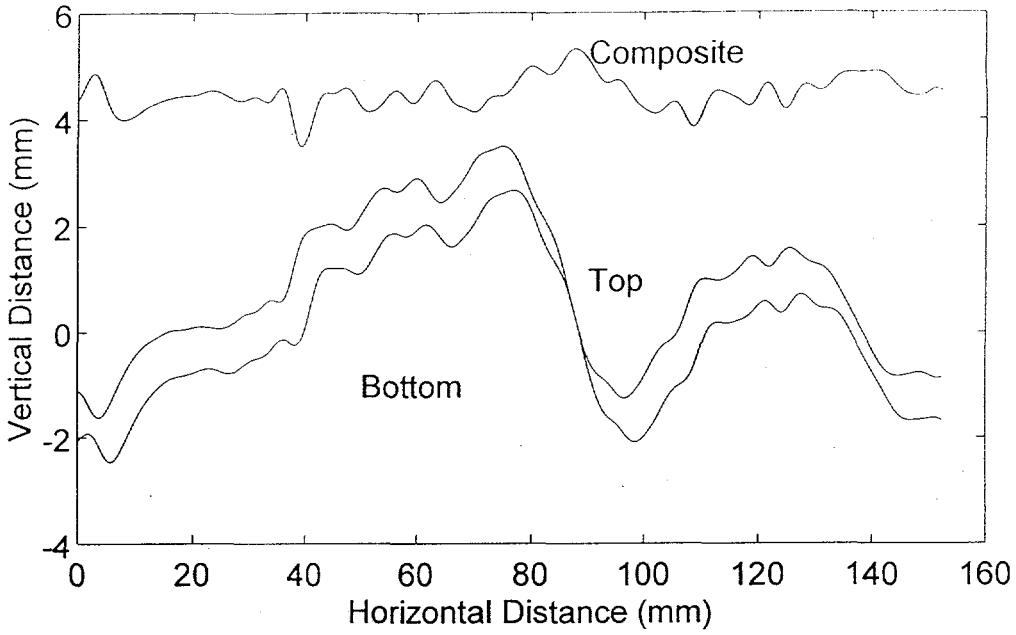

(a)

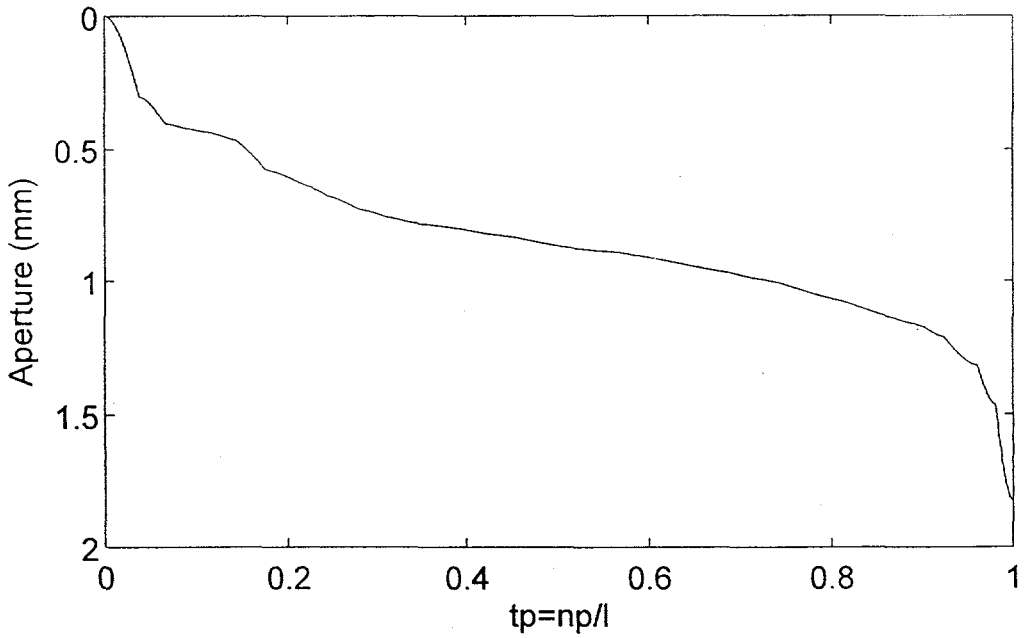

(b)

(a) Bottom, top, and composite topography, and (b) Bearing area curve for fracture #1 after 2 mm of slip.

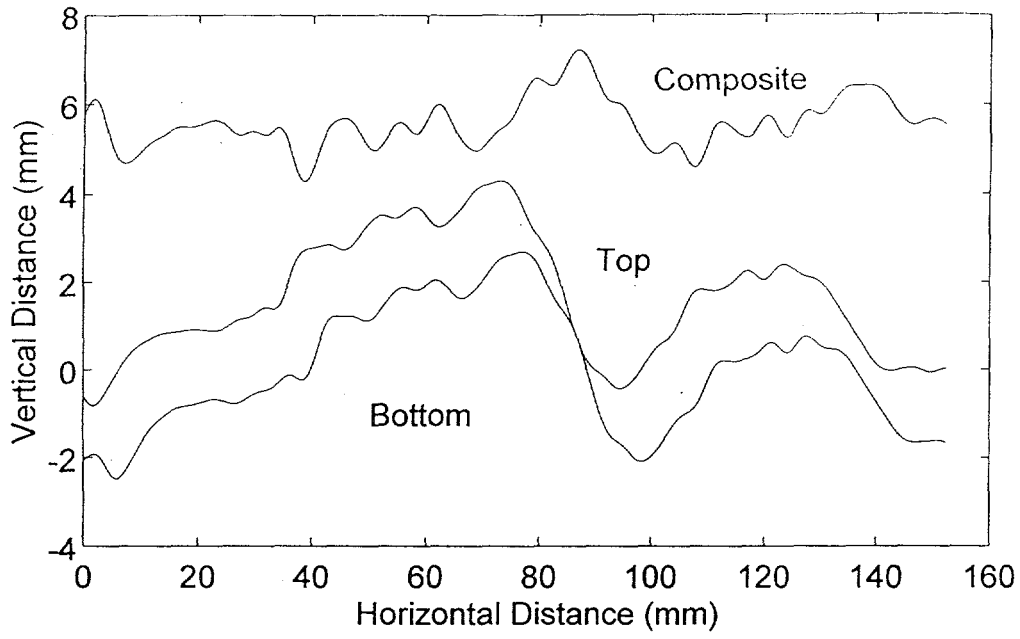

(a)

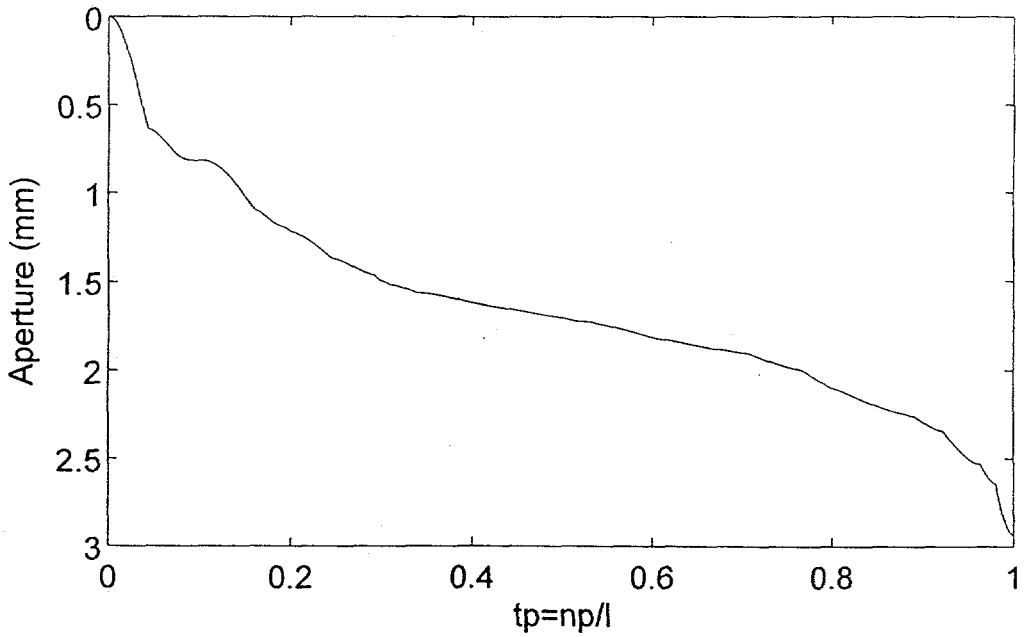

(b)

(a) Bottom, top, and composite topography, and (b) Bearing area curve for fracture #1 after 4 mm of slip.

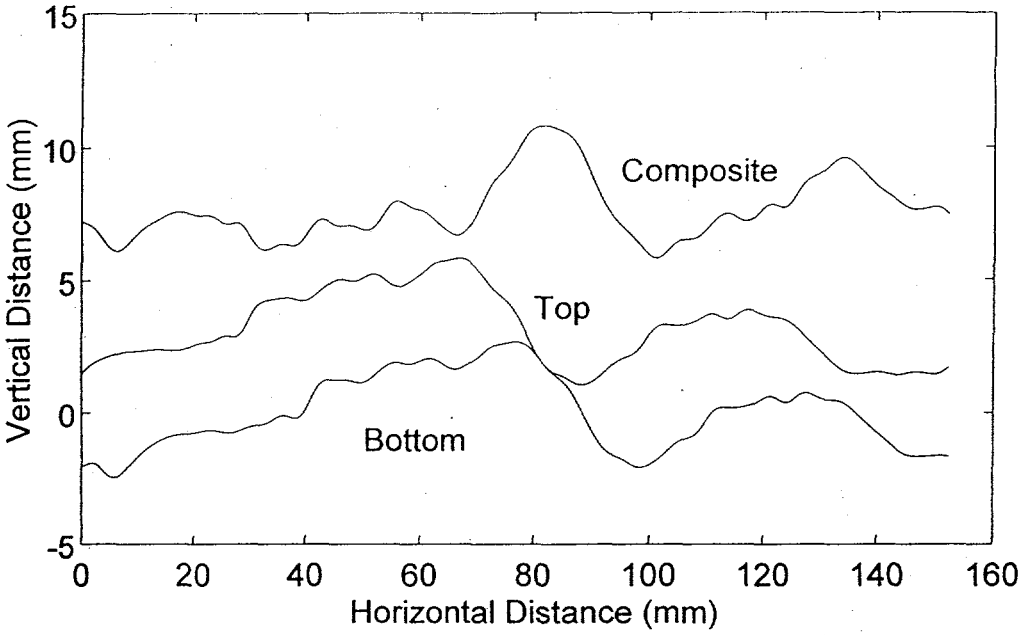

(a)

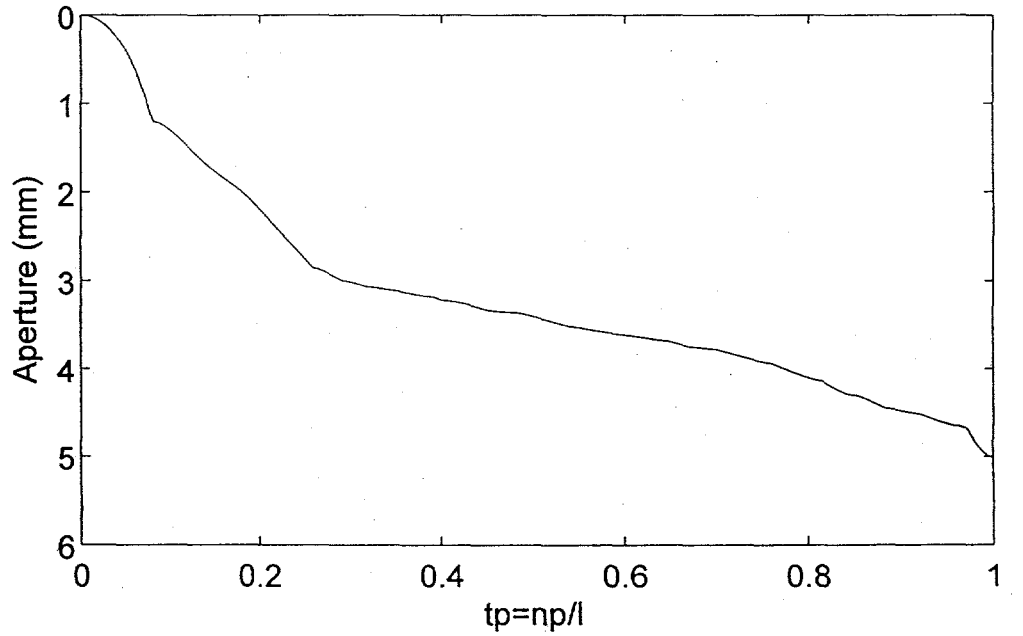

(b)

(a) Bottom, top, and composite topography, and (b) Bearing area curve fracture #1 after 10 mm of slip.

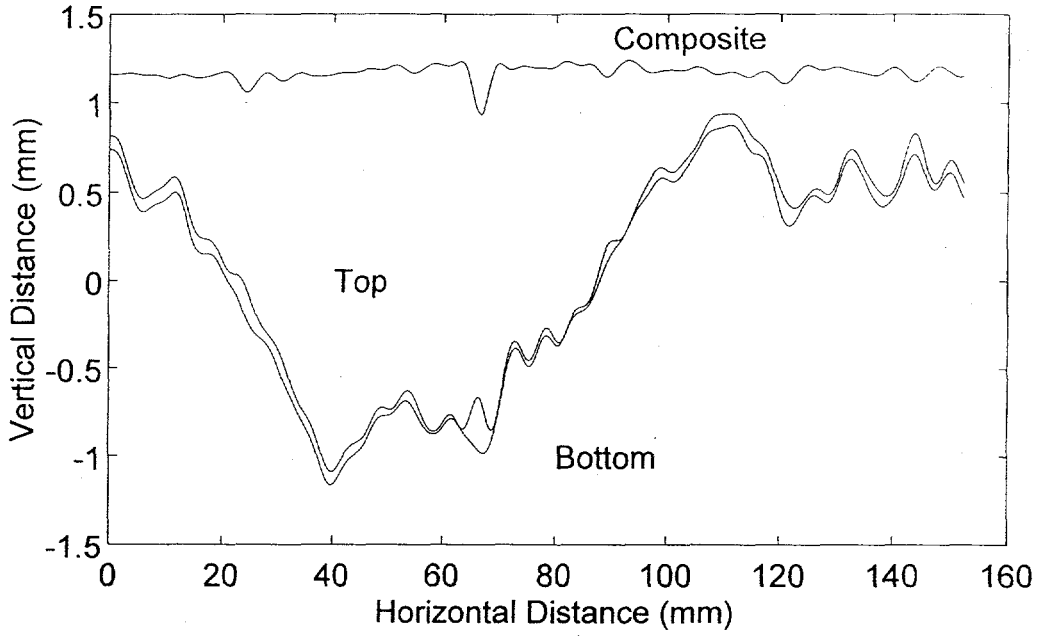

(a)

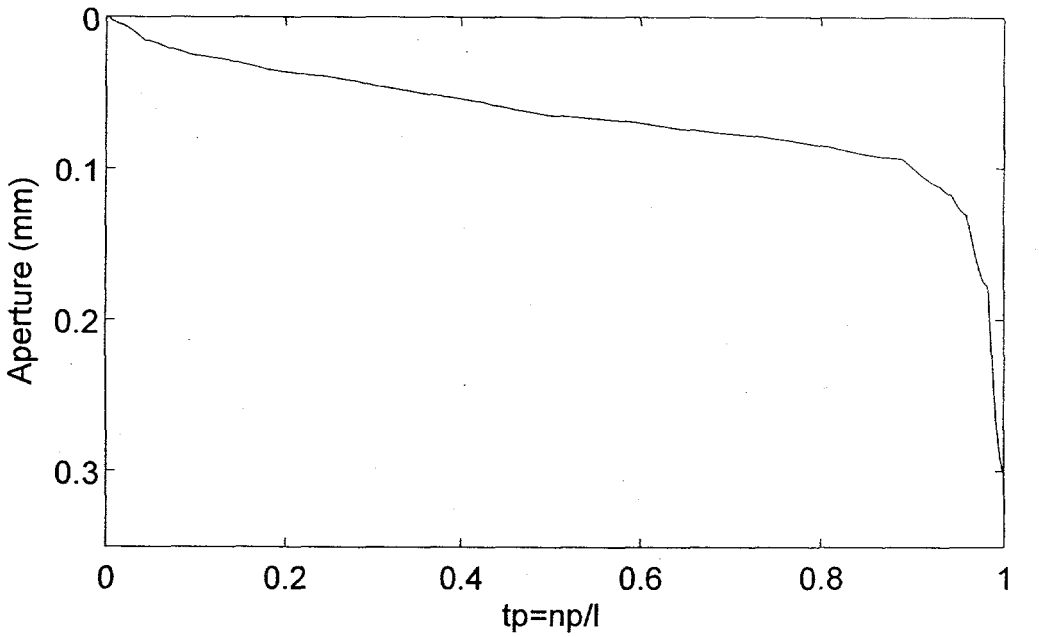

(b)

(a) Bottom, top, and composite topography, and (b) Bearing area curve for fracture #2 in a mated position.

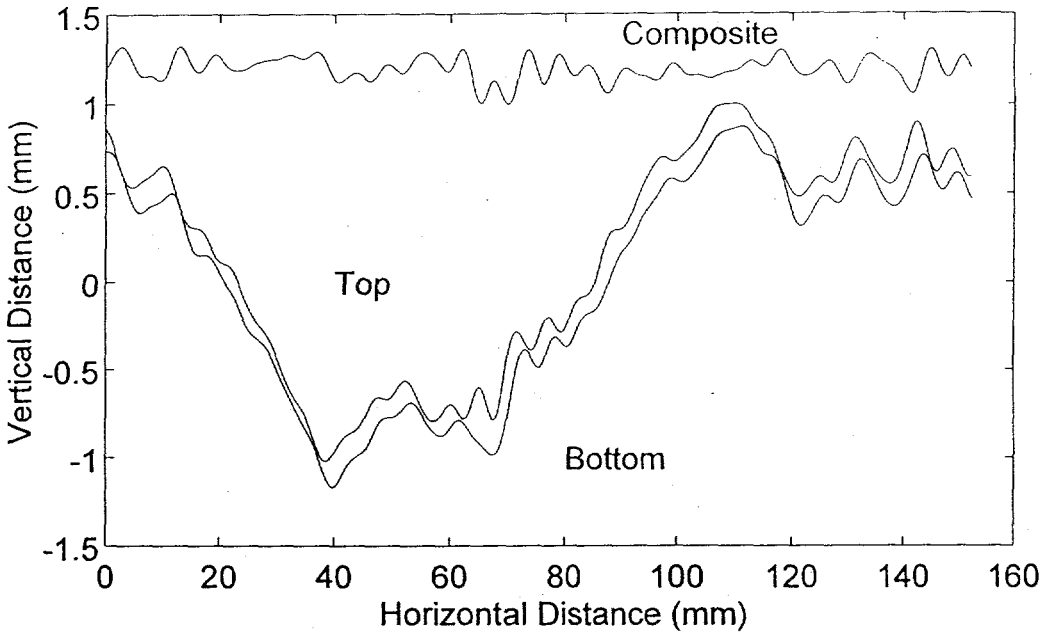

(a)

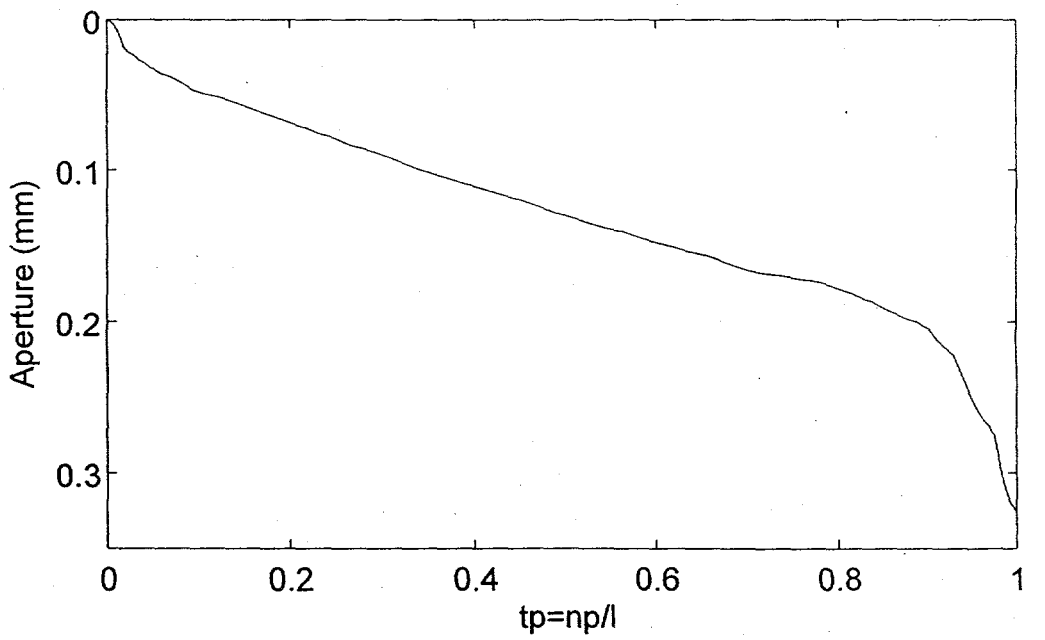

(b)

(a) Bottom, top, and composite topography, and (b) Bearing area curve for fracture #2 after 1 mm of slip.

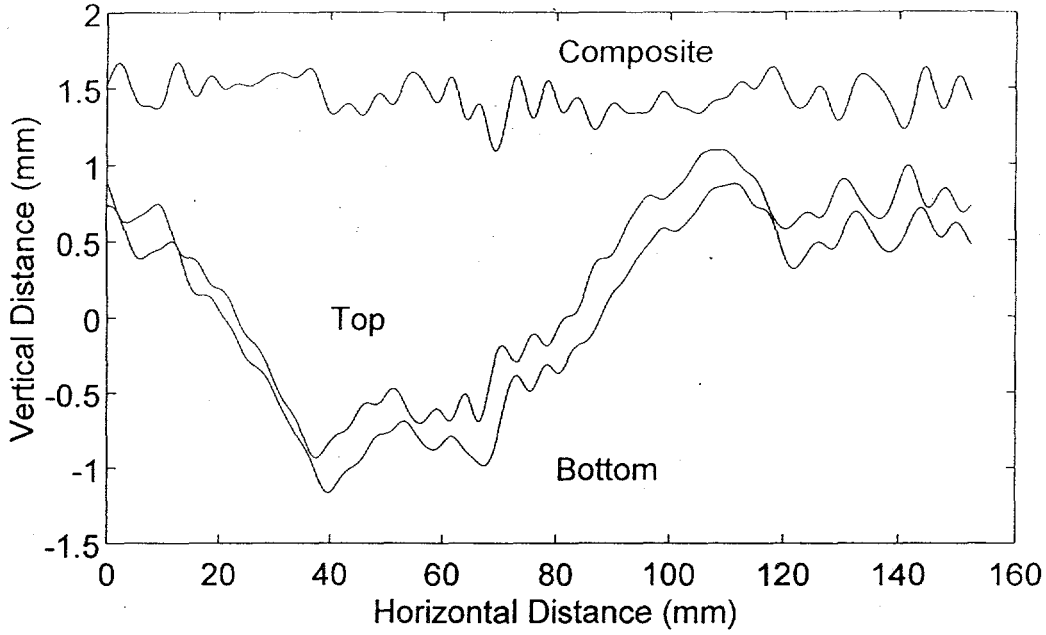

(a)

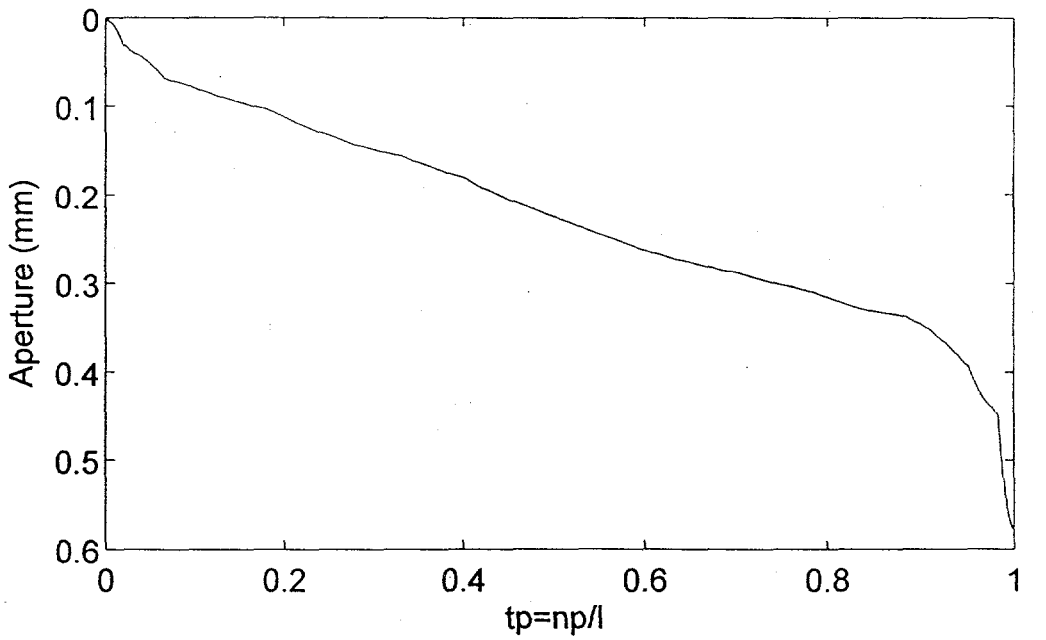

(b)

(a) Bottom, top, and composite topography, and (b) Bearing area curve for fracture #2 after 2 mm of slip.

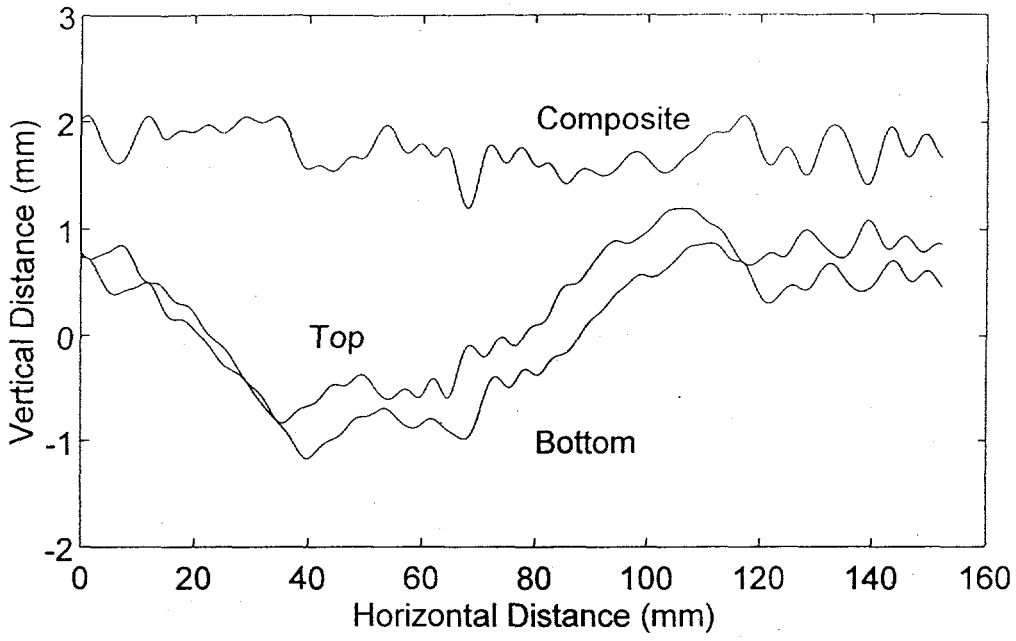

(a)

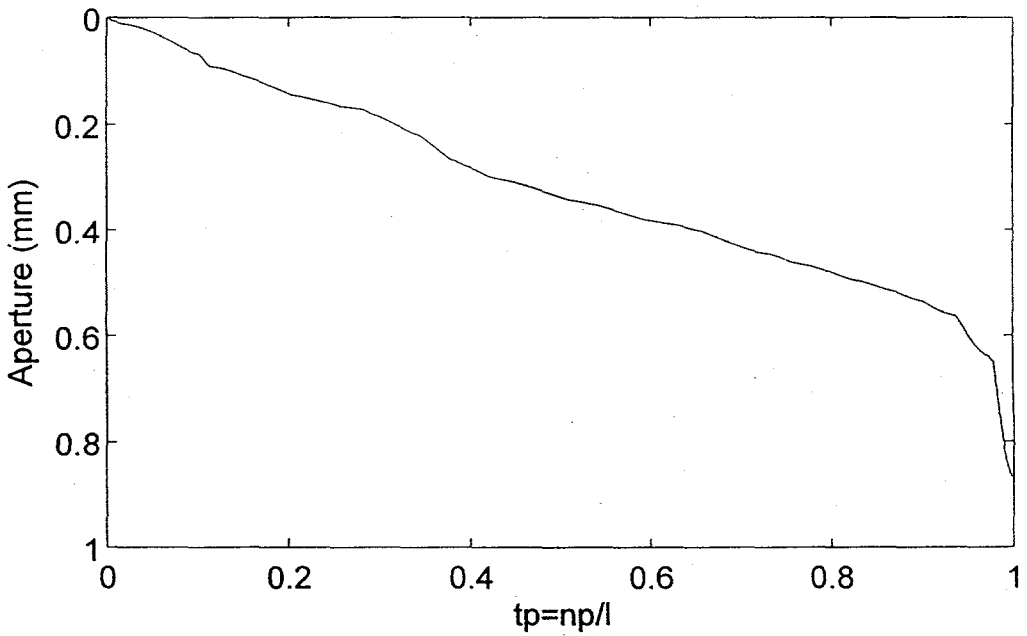

(b)

(a) Bottom, top, and composite topography, and (b) Bearing area curve for fracture #2 after 4 mm of slip.

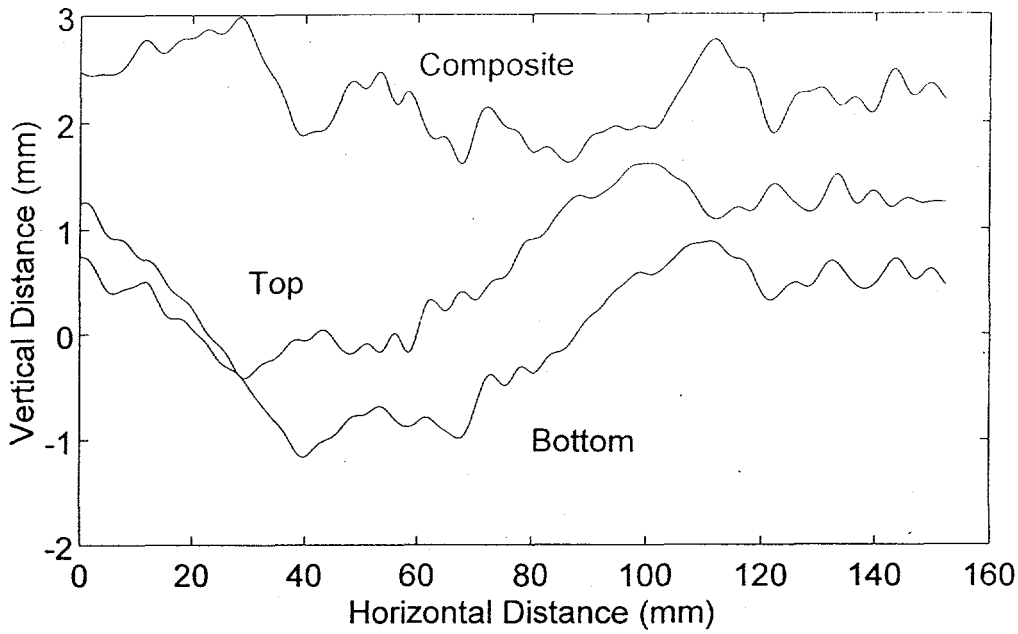

(a)

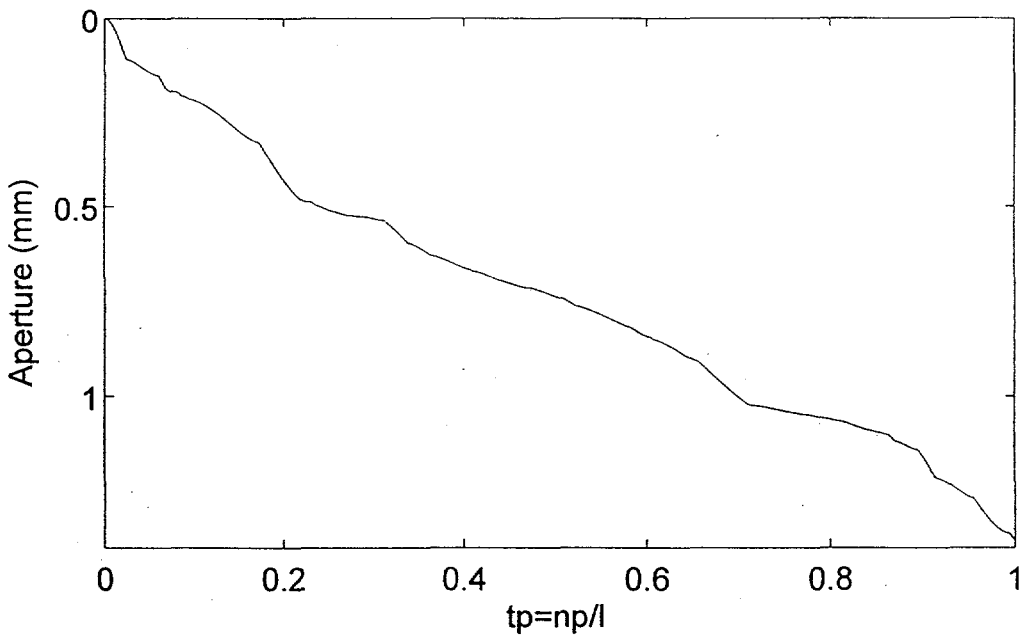

(b)

(a) Bottom, top, and composite topography, and (b) Bearing area curve for fracture #2 after 10 mm of slip.

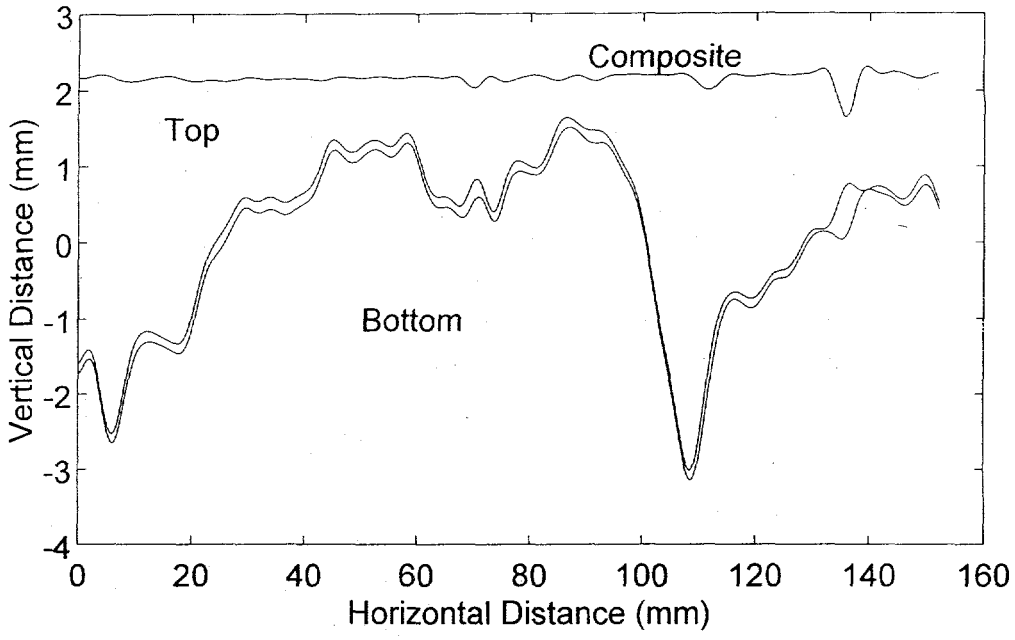

(a)

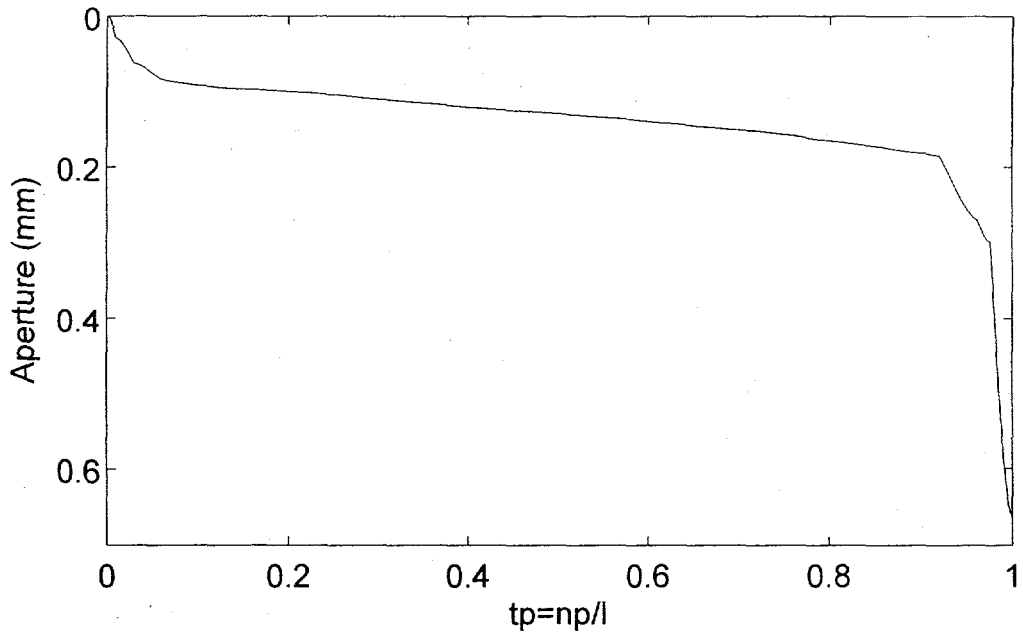

(b)

(a) Bottom, top, and composite topography, and (b) Bearing area curve for fracture #4 in a mated position.

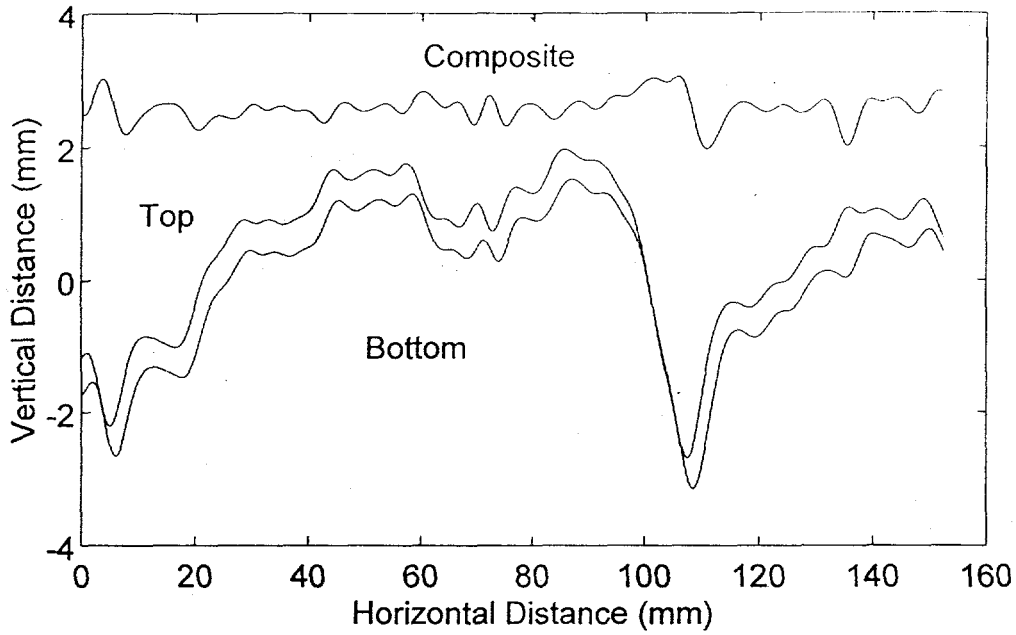

(a)

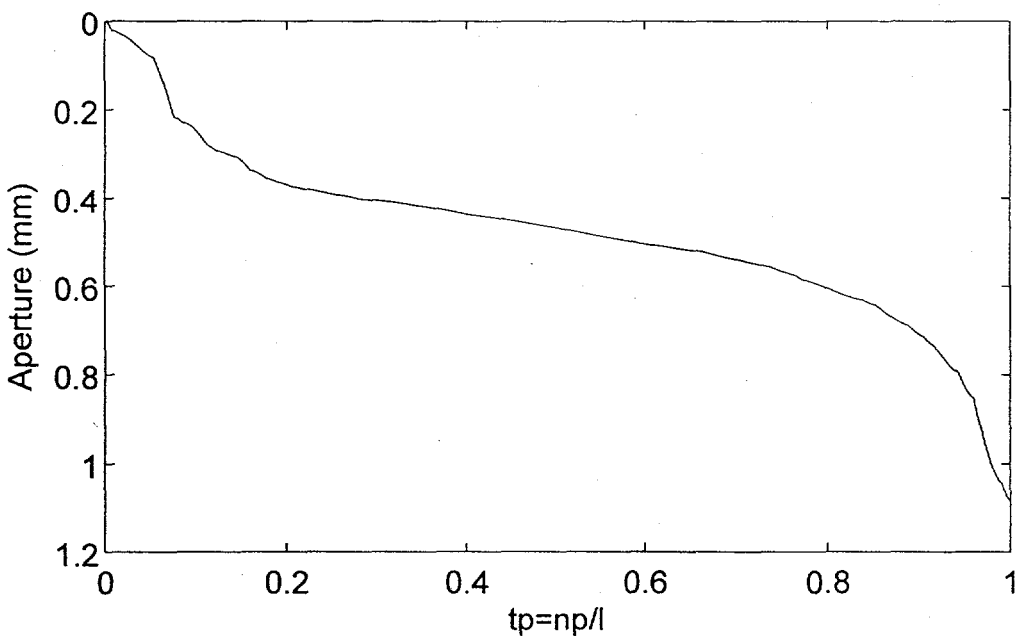

(b)

(a) Bottom, top, and composite topography, and (b) Bearing area curve for fracture #4 after 1 mm of slip.

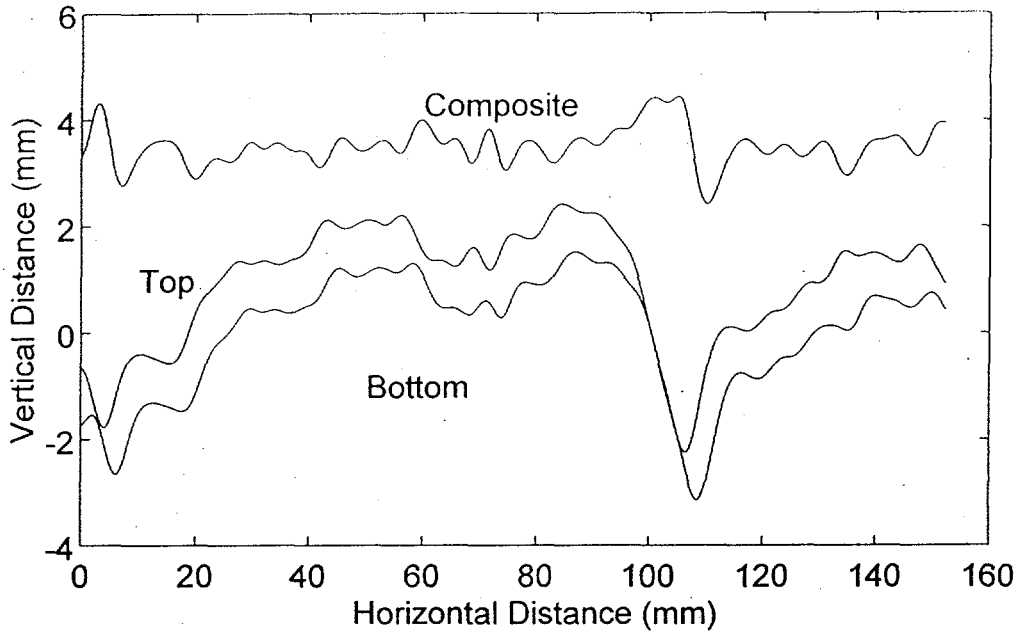

(a)

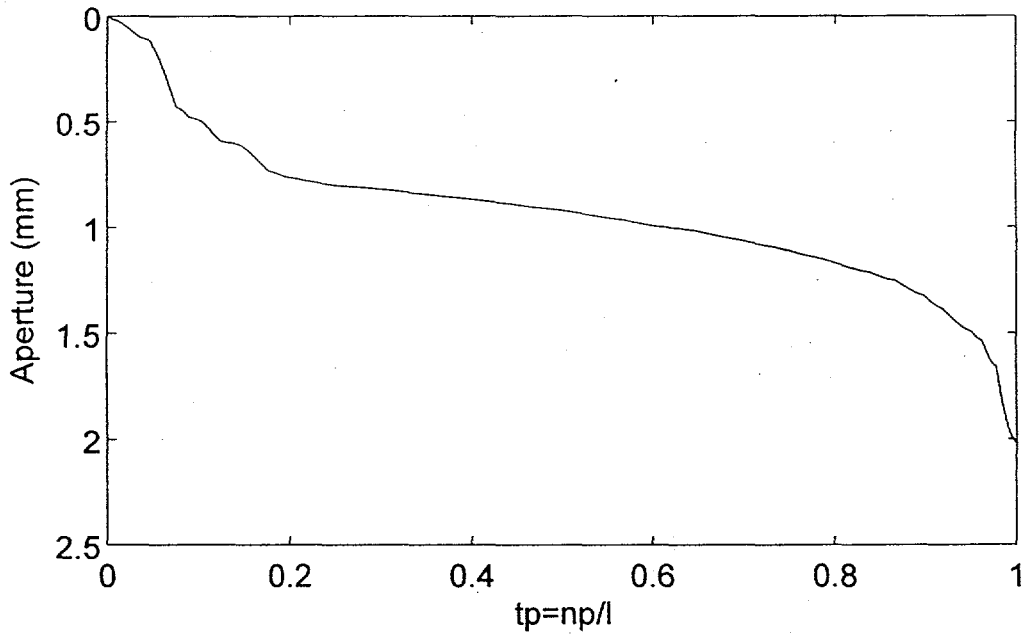

(b)

(a) Bottom, top, and composite topography, and (b) Bearing area curve for fracture #4 after 2 mm of slip.

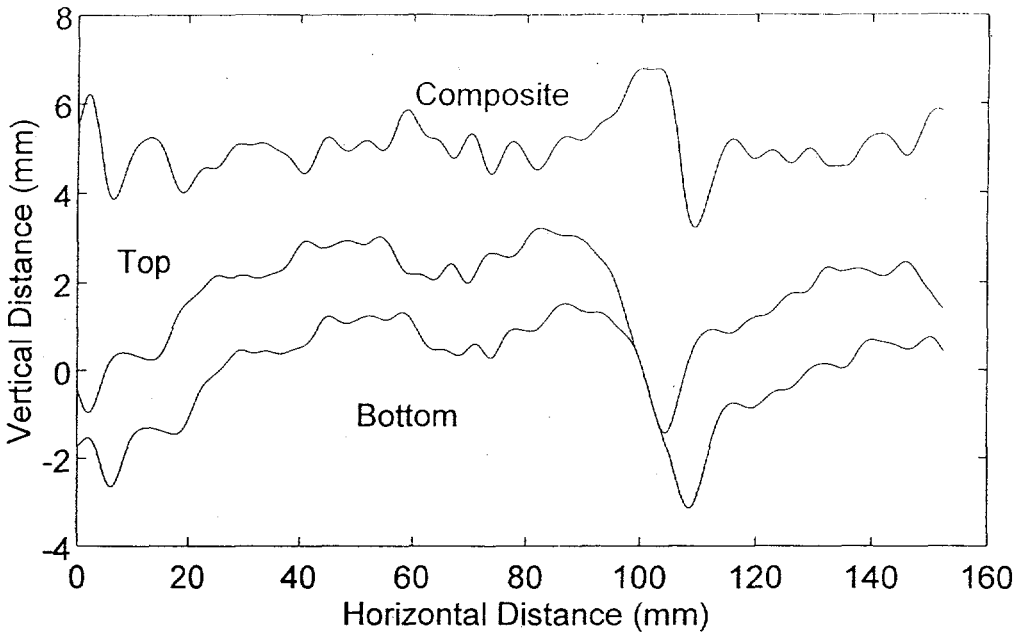

(a)

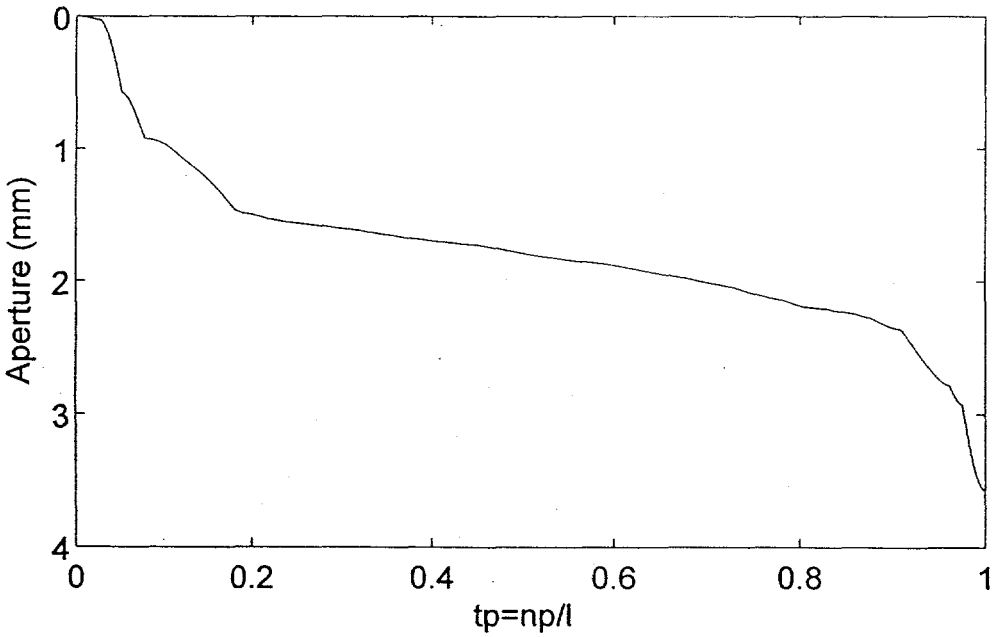

(b)

(a) Bottom, top, and composite topography, and (b) Bearing area curve for fracture #4 after 4 mm of slip.

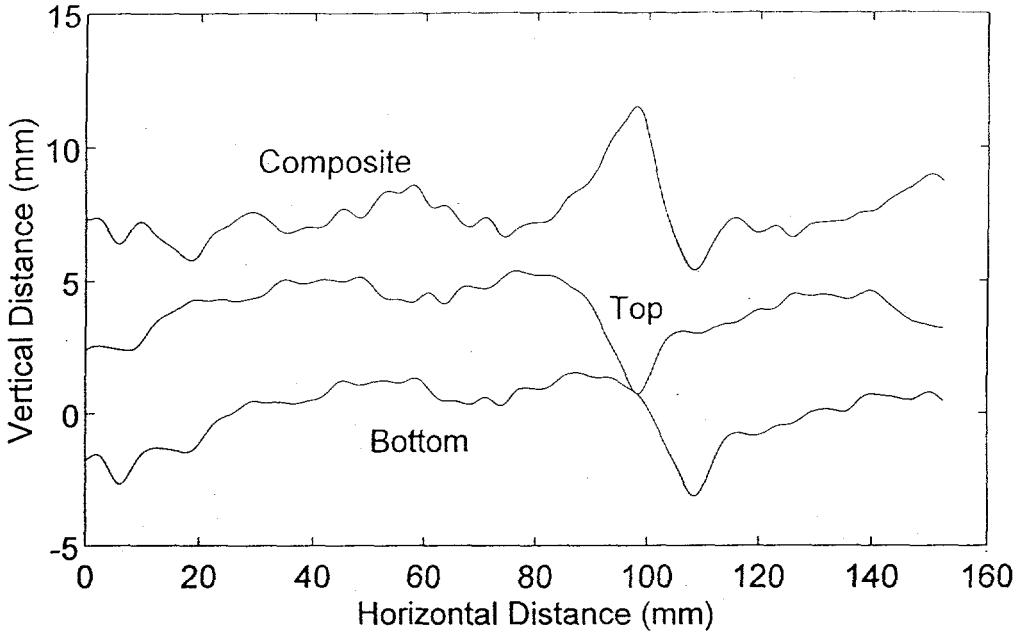

(a)

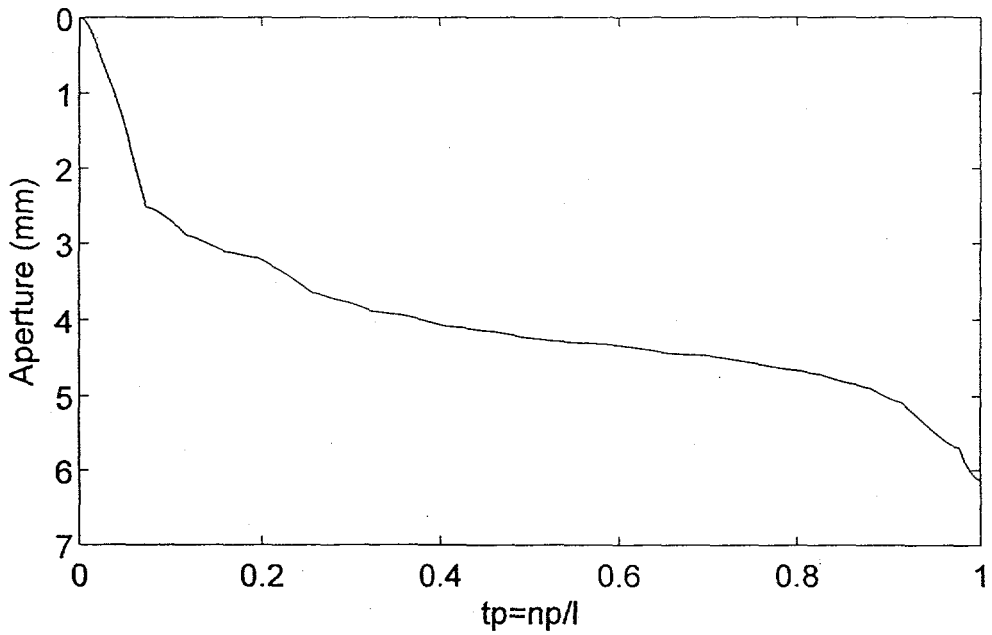

(b)

(a) Bottom, top, and composite topography, and (b) Bearing area curve for fracture #4 after 10 mm of slip.

YUCCA MOUNTAIN SITE CHARACTERIZATION PROJECT

UC814 - DISTRIBUTION LIST

1 D. A. Dreyfus (RW-1)
Director
OCRWM
US Department of Energy
1000 Independence Avenue SW
Washington, DC 20585

1 L. H. Barrett (RW-2)
Acting Deputy Director
OCRWM
US Department of Energy
1000 Independence Avenue SW
Washington, DC 20585

1 S. Rousso (RW-40)
Office of Storage and Transportation
OCRWM
US Department of Energy
1000 Independence Avenue SW
Washington, DC 20585

1 R. A. Milner (RW-30)
Office of Program Management
and Integration
OCRWM
US Department of Energy
1000 Independence Avenue SW
Washington, DC 20585

1 D. R. Elle, Director
Environmental Protection Division
DOE Nevada Field Office
US Department of Energy
P.O. Box 98518
Las Vegas, NV 89193-8518

1 T. Wood (RW-14)
Contract Management Division
OCRWM
US Department of Energy
1000 Independence Avenue SW
Washington, DC 20585

4 Victoria F. Reich, Librarian
Nuclear Waste Technical Review Board
1100 Wilson Blvd., Suite 910
Arlington, VA 22209

5 Wesley Barnes, Project Manager
Yucca Mountain Site Characterization
Office
US Department of Energy
P.O. Box 98608--MS 523
Las Vegas, NV 89193-8608

1 Director
Office of Public Affairs
DOE Nevada Operations Office
US Department of Energy
P.O. Box 98518
Las Vegas, NV 89193-8518

8 Technical Information Officer
DOE Nevada Operations Office
US Department of Energy
P.O. Box 98518
Las Vegas, NV 89193-8518

1 P. K. Fitzsimmons, Technical Advisor
Office of Assistant Manager for
Environmental Safety and Health
DOE Nevada Operations Office
US Department of Energy
P.O. Box 98518
Las Vegas, NV 89193-8518

1 J. A. Blink
Deputy Project Leader
Lawrence Livermore National Laboratory
101 Convention Center Drive
Suite 820, MS 527
Las Vegas, NV 89109

2 J. A. Canepa
Technical Project Officer - YMP
N-5, Mail Stop J521
Los Alamos National Laboratory
P.O. Box 1663
Los Alamos, NM 87545

1 Repository Licensing & Quality
Assurance
Project Directorate
Division of Waste Management
US NRC
Washington, DC 20555

1 Senior Project Manager for Yucca
Mountain
Repository Project Branch
Division of Waste Management
US NRC
Washington, DC 20555

1 NRC Document Control Desk
Division of Waste Management
US NRC
Washington, DC 20555

1 Chad Glenn
NRC Site Representative
301 E Stewart Avenue, Room 203
Las Vegas, NV 89101

1 E. P. Binnall
Field Systems Group Leader
Building 50B/4235
Lawrence Berkeley Laboratory
Berkeley, CA 94720

1 Center for Nuclear Waste
Regulatory Analyses
6220 Culebra Road
Drawer 28510
San Antonio, TX 78284

2 W. L. Clarke
Technical Project Officer - YMP
Attn: YMP/LRC
Lawrence Livermore National Laboratory
P.O. Box 5514
Livermore, CA 94551

1 V. R. Schneider
Asst. Chief Hydrologist – MS 414
Office of Program Coordination
and Technical Support
US Geological Survey
12201 Sunrise Valley Drive
Reston, VA 22092

1 J. S. Stuckless, Chief
Geologic Studies Program
MS 425
Yucca Mountain Project Branch
US Geological Survey
P.O. Box 25046
Denver, CO 80225

1 N. Z. Elkins
Deputy Technical Project Officer
Los Alamos National Laboratory
Mail Stop 527
101 Convention Center Drive, #820
Las Vegas, NV 89109

2 L. S. Costin, Acting
Technical Project Officer - YMP
Sandia National Laboratories
Organization 6313, MS 1325
P.O. Box 5800
Albuquerque, NM 87185

1 Ray Wallace
US Geological Survey
106 National Center
12201 Sunrise Valley Drive
Reston, VA 22092

1 L. R. Hayes
Technical Project Officer
Yucca Mountain Project Branch
MS 425
US Geological Survey
P.O. Box 25046
Denver, CO 80225

1 A. L. Flint
US Geological Survey
MS 721
P.O. Box 327
Mercury, NV 89023

1 R. E. Lewis
Yucca Mountain Project Branch
MS 425
US Geological Survey
P.O. Box 25046
Denver, CO 80225

1 D. Zesiger
US Geological Survey
101 Convention Center Drive
Suite 860, MS 509
Las Vegas, NV 89109

2 L. D. Foust
Nevada Site Manager
TRW Environmental Safety Systems
101 Convention Center Drive
Suite P-110, MS 423
Las Vegas, NV 89109

1 C. E. Ezra
YMP Support Office Manager
EG&G Energy Measurements Inc.
MS V-02
P.O. Box 1912
Las Vegas, NV 89125

1 E. L. Snow, Program Manager
Roy F. Weston, Inc.
955 L'Enfant Plaza SW
Washington, DC 20024

1 Technical Information Center
Roy F. Weston, Inc.
955 L'Enfant Plaza SW
Washington, DC 20024

1 Technical Project Officer - YMP
US Bureau of Reclamation
Code D-3790
P.O. Box 25007
Denver, CO 80225

1 B. T. Brady
Records Specialist
US Geological Survey
MS 421
P.O. Box 25046
Denver, CO 80225

1 M. D. Voegele
Technical Project Officer - YMP
M&O/SAIC
101 Convention Center Drive
Suite 407
Las Vegas, NV 89109

1 Paul Eslinger, Manager
PASS Program
Pacific Northwest Laboratories
P.O. Box 999
Richland, WA 99352

1 A. T. Tamura
Science and Technology Division
OSTI
US Department of Energy
P.O. Box 62
Oak Ridge, TN 37831

1 P. J. Weeden, Acting Director
Nuclear Radiation Assessment Div.
US EPA
Environmental Monitoring Sys. Lab
P.O. Box 93478
Las Vegas, NV 89193-3478

1 ONWI Library
Battelle Columbus Laboratory
Office of Nuclear Waste Isolation
505 King Avenue
Columbus, OH 43201

1 C. H. Johnson
Technical Program Manager
Agency for Nuclear Projects
State of Nevada
Evergreen Center, Suite 252
1802 N. Carson Street
Carson City, NV 89710

1 John Fordham, Deputy Director
Water Resources Center
Desert Research Institute
P.O. Box 60220
Reno, NV 89506

1 The Honorable Cyril Schank
Chairman
Churchill County Board of
Commissioners
190 W. First Street
Fallon, NV 89406

1 T. Hay, Executive Assistant
Office of the Governor
State of Nevada
Capitol Complex
Carson City, NV 89710

3 R. R. Loux
Executive Director
Agency for Nuclear Projects
State of Nevada
Evergreen Center, Suite 252
1802 N. Carson Street
Carson City, NV 89710

1 Brad R. Mettam
Inyo County Yucca Mountain
Repository Assessment Office
P. O. Drawer L
Independence, CA 93526

1 Lander County Board of Commissioners
315 South Humbolt Street
Battle Mountain, NV 89820

1 Vernon E. Poe
Office of Nuclear Projects
Mineral County
P.O. Box 1600
Hawthorne, NV 89415

1 Les W. Bradshaw
Program Manager
Nye County Nuclear Waste Repository
Project Office
P.O. Box 1767
Tonopah, NV 89049

1 Florindo Mariani
White Pine County Coordinator
P. O. Box 135
Ely, NV 89301

1 Judy Foremaster
City of Caliente Nuclear Waste
Project Office
P.O. Box 158
Caliente, NV 89008

1 Philip A. Niedzielski-Eichner
Nye County Nuclear Waste
Repository Project Office
P.O. Box 221274
Chantilly, VA 22022-1274

1 Dennis Bechtel, Coordinator
Clark County Nuclear Waste Div.
500 S. Grand Central Parkway
Suite 3012
Las Vegas, NV 89155-1751

1 Juanita D. Hoffman
Nuclear Waste Repository
Oversight Program
Esmeralda County
P.O. Box 490
Goldfield, NV 89013

1 Eureka County Board of Commissioners
Yucca Mountain Information Office
P.O. Box 714
Eureka, NV 89316

1 Economic Development Dept.
City of Las Vegas
400 E. Stewart Avenue
Las Vegas, NV 89101

1 Community Planning & Development
City of North Las Vegas
P.O. Box 4086
North Las Vegas, NV 89030

1 Community Development & Planning
City of Boulder City
P.O. Box 61350
Boulder City, NV 89006

1 Commission of European Communities
200 Rue de la Loi
B-1049 Brussels
BELGIUM

2 Librarian
YMP Research & Study Center
MS 407
P.O. Box 98521
Las Vegas, NV 89193-8521

1 Amy Anderson
Argonne National Laboratory
Building 362
9700 S. Cass Avenue
Argonne, IL 60439

1 Glenn Van Roekel
Director of Community Development
City of Caliente
P.O. Box 158
Caliente, NV 89008

1 G. S. Bodvarsson
Head, Nuclear Waste Department
Lawrence Berkeley Laboratory
1 Cyclotron Road, MS 50E
Berkeley, CA 94720

1 Michael L. Baughman
Intertech Services Corp.
P.O. Box 93537
Las Vegas, NV 89193

30 Dr. Bernard Amadei
University of Colorado
Department of Civil Engineering
Campus Box 428
Boulder, CO 80309-0428

	MS	
2	1330	C. B. Michaels, 6352 100/124211/SAND94-1941/QA
20	1330	WMT Library, 6352
10	1325	R. H. Price, 6313
5	0751	S. R. Brown, 6117
1	9018	Central Technical Files, 8523-2
5	0899	Technical Library, 13414
1	0619	Print Media, 12615
2	0100	Document Processing, 7613-2 for DOE/OSTI